Semiconductor nanolasers in living cells

Alasdair Fikouras

A thesis submitted for the degree of PhD
at the
University of St Andrews

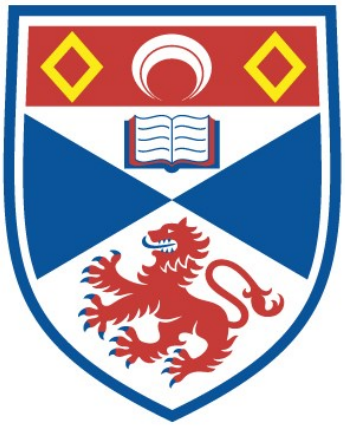

2020

Identifier to use to cite or link to this thesis:

DOI: https://doi.org/10.17630/sta/1220

SEMICONDUCTOR NANOLASERS IN LIVING CELLS

Alasdair Fikouras

This thesis is submitted in partial fulfilment for the degree of

Doctor of Philosophy (PhD)

University of
St Andrews

FOUNDED
1413

November 28, 2019

School of Physics and Astronomy
University of St Andrews, KY16 9SS

Abstract

In recent years there have been significant advancements in the miniaturisation of semiconductor laser devices, with optimised structures reaching extremely low thresholds, and operating at room temperature. This progress has enabled the demonstration of intracellular lasers, where miniaturised lasers are operated within living cells. Further developments in this new field focused on the optimisation of laser geometries as a potential method to increase the intensity and spectral resolution provided, over conventional biophotonic imaging approaches, using e.g. fluorophores and quantum dots. These intracellular lasers provide opportunities for sensing and multiplexing that were not possible with established techniques.

The focus of this PhD was on integrating these two research frontiers. It involved the fabrication, characterisation, and application of III-V, semiconductor nanodisk whispering gallery mode (WGM) lasers. These were processed to be biocompatible and applied as a biophotonic tool. The tiny resonator volumes - substantially smaller than the nucleus of a cell - could be easily integrated into a variety of cell types, including neurons and immune T-cells that had not been previously capable of internalising lasers. The minimal resonator volume allowed inserting multiple lasers within cells, as they moved through confined environments, such as micro-pore epithelial analogues. Furthermore, the unique properties of WGM lasers were exploited to investigate cell dynamics as an intracellular local refractive index sensor.

The realised lasers exhibited excellent properties, with high signal to noise ratios and very low laser thresholds (~0.13pJ). This was achieved by exploiting the large optical gain and high refractive index of GaInP/AlGaInP multi-quantum wells. In this work, the versatility of these lasers as a photonic platform was demonstrated by embedding them into transferable membranes. This was applied as a sensor for investigating epsilon near zero (ENZ) metamaterials and their optical enhancement properties, and additionally allowed the fabrication of different laser cavity designs such as a random network laser, to investigate the properties of random lasing.

Candidate's declarations:

I, Alasdair Fikouras, do hereby certify that this thesis, submitted for the degree of PhD, which is approximately 40,000 words in length, has been written by me, and that it is the record of work carried out by me, or principally by myself in collaboration with others as acknowledged, and that it has not been submitted in any previous application for any degree.

I was admitted as a research student at the University of St Andrews in September 2015.

I received funding from an organisation or institution and have acknowledged the funder(s) in the full text of my thesis.

Date Signature of candidate

04/05/2020

Supervisor's declaration:

I hereby certify that the candidate has fulfilled the conditions of the Resolution and Regulations appropriate for the degree of PhD in the University of St Andrews and that the candidate is qualified
to submit this thesis in application for that degree.

Date Signature of supervisor

04/05/2020

04/05/2020

Permission for Publication:

In submitting this thesis to the University of St Andrews we understand that we are giving permission for it to be made available for use in accordance with the regulations of the University Library for the time being in force, subject to any copyright vested in the work not being affected thereby.

We also understand, unless exempt by an award of an embargo as requested below, that the title and the abstract will be published, and that a copy of the work may be made and supplied to any bona fide library or research worker, that this thesis will be electronically accessible for personal or research use and that the library has the right to migrate this thesis into new electronic forms as required to ensure continued access to the thesis.

I, Alasdair Fikouras, confirm that my thesis does not contain any third-party material that requires copyright clearance.

The following is an agreed request by candidate and supervisor regarding the publication of this thesis:

PRINTED COPY

No embargo on print copy

ELECTRONIC COPY

No embargo on electronic copy

Date Signature of candidate

04/05/2020

Date Signature of supervisor

04/05/2020

04/05/2020

Underpinning Research Data or Digital Outputs

Candidate's declarations:

I, Alasdair Fikouras, understand that by declaring that I have original research data or digital outputs, I should make every effort in meeting the University's and research funders' requirements on the deposit and sharing of research data or research digital outputs.

Date 04/05/2020 Signature of candidate

Permission for publication of underpinning research data or digital outputs

We understand that for any original research data or digital outputs which are deposited, we are giving permission for them to be made available for use in accordance with the requirements of the University and research funders, for the time being in force.

We also understand that the title and the description will be published, and that the underpinning research data or digital outputs will be electronically accessible for use in accordance with the license specified at the point of deposit, unless exempt by award of an embargo as requested below.

The following is an agreed request by candidate and supervisor regarding the publication of underpinning research data or digital outputs:
No embargo on underpinning research data or digital outputs.

Date Signature of candidate

04/05/2020

Date Signature of supervisor

04/05/2020

04/05/2020

Acknowledgments

Firstly, I would like to extend my sincere gratitude to my co-supervisors, Professor Malte Gather and Professor Andrea Di Falco, for giving me this opportunity to have such an exciting and fascinating project. During this PhD, I have immensely valued their expertise, enthusiasm and guidance. They have helped me not only understand my work and produce this thesis but also look forward to working on it. I appreciate your advice, patience and encouragement you have given me during these past few years. I am extremely lucky to have such great supervisors.

I would like to particularly thank Dr Marcel Schubert for his assistance and proficiency that this work required. I really enjoyed troubleshooting the process and instruments, as well as the great conversations our work and all else besides. You were a source of inspiration and motivation in this project.

I would also like to thank Dr Andrew Meek for the endless conversations about our projects and his support throughout. They were really a highlight of the project and it was great to share a desk with you, thanks so much as a colleague and a friend.

I am very thankful for Dr Soraya Caixeiro, for her expertise in the project as well as her enthusiasm and innovation with the project as it developed. It was always great to have a person to turn to when I needed more hands or brain cells!

I would also like to thank Dr Alexandros Liles for his assistance in the early stages of the project, training me to use the instruments and assisting me in the initial fabrication efforts.

I want to thank my colleagues at the University of St Andrews too, which made the project a tremendous social, stimulating and collaborative experience. Especially in my two research groups the Synthetic Optics Group and Gatherlab. They made this PhD such a great experience! Thank you, James, Adam, Xin, Aline, Markus, Elena, Andrew, Andreas, Dinesh, Laura, Nils, Jonathan, Caro, Jan, Changmin, Joe, Yali, Sabina, Ana, Francisco and Philipp.

I would also like to thank all the technicians who kept the cleanroom working, as well as the staff. In particular, Callum Smith and Graham Beaton, who's constant diligence in maintaining the instruments made this PhD possible.

In the school of medicine, I'd like to particularly thank Simon Powis and Fiona Cooke for providing the biological cells used in this project. In the School of Physics and Astronomy I would like to particularly thank the school secretaries, Lesley Aitken, Linda Cousins and Dimali Vithanage, and the finance assistant Poppy Nicholson for ensuring that my postgraduate experience went smoothly. I would also like to thank Scott Johnson, for handling the many of the orders and deliveries, Ian Taylor for the conversations and guidance about the data and network management and Cameron Rae for giving me the opportunity to demonstrate in undergraduate labs, which were fantastic fun. Also, my thanks to David Miller, in the school of Chemistry, for his assistance using the FIB and in the BSRC I would like to thank Jill McVee for training me to use the confocal microscope.

I would also like to thank my friends everywhere for sharing in my passion for this project. Many thanks to my mother, Margaret McDougall, for always being there when I needed her. So many thanks to my extended family for their support, but most particularly my beloved wife Bethany Fikouras. Your support made everything that was difficult so much easier, for sharing in my joy and for marrying me.
Also, some thanks to my cat Skia for putting up with me, mostly.

Funding

This work was supported by the Engineering and Physical Sciences Research Council

EP/M508214/1

List of Publications and Conferences

Publications

- A.H. Fikouras, Marcel Schubert, Markus Karl, Jothi D. Kumar, Simon J. Powis, Andrea di Falco & Malte C. Gather., "Non-obstructive intracellular nanolasers," *Nat. Commun.*, vol. 9, no. 1, p. 4817, 2018.

- Jonathon Harwell, James Burch, Alasdair Fikouras, Malte C Gather, Andrea Di Falco, Ifor DW Samuel, "Patterning Multicolor Hybrid Perovskite Films *via* Top-Down Lithography", *ACS nano*, vol. 13, no. 4, p. 3823-3829, 2019.

Conferences

- SUPA Annual Gathering 2018 – Presentaiton: *Biolasers: Photonic Nanodisk Resonators for Intracellular Exploration.* A.H. Fikouras, Marcel Schubert, Markus Karl, Jothi D. Kumar, Simon J. Powis, Andrea di Falco & Malte C. Gather

- Nanophotonics and Micro/Nano Optics International Conference 2018 – Presentation: *Nanodisk lasers for internalisation by live cells* A.H. Fikouras, Marcel Schubert, Markus Karl, Jothi D. Kumar, Simon J. Powis, Andrea di Falco & Malte C. Gather

- OSA Biophotonics Congress: Optics in the Life Sciences 2019 – Presentation: *Intracellular Semiconductor Nanodisk Lasers* A.H. Fikouras, Marcel Schubert, Markus Karl, Jothi D. Kumar, Simon J. Powis, Andrea di Falco & Malte C. Gather

- International Conference on Biophotonics 2019 – Poster: *Semiconductor Intracellular Nanolasers* A.H. Fikouras, Marcel Schubert, Markus Karl, Jothi D. Kumar, Simon J. Powis, Andrea di Falco & Malte C. Gather

...Every hundred years a little bird comes and sharpens its beak on [the diamond mountain], and when the whole mountain is worn away by this, then the first second of eternity will be over.

Early top down diamond lithography process (*The Shepherd Boy*, Grimm's Household Tales (1812))

Table of Contents

1 INTRODUCTION 1

2 BACKGROUND AND THEORY 6

2.1 Laser Theory 7
2.1.1 Light-Matter Interaction 7
2.1.2 Properties of Laser Light 9
2.1.3 Components of a Laser 9
2.2 Semiconductor Gain Medium 10
2.2.1 III-V Semiconductor Materials 10
2.2.2 Bandgap Engineering 12
2.2.3 Superlattice 13
2.2.4 InGaP/AlInGaP MQW 14
2.2.5 Semiconductor Properties 16
2.3 Cavity and Resonator Physics 16
2.3.1 Laser Critical Dimension 17
2.3.2 Total Internal Reflection 17
2.3.3 Cavity Architecture 18
2.3.4 Basics of Whispering Gallery Mode Resonators 19
2.3.5 Properties of WGMs 20
2.3.6 Scalar Wave Solution of WGM 21
2.3.7 Quality Factor 24
2.3.8 Purcell Enhancement Factor 26
2.3.9 Tunability and Sensing 27
2.3.10 Other Sensing 28
2.4 Photon Pumping 29
2.5 State of the Art 31
2.6 Contributions 32

3 FABRICATION 33

3.1 Outline 34
3.2 Patterning 35
3.2.1 UV Photolithography 37
3.2.2 Electron Beam Lithography 38
3.3 Etching 41
3.3.1 Wet Etching 41
3.3.2 Dry Etching 46
3.4 Sacrificial Layer Release Etch 48
3.4.1 HF of Dry Etch Structures 52
3.4.2 Release from Substrate 53
3.5 Encapsulation 55
3.6 Contributions 56

4 CHARACTERISATION 57

4.1 Outline 58
4.2 Setups and Lasing 58

4.3 Fluorescence and Initial Lasing 60
4.4 Lasing Properties 61
4.4.1 Emission Behaviour 62
4.4.2 Spectra Linewidth and Disk Quality 67
4.4.3 Threshold measurements 68
4.4.4 Threshold Behaviour 71
4.5 Wavelength Sensitivity and Stability 72
4.5.1 Stability in Solution 73
4.5.2 Sources of Environmental Sensitivity 75
4.5.3 Refractive Index Sensing 76
4.5.4 Other Sensing 77
4.6 Contributions 78

5 BIOPHOTONICS PLATFORM 79

5.1 Outline 80
5.1.1 Biocompatibility 80
5.2 Setups and Procedures 81
5.3 Disk Identification 82
5.3.1 Confirming Internalisation 83
5.4 Investigated Cell Types 88
5.5 Cell Viability Investigation 90
5.5.1 Live/Dead Assay 91
5.5.2 Proliferation Rate Assay 92
5.5.3 Additional Viability Assays 93
5.6 Cell Lasing Experiments 93
5.6.1 Intracellular Lasing 94
5.6.2 Optical Barcoding 95
5.6.3 Intracellular Lasers in Confined Environments 97
5.6.4 Optical Sensing 99
5.6.5 Contributions 102

6 TRANSFERABLE PHOTONIC PLATFORM 103

6.1 Introduction 104
6.1.1 Nanolaser Membrane Fabrication 104
6.2 ENZ Platform 108
6.2.1 ENZ Substrates 109
6.2.2 WGM Experiments 110
6.3 Random Network Structure 114
6.4 Contributions 116

7 CONCLUSION 117

7.1 The Work 118
7.2 Outlook 118
7.2.1 Further Biophotonic Application 119
7.2.2 Random Network Lasers 119
7.2.3 Transferable Photonic Platform 119
7.3 Impact 120

BIBLIOGRAPHY 121

Introduction

Two and a half millennia of developed understanding separate the first recorded musings on the properties of light by Aristotle and Euclid and the discovery of its fundamental unit: the photon, by Einstein. The behaviour and properties of light can appear mysterious and counterintuitive to an untrained eye; it seems to be manipulatable, but simultaneously ethereal and fleeting in a way that matter is not. As our research into light continued, natural philosophers mistakenly assumed that it must have travelled in the luminiferous aether, as its behaviour was both familiar, but somehow totally alien. Many first investigations of light by children involve attempts to capture light by trapping it in a box, sometimes developing the initial idea with different sorts of boxes, with mirrors, or different shapes. This idea is not without merit, but the quality of the 'box' needs careful consideration…

The study of the properties of light and the foundation of modern optics was initially developed in the early 5th century BC and for many centuries focused extensively on developing astronomy. It was not until the 17th century that Newton demonstrated that light could be decomposed into spectra, which followed the proposition of light as a particle, followed shortly after by Huygens who replaced this with the more mainstream concept of the wave theory of light. This theory endured until the 20th century until Einstein established the photon: an electromagnetic wave-packet that has particle-like behaviour [1]. As a consequence of this improved understanding of light, this century has yielded new insights of the universe and has led to a rapid development and application in technologies that have transformed the world.

What is it about the nature of light that allows it to be such a versatile, applicable basis for technology? There are many aspects to this, but principally the relative ease of light generation, from primitive fire to the modern LED, and the apparently instantaneous nature of light travel (at least over the distances that make sense from the human perspective) allowed the development of global communication arrays and advanced imaging. However, the aforementioned range of light sources have a similar characteristic which has a significant disadvantage; it is diffuse. The light will decrease in intensity with a regular inverse square distance law, which was the nature of all understood light, from candles to stars. This is where one of the most significant advancements in the understanding of light-based systems comes into play, possibly one of the most ground-breaking for human technology thus far: the development of lasers [2]. A laser is a relatively simple system for its extensive impact on the world; in some sense it can be thought of as the realisation of the child's dream of trapping light in a box. Light, that is photons, are bosons, and can be forced to occupy the same state in a way that other particles, fermions, cannot. To ensure that light is made to occupy the same state, the mirrors of the 'box' need to be extremely reflective, the dimensions of the box are vitally important, and the air in the box needs to be substituted with a different, carefully selected medium, which interacts with the trapped light to keep it confined and compensate for any loss of light. Once this was mastered, the potential of lasers as a tool was realised, and has impacted our daily lives and created whole new actively growing branches of science and technology [3]–[6].

As with many active branches of technology, the focus has been on refinement and improvement. Within this century, lasers have been developed from a demonstration of

a first commercial system in the 1960s [7] to ultra-high energy density designed to ignite nuclear fusion [8], a process that was the almost exclusive domain of stars. On the other extreme, the same pressures and demands that miniaturised and refined electrical technology and shaped building sized computers into handheld devices are now driving low power consumption, miniaturisation of lasers. This miniaturisation is widely regarded as one of the most promising avenues to address the ever-increasing demand for speed and bandwidth in data transmission and information processing. At the leading edge of these photonic technologies, there are important challenges to overcome, a balance between the size of the device and the energy it requires to operate as a laser. Some of the most efficient lasers are targeted towards communications having an efficiency of single femtojoule / bit [6]. The smallest designs of solid-state lasers have utilised whispering gallery modes, which avoid the need for mirrors and instead use total internal reflection at the interface to reflect the trapped light [9], which will be the focus of this work.

Newton's optics were used to craft very high-quality microscopes for the time, and new optical devices were used to the further study of biology in an extremely fruitful manner. Today the application of lasers has revolutionised these workhorse microscopes, e.g. confocal and light sheet, and enabled new imaging modalities, such as multi-photon or super-resolution [10]. Until now, they have been used predominantly as external devices. The laser beam relayed into the sample with lenses or fibres and exciting fluorescent dyes or nanoparticle quantum dots. However, the advances on miniaturisation and efficiency of lasers made for telecoms applications, one can now consider direct integration into a biological system. Given the uncontested spectral resolution of laser emission compared to the traditional spontaneous light emitting sources, such as fluorescent proteins, could enhance multiplexing capability from around 10 - 20 possible wavelengths to several hundred. Additionally, these miniaturised laser sources could allow for the use of multiple lasers as single 'multiplet' useable as highly characterisable barcodes capable of uniquely labelling cells. Finally, lasers have often been utilised as sensors, and measuring tools for many applications and being able to have such a sensor within biological tissue, or cell could yield unprecedented insights for cell dynamics.

Such an 'intracellular laser' has been developed for some time now. Pioneering work utilising green fluorescent protein expressing cells as gain in an external mirrored cavity [11]. This was built upon using polymer microspheres and vesicles [12], [13]. These have already demonstrated the potential to expand on the possibilities of conventional

microscopy techniques significantly. However, the performance targets and trade-offs pertaining to miniaturisation of intracellular lasers are considerably different to the efficiency of the communications lasers discussed earlier. Lasers operating in an aqueous environment poses demands on their chemical stability and leads to reduced refractive index contrast between the laser material and its environment. Furthermore, the laser material, the resonator and the pump should have the least possible impact on cell physiology; to integrate intracellular lasers with other bioimaging technology platforms, they should operate in a spectral window already used for *in vivo* microscopy and where tissue scattering and absorption are low. At the extremes of miniaturisation, spasers that exploit surface plasmon interactions to generate lasers can be fabricated down to subwavelength dimensions (~22 nm) [14]. These have been demonstrated within cells, however require very high excitation energy densities that, whilst useful for photoacoustic imaging and photothermal destruction [15], are therefore undesirable for long term cell investigations due to the impact on viability. For low threshold dielectric semiconductors microcavity lasers, they are typically optimised for telecoms wavelengths and are utilised as lab-on-a-chip attached devices [16]. They often are composed of toxic materials, and a diminishing performance at the warm temperatures for cells, and lack the specificity for targets that traditional fluorophores have [17], [18]. Efforts to balance these requirements to produce a reliable laser device could be applied in conventional microscopy for image enhancement [19], or as an advanced cell label that could track biological targets with a level of specificity currently only possible with 2D light sheets [20], which currently find a limit in what can be analysed mostly by the enormous quantity of data that such a system produces.

Conventional lasers attempt to reduce the sources of loss caused by scattering. However, recently, random lasers have been identified as a low-cost laser cavity design utilising the scattering between particles. However, understanding their properties in a more controlled environment could aid in their development, and further their applications in display technology and material sensor [5]. This could be accomplished making a pre-determined network with light scattering at the nodes to create a similar effect to random scattering laser at particles [21], [22]. This thesis will explore the fabrication of this structure.

In this thesis, microdisk whispering gallery mode lasers are used as the platform to achieve intracellular lasing. Conventionally, microdisk lasers are produced on-chip, for use as a unit of a photonic circuit or lab-on-chip sensor [23], [24]. The nanolaser disks

for this work need to be free-standing or fully detached in solution for use in cells. Following the development of a process to produce optically pumped disk lasers with sub-μm diameters from a III-V multi-quantum well, a protocol is developed to detach these lasers and transfer them into cell cultures fully. The lasers are characterised in detail and the compatibility with cell – both in terms of stability and minimal impact on cell health – is explored. Barcoding of cells migrating through narrow pores is demonstrated, and a proof-of-principle of optical sensing is given.

Additionally, this thesis briefly explores embedding the nanolasers into a flexible, transferable membrane. The application of this membrane to control the position and conditions of the nanolasers combines the lab-on-a-chip and free-standing advantages. The size of this membrane could be controlled from micron-sized with a few disks to investigate small objects, or could be used as a macroscopic sensor, which could be used for a variety of conditions. This thesis will optimise the lift-off of such a nanolaser embedded membrane, and use it to investigate a novel set of 'metamaterials' with a permittivity ε near zero (ENZ), where the behaviour light is anomalous compared to materials regularly found in nature [25].

This thesis is structured as follows: the theoretical basis and background of the material and devices will be discussed in Chapter 2. This will then be followed by a discussion on the fabrication process in Chapter 3, and the characterisation of the laser performance in Chapter 4. The thesis will then detail the application of these devices as a biophotonic tool in Chapter 5, which will demonstrate the advantages of these structures by showing the cells passing through a confined environment, and its use as an advanced intracellular sensor. It will then discuss the progress so far in optimising a more general photonic platform in chapter 6, including ongoing work to investigate the enhancement response of ENZ and the current progress of the random network structure. Finally, ongoing research and impact will be discussed in Chapter 7.

Background and Theory

This chapter will begin with the basics of laser operation. The following section will discuss the gain medium and introduce III-V semiconductor materials used in this work, with some background on Multi-Quantum-Well (MQW) structures used for material gain in Section 2.2. Section 2.3 will then discuss the nature of the whispering gallery mode (WGM) laser cavity, the resonators used in this project. Section 2.4 will briefly discuss the pump sources and cavity threshold behaviour, and 2.5 discuss the context of the resonators described in the body of micro and nanolaser research.

2.1 Laser Theory

The development of new lasers for novel research and practical applications continues to further the state of the art with more powerful, miniaturised and efficient examples. This section serves to contextualise this research with an introduction to the fundamentals of the topic.

2.1.1 Light-Matter Interaction

Light and matter interact in many important ways, absorption, thermal radiation, scattering etc. all of which are fundamentally interactions between photons and electrons. The property of interest here: lasing is a somewhat distinct, quantum property of light that relies on a strong interaction between the photon field and an optically active material [26].

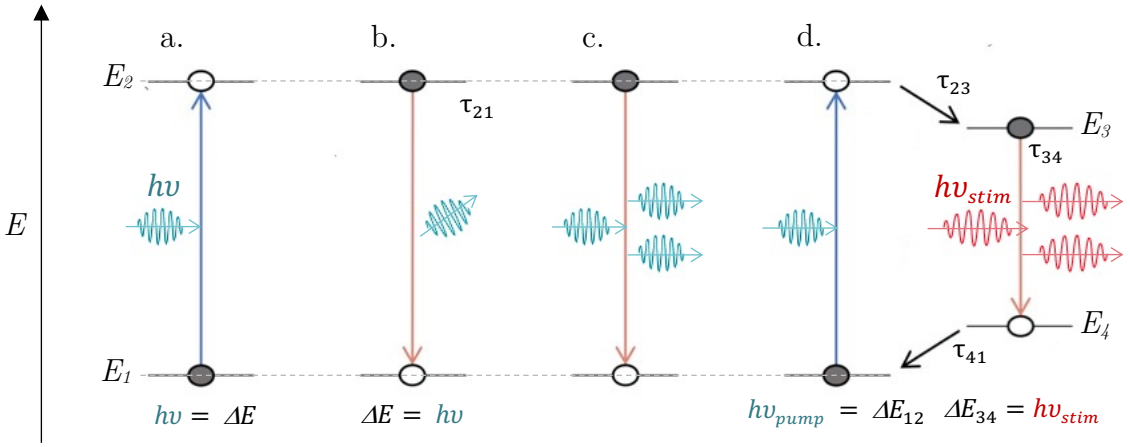

Figure 2.1: Schematic of light-matter interactions. a. Absorption of the incoming photon with energy hυ gives the electron enough energy to move from the E_1 ground state to the E_2 excited state. b. After some time τ_{12}, characteristic of the energy level, the electron can decay from the excited state to release a photon of energy ΔE, which has random phase and direction. c. Stimulated emission, a photon of energy $h\upsilon = \Delta E$ interacts with an electron in the excited state, triggering a decay. The emitted photon is a clone of the incident photon. d. An example of a 4-level laser system to optimise this process. A 'pump' photon of energy ΔE_{12} takes the electron to an energetic state, where it quickly undergoes a non-radiative decay to a slightly less excited state E_3. This state is very long-lived such that $\tau_{34} >> \tau_{23}$ such that electrons accumulate at this energy level. This increases the chance that an incident photon of energy ΔE_{34} can stimulate the emission. The final transition τ_{41} should also be very rapid to ensure that the population inversion is maximised.

To illustrate this interaction and how it relates to typical interactions of light and matter, we can start with absorption (Figure 2.1). This is a process by which incident

photons passing through a material are occasionally absorbed by the interactions with electrons, resulting in the electron being elevated to a higher energy state. The electron can remain in the excited state for a period of time dependant on the material and will relax back into its 'ground' state of lowest possible energy, by a variety of mechanisms. One of these mechanisms, a process where electrons can make a transition from excited to the ground state, is called spontaneous emission. The transition energy of the electron is emitted as a photon with random phase and direction, resulting in the phenomena of thermal emission and fluorescence. This is described as a 'linear process', as the amount of light emitted by these materials is directly proportional to the light absorbed.

If the electron is already in such an excited state, a further photon of similar energy to the gap between the ground and excited state, passing through the material has a quantum mechanical interaction with the excited electron, stimulating it to drop to its lower energy state. This stimulated transition of the electron creates a duplicate of the incident photon, in terms of energy, phase, directionality and polarisation. For stimulated emission to enable lasing, there should be a high probability of a photon encountering an electron in the excited state, which is not a typical state of matter and is referred to as a population inversion. A common approach to creating such an inversion is to find a material, or combination of materials, where a 4-level system can form. Electrons can be given energy by a pump source that takes them to an excited state, where they then quickly decay to a less energetic state but not the ground state. The next transition typically has a long lifetime compared to the other transitions, such that electrons accumulate at this energy level, creating the population inversion. Radiative energy released by the transition to the next lowest energy level can go on to stimulate further transitions. The final transition must be similarly rapid to drain electrons to the ground state as if electrons accumulate in the E_3 state, this removes the population inversion, and incoming photons of E_{23} would be absorbed, resulting in no laser.

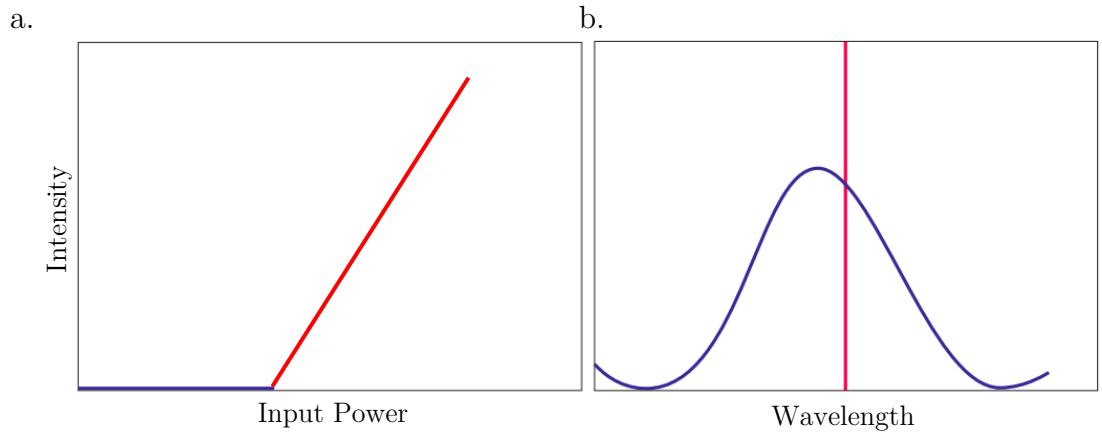

Figure 2.2 The essential characteristics of a laser. a. A graph showing the input energy versus the output energy of a laser device. The change in slope indicates the threshold that defines the transition from spontaneous processes (blue) to stimulated lasing (red). b. The same process but showing transition in spectral shape: the broadband spontaneous emission spectrum (blue), narrowing above threshold to the intense monochromatic laser light (red). Adapted from [26].

2.1.2 Properties of Laser Light

Lasers and laser light emitters have several unique characteristics (Figure 2.2). As discussed, lasing requires a population inversion and thus only occurs if the material is pumped with high energy photons sufficiently strongly. This is called the 'threshold', where the characteristic absorption and spontaneous emission mechanisms are no longer the dominating optical effect, and the stimulated emission leads to a dramatic increase the output light from the system. Additionally, the emission pattern transitions from the relatively broad band of wavelengths centred on the material transition to a very narrow band, sharp spectroscopic peak from a laser. Because the photons in the medium are duplicated, in the laser, the light coming out is amplified. Hence the term 'gain' is often used be used to describe the ability of a medium to achieve amplification.

2.1.3 Components of a Laser

These discussed properties can be used to identify the components to form a laser. To supply enough photons to sustain the population inversion, this requires a high intensity of incoming high energy photons. Specific material properties are required for a population inversion with which stimulated emission photons can interact to achieve amplification. Finally, the majority of the emitted photons must be trapped in the medium to stimulate the transition of more electrons further, though a variety of possibilities exist and will be discussed later.

This makes up the three major components of a laser: the gain material; where the electron transition from population inversion creates the photons and the chain reaction of stimulated emission, the pump; a light source which provides the energetic photons to sustain the population inversion, and finally the cavity; which ensures sufficient photons are trapped for the sustained process of stimulated emission, which has specific length requirements that will be discussed in Section 2.3.

2.2 Semiconductor Gain Medium

This subsection will introduce the materials utilised in this work for the gain medium of a laser. It will discuss how they can be optimised for emission wavelength, confinement and threshold. It will then describe the specific structure utilised, as well as a brief consideration of specific properties relevant to future discussion.

2.2.1 III-V Semiconductor Materials

This work builds previous research investigating organic emitters (dyes) as gain materials [12], [13], [27]. These emitters have a diverse spectrum of exploitable wavelengths and have been extensively developed for a range of uses. These materials have been demonstrated as gain for a variety of conformations, even within live cells. As will be discussed in Section 2.3, there is a minimum length requirement for a laser, but it is important to note that this is the length that light experiences, the optical path length, which is a function of both wavelength and refractive index. To increase this from the refractive index of polymers and silica, which are the scaffolds in which the dye is doped, we can explore inorganic semiconductors.
The origin of refractive index n is a combination of the properties of a material, can be described in first approximation by the following equation,

$$n(\omega) = 1 + \frac{q_e^2}{2\epsilon_0 m}\left(\frac{N}{(\omega_0^2 - \omega^2)}\right)$$

This gives a relationship between the refractive index $n(\omega)$ and the number of atoms per unit volume (N), the resonant frequency of the electron in the material (ω_0) and the frequency of the incident light (ω) [28]. The number of atoms per unit volume gives an indication of the electron density, and in the case of gallium arsenide is an order of

magnitude greater than in polystyrene, a commonly used polymer scaffold for organic lasers.

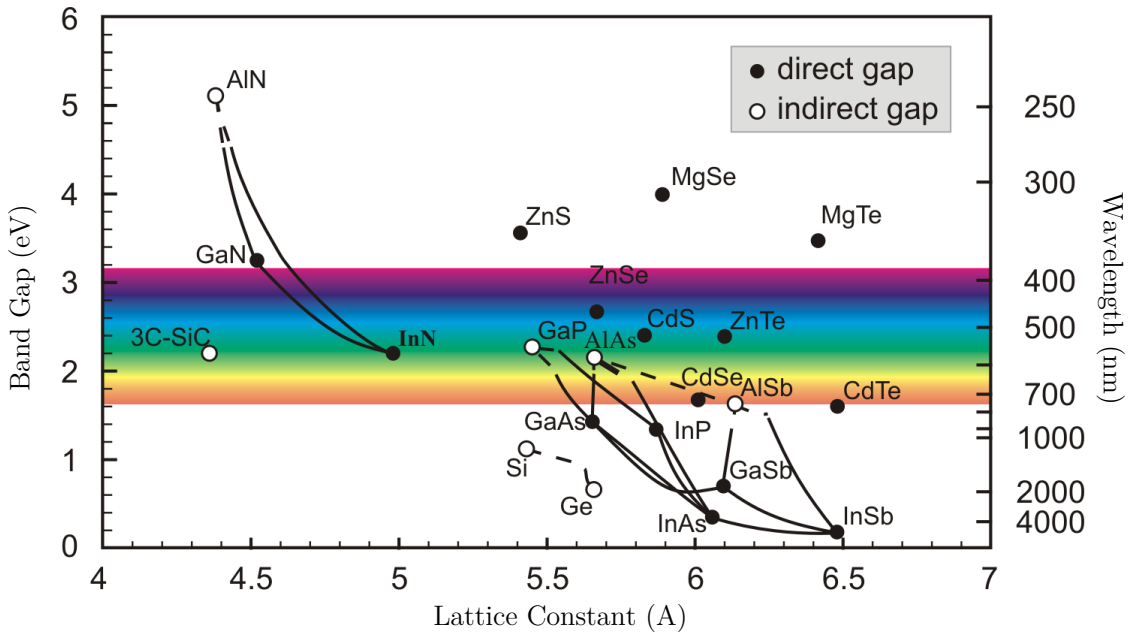

Figure 2.3 A diagram of the bandgap energies of semiconductor crystals of different compositions. The bandgap energy defines the wavelength of the stimulated photons. A direct bandgap describes the simple transitions discussed earlier, whilst the indirect bandgap requires additional momentum to allow the electron to transition laterally. Reproduced from [29].

Some of the most desirable active materials are categorised as III-V semiconductors. They are grown in layers of controlled thickness from elements of Group 3 and Group 5 of the periodic table, evaporated and deposited on a substrate of desired crystal structure, a process called molecular beam epitaxy (MBE). These materials are highly sought after not just for the large gain they can produce within their structures, but also for the bandgaps, which act as the previously discussed energy levels in semiconductor crystals, as alloys can produce a spectrum of wavelengths as seen in Figure 2.3.

2.2.2 Bandgap Engineering

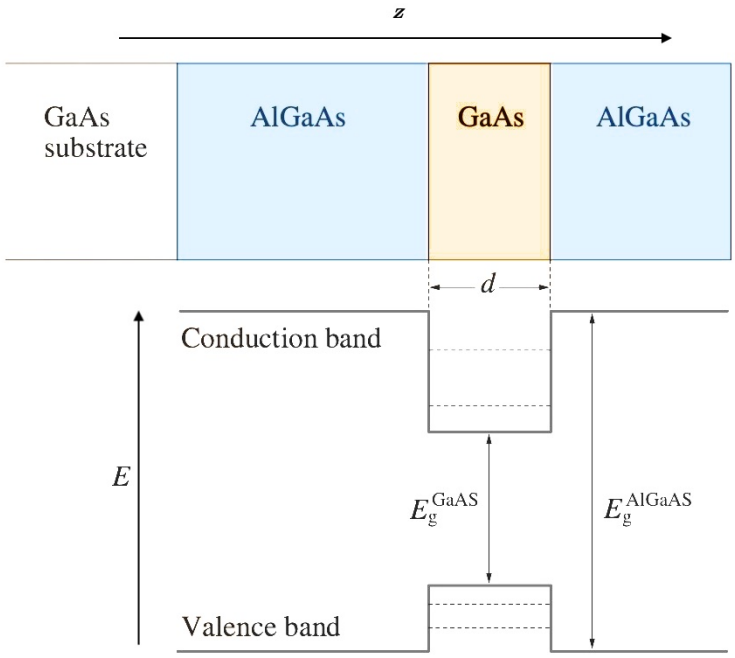

Figure 2.4. Basics of a bandgap structure. A wafer material is epitaxially grown from a substrate in layers (increasing z), which results in a set of discrete energy levels. Much like the 4-level system described in Figure 2.1 d, Eg_{GaAs} is the long-lived transition where charge carriers accumulate in a 'potential well'. The electron transitions, rather individual atomic transitions, are defined by this bandgap which depends on the material composition. A population inversion is achieved readily due to the fast-moving conduction band negative charge carriers (electrons) compared to the relatively slow-moving valence band positive charge carriers (holes). Adapted from [30].

The precise band structure can be engineered by adjusting the composition of the different layers and thickness, creating what is referred to as a quantum well. These are deposited as described in Figure 2.4, which depicts a simplified GaAs bandgap for infrared emission.

It is easy to correlate the energies of the band structure to the energy levels Figure 2.1 The population inversion in such materials is relatively easy to achieve, with the separation of holes and electrons being enforced by the comparatively slower rate of motion of the holes through the valence band [31]. The electrons accumulate in a 'Quantum Well' (QW) where they are confined at discretised energy levels, which provides the population inversion. Following this, recombination at the E_g by stimulated emission can result in strong thermal effects, which can often necessitate cooling for sustained operation, and practically useful thresholds [4], [9].

For this work, it was desireable to emit in the visible part of the spectrum for compatibility with commonly used imaging instruments. For instance, biological setups that are optimised to image visible light emitting fluorophores. As can be seen from the available bulk materials in Figure 2.3, there are a few available options for visible emission.

2.2.3 Superlattice

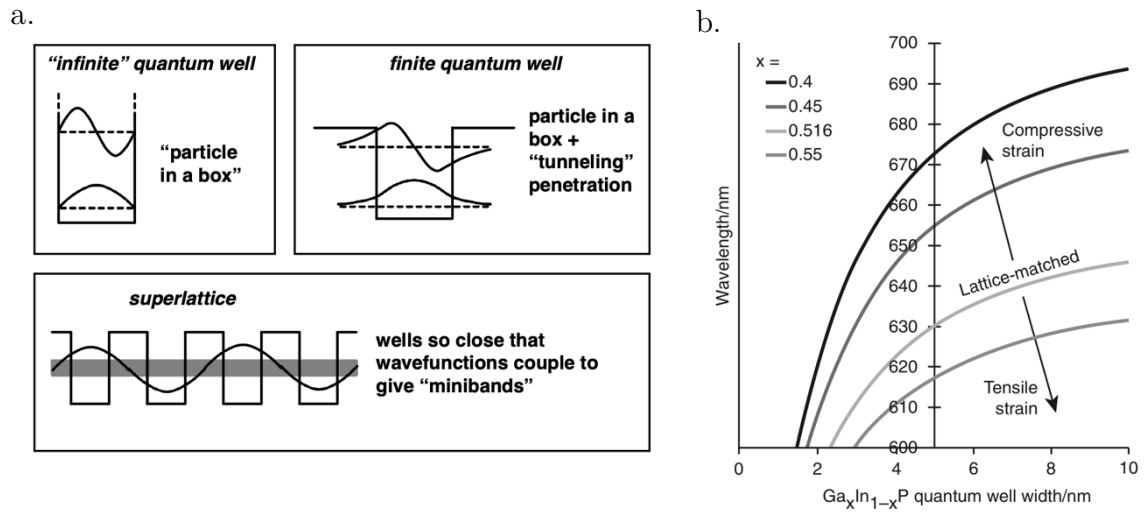

Figure 2.5 a. The electrons are typically not trapped in a perfect quantum well and can decay through the edges of the material by quantum tunnelling. By structuring a series of closely separated potential wells (referred to as a 'multi quantum well' (MQW)), the electrons can tunnel through the separation into the next well. The wavefunctions of these particles combine to convert the discrete energy levels into minibands where the charge carriers can be more dispersed. Reproduced from [32] *b. The 'strain' effect on wavelength output by changing the atomic composition ratio of the III-V material, and how these effects vary with the quantum well width. When the native lattice constant is smaller than the substrate on which the material is deposited, this results in compressive strain, as opposed to tensile strain where the native lattice structure is stretched to mimic the substrate. Reproduced from* [3].

Additional semiconductor properties of these alloys and single quantum wells can be exploited to reduce the thermal effects of recombination introduced in the previous section, and further tune the emission of the final structure. One such method alternates the composition of deposited semiconductor materials in stacked layers, referred to as a superlattice. This utilises the finite confinement of quantum wells: neighbouring quantum wells (MQW) separated by sufficiently close distances result in the formation of 'minibands' as a consequence of this is that electrons are able to 'tunnel' through the sides of the well. These minibands form the discretised energy levels and therefore, the bandgaps and are dependent on the MQW materials, thickness and number (Figure 2.5 a) [30]. For further tuning, another method arises as a consequence of evaporating

materials of different composition, as often one must to force a crystal adopt the lattice constant (Figure 2.3) of the substrate during the epitaxial growth [33]. This is referred to as 'strain engineering' and can tune the bandgap further (Figure 2.5 b). The benefits of this engineering can be explained thus: electrons are fermions and are forbidden to occupy the same state by the Pauli exclusion principle, and hence can fill the available occupancy of a bandgap such as that in Figure 2.4 relatively quickly. However, in a conduction miniband like those in an MQW, there can be much a greater distribution of the charge carriers, allowing for a greater population inversion, as well as minimising non-radiative recombination losses due to other types of light/matter interaction. This more efficient structure is much less temperature-sensitive than its bulk counterpart resulting in more efficient thresholds [34], as well as potentially minimising carrier interactions that might result in broader than expected peaks by reducing the linewidth enhancement factor [35], [36].

2.2.4 InGaP/AlInGaP MQW

In this work, to achieve the visible light emission, a stack of 2 quantum wells made from $In_{0.59}Ga_{0.41}P$ is utilised [37]. The effect of quantum well width now becomes an important factor (Figure 2.5 b). Ideally, the emission of the disks should be as far-red as possible, to minimise scattering and to potentially allow for a longer wavelength pump source. To maximise the gain and shift the spectra to a shorter wavelength, a MQW structure is ideal [38].

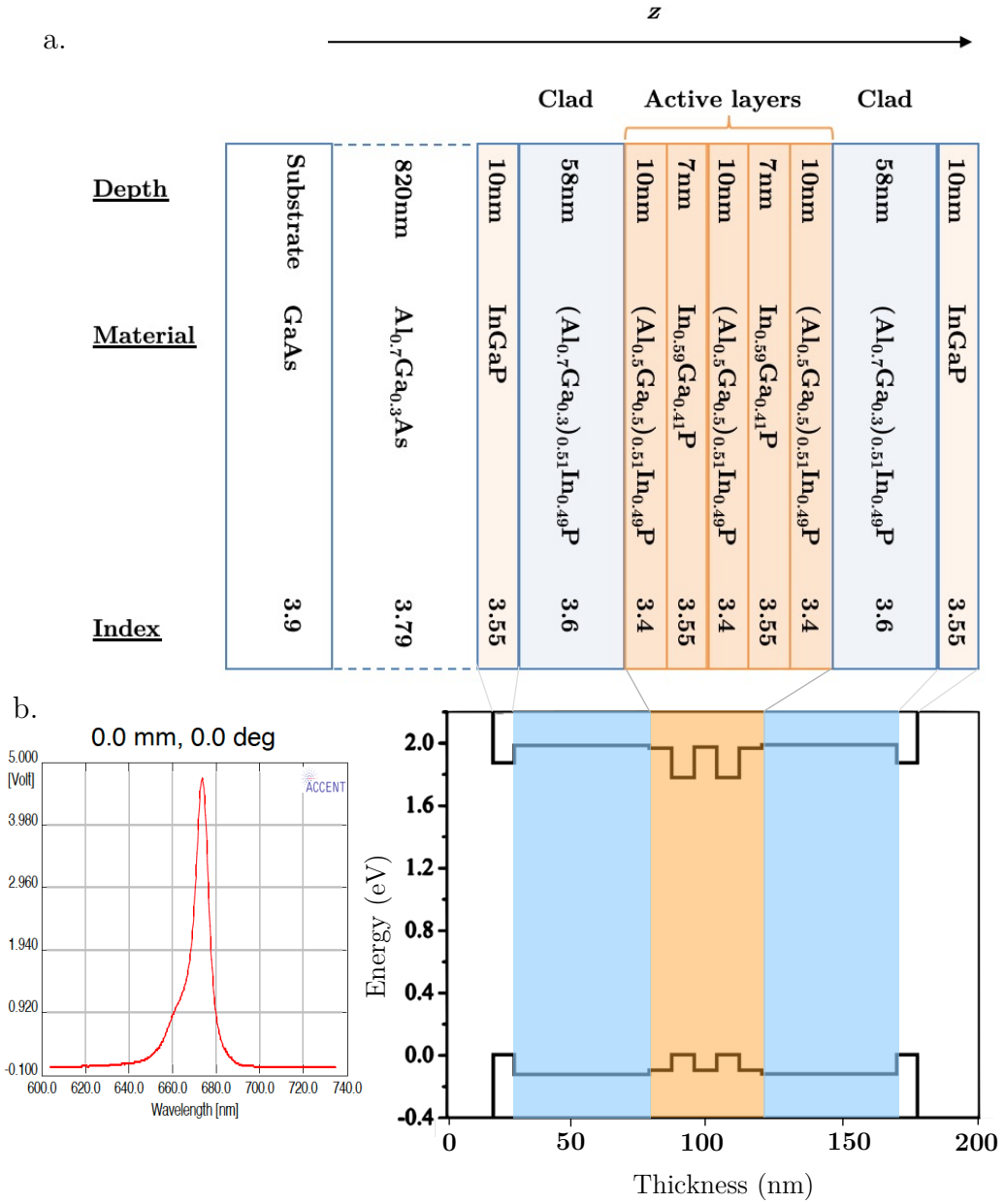

Figure 2.6. The MQW structure used in this work. The InGaP quantum wells and AlInGaP waveguides form the active region (orange) and are clad in AlInGaP (blue) grown on an epitaxial release layer of AlGaAs and a GaAs substrate. The bandgap structure from each layer is adapted from a similar structure VSCEL laser [39]. b. Fluorescence emission of the wafer structure, produced by the EPSRC National Center for III-V Technologies, Sheffield).

Figure 2.6 is a schematic and bandgap structure of the wafer used for this work. The 7nm InGaP quantum wells are predicted to be compressively strained and emit around ~1.83 eV or ~680nm, which is confirmed by fluorescence spectrum provided, with a peak at 675nm (Figure 2.6 b), the refractive indexes are estimated from the literature [40], [41], and are considered in this work as an effective index of the combined structure.

2.2.5 Semiconductor Properties

Band Bending

This explanation of the bandgap structure of a semiconductor is a simplified one that does not consider some of the material properties. This is sufficient for understanding this work as these devices have been extensively demonstrated to exhibit stable and high performance under regular operation. However, one must consider the surface properties as microscopic charge imbalances at the interface of the MQW can distort the bandgap of the superlattice. This 'band bending', which is extremely important for nano-scale devices due to their low volume to surface area ratio they should be dominated by the interface, which may influence the behaviour of the final nanolaser [42], [43].

Quantum Confined Stark Effect

Another well-characterised property of semiconductors is that in the presence of an electric field, the MQW structure can become slanted, which changes the effective energy of the transition, which can affect the output wavelength or result in peak broadening [30], [32].

2.3 Cavity and Resonator Physics

To understand how light can be contained within such nanoscale devices, we must first consider the most basic cavity, consisting of two opposing mirrors to reflect the light. We will discuss the substantial losses involved in regular mirrors. More advanced setups utilise refractive index contrast to force the light to remain within the cavity. This subsection will outline the fundamental physics behind this process and discuss the mechanism behind cavity confinement in general, before discussing whispering gallery mode resonators utilised by this work in depth.

2.3.1 Laser Critical Dimension

As discussed earlier, one of the key components of a laser is the cavity, which provides optical feedback. For certain configurations, the term resonator is used interchangeably with cavity, to describe the process by which only resonant wavelengths of light are confined whilst non-resonant light is dissipated. The simplest of such a cavity is the Fabry Pérot cavity; two plane-parallel mirrors can be used to trap the light within the gain medium. These mirrors maximise the chance of stimulated emission by forcing the resonant photons to have a longer path through the gain, but the key property of these mirrors is their separation, which forms the boundary conditions for the electromagnetic fields within the cavity. For this, the cavity must satisfy the condition for standing waves, and therefore must be proportional to the wavelength of the resonant photons, hence,

$$2\, n_{eff} L \;=\; m\lambda, \qquad m = 1,2,3\ldots$$

Where m is the mode number, or the number of standing waves, and L is the length of the 'laser critical dimension' of the cavity. In this case, it is the spacing between the two mirrors of the Fabry Pérot cavity. Note that the equation utilises an effective refractive index, discussed earlier as the combined refractive index of the gain medium, which can be used to estimate the minimum length possible for a laser, assuming the minimum mode number m=1, the minimum length L can be estimated by $\lambda/2n_{eff}$. This well-known condition is referred to as the half-wavelength condition, or the diffraction limit [18].

2.3.2 Total Internal Reflection

Considering the effective refractive index discussed, instead of two opposing mirrors, light could be confined between an interface of two different refractive indexes. Instead of the conventional descriptor of the speed of light changing as it goes from a refractive index n_1 to n_2 we can describe the light wave as a planar object, crossing the interface of refractive index contrast at an angle θ to the normal would result in light bending at the interface. Snells Law describes the relationship between the angle of incidence and the refractive indexes n of the medium:

$$n_1 sin\theta_1 \;=\; n_2 sin\theta_2$$

A consequence of this relationship implies that there must exist an angle that light passing from a higher refractive index material to a lower material would be reflected from the interface rather than bending into it. This critical angle $\theta_{critical} = \theta_2 = 90°$ can be substituted into the equation yielding the general expression

$$\theta_{critical} = \arcsin\left(\frac{n_1}{n_2}\right)$$

This core feature of refractive indexes at interfaces allows us to trap light within such interface contrast. This property can be used to ensure light can be confined within a higher refractive index active layer to a lower refractive index cladding, essential for use in fibre optics and other waveguiding devices, but more importantly, can be used for laser cavities of specific geometries.

2.3.3 Cavity Architecture

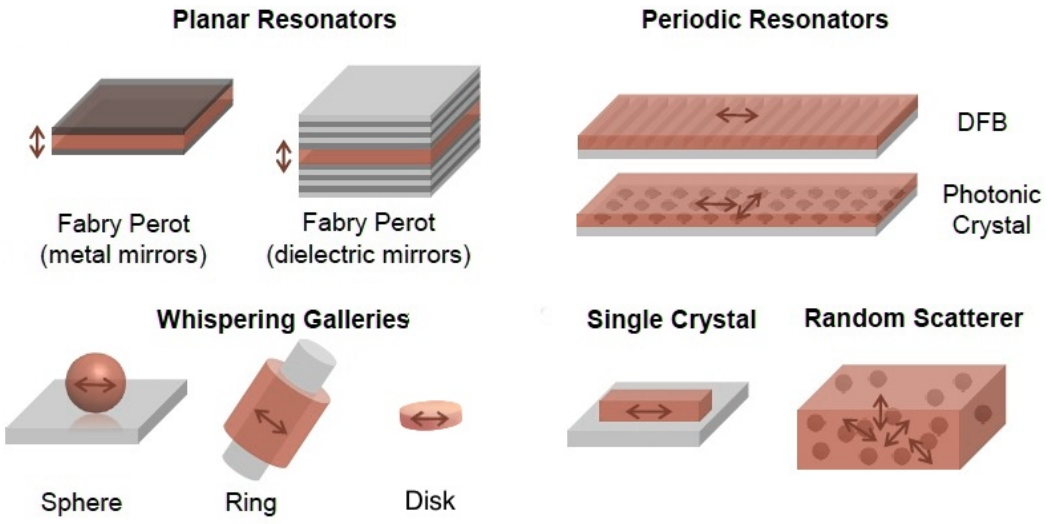

Figure 2.7 A collection of representative examples illustrating the variety of cavities for generating laser light. Adapted from Markus Karl Thesis [44]

By exploiting the properties and effects of refractive index contrast, the number of cavity designs and geometries possible can be expanded upon. Planar resonators that use a linear path with light confined between dielectric distributed Bragg reflectors (DBR) alternate high and low refractive indexes to force the incident planar light wave to interfere with itself and reflect, resulting in less lossy confinement than for metallic mirrors. The periodic resonators use the differences in optical path length created by the structure to confine the photons. Whispering gallery mode resonators utilise the

refractive index contrast at the interface to confine the light with total internal reflection around the circumference. Single crystals are very similar to the planar resonators, relying on the contrast at the interfaces reflect the photons to form a cavity from the long axis. Random lasers rely on the irregular spacing between scattering objects or nodes to provide the resonance condition. These are schematically illustrated in Figure 2.7.

The fabrication of high-quality optical mirrors is a complex and challenging task, and in the end, the sizes required for these components restricts the range of suitable applications, particularly at the micro and nanoscales. To miniaturise the dimensions these of resonators, a first obvious step is to maximise the refractive index of the bulk, for this work, $n\sim 3.4$ for III-V materials provides a good candidate in this regard. Finally, consider the geometry of the cavity.

2.3.4 Basics of Whispering Gallery Mode Resonators

For a dielectric resonator to perform with the smallest physical dimensions, limited by the wavelength of light, by instead the exploiting property of total internal reflection discussed earlier, it is possible to create extremely high performance, low mode volume resonators utilising whispering gallery modes (WGM) [45], [46].

The famous origin of the discovery WGM resonance is Whispering Gallery in St Pauls Cathedral. The behaviour of the sound waves in this gallery, long known to allow the overhearing of soft sounds over large distances with no apparent decrease in amplitude as one would expect in normal conditions. They were first fully described by Lord Rayleigh, observing that there were patterns of maxima along the wall (not, as originally thought, only at the opposite side), but no sound toward the centre of the room. As a result, he concluded that the sound waves 'stuck' to the walls and travelled along them across the room, interfering in such a way that maxima refocus in particular locations [47]. As with many acoustic phenomena, due to the wavelike properties of light and sound, it was inevitable that optical analogue would be created. This effect relies on the total internal reflection properties discussed earlier, ensuring that the angle at which light impinges on the inner interface of the sphere is never steep enough that it can be transmitted. An early study in 1961 used millimetre-sized dielectric structures of circular geometries, particular in solid-state spheres of CaF_2, which still represent some of the highest quality WGM resonators [48], [49].

2.3.5 Properties of WGMs

There exists no complete general solution for WGMs; however relevant properties can be extracted from geometric arguments from the optical path of light [46], [50]. For constructive interference to occur, light travelling around the circumference of a WGM resonator, the laser critical dimension, L of the cavity discussed earlier is now a circumference, such that L = 2πR. This means that the modes now obey the resonant condition

$$2\pi R n_{eff} = m\lambda$$

[18], where the left-hand side of the equation indicates the optical path length, and the right-hand side the wavelength and its mode number. This factor of two is less than a reflective cavity as for a WGM, the half-wavelength condition cannot result in a resonance condition as the WGM is formed from two counterpropagating travelling waves that form the whispering gallery mode, rather than a single wave in a reflective cavity. This simple equation can be used to estimate a wavelength of lasing from a measured diameter or the diameter from a measured laser wavelength. This shows that for a given mode number m, reducing the diameter relies on increasing the refractive index of the resonator. However, another essential feature emerges from this relationship.

Due to a large size compared to their radiative wavelength, the polymer microsphere WGM utilised in prior work [13], [51], supports multiple modes, with different m separated by a free spectral range (FSR). Aside from these modes emerging from the integer requirement for constructive interference, it is also possible to characterise these modes by the direction of the E field, defining the electric and magnetic Mie modes (commonly referred to in the literature as the transverse T_E and T_M modes respectively). They do not correspond perfectly to the traditionally defined transverse waves, so are sometimes called quasi-T_E and T_M modes due to the approximate polarisation of these modes, where the naming convention is inverted to those used in slab waveguides as they are defined by resonator axis rather than the path of propagation [52], [53]. The planar disk resonators developed for this work, however, are small enough that only one $m\lambda$ lies within the range of wavelengths supports gain. Additionally, the disks are sufficiently thin in the z-direction, and as the harmonic in-plane T_M has an E-field with only a z-component (180 nm) that there is likely insufficient gain for a T_M mode to be

supported [38], resulting in a single T_E mode operation, which are depicted in Figure 2.8 and Figure 2.9.

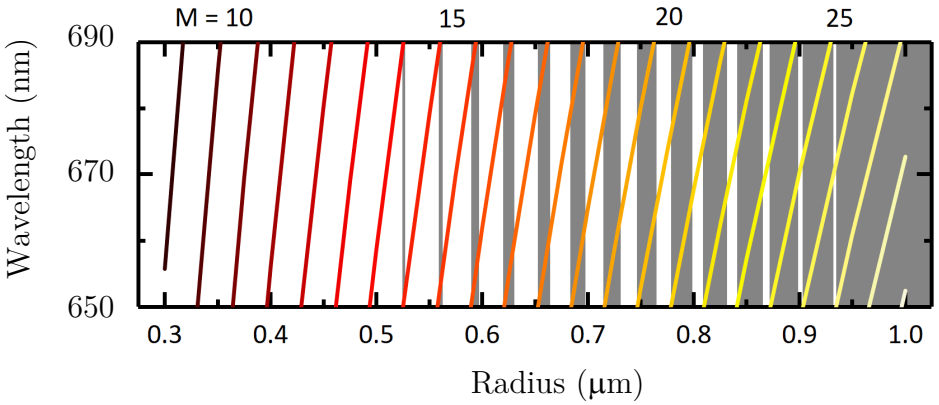

Figure 2.8 A map of modelled supported wavelengths in the material gain utilised in this work. The space between supported modes called the free spectral range (FSR) for radii<0.5, is sufficiently large that only one mode is supported [54]*. For such a 375 nm radius disk, an increase in diameter by 1 nm leads to an increase in emission wavelength of 0.84 nm. The gradients are linear. Figure reproduced from supplementary material* [55].

2.3.6 Scalar Wave Solution of WGM

Knowing both the diameter, the refractive index of the resonator material and the emitted wavelength as initial conditions allows for a calculation of n_{eff} which can be further interrogated to determine the refractive index of the medium surrounding the resonator into which the WGM partially extends through an evanescent component [56]. For this, we can move on from the geometric arguments to some modelling using electromagnetic solutions [57].

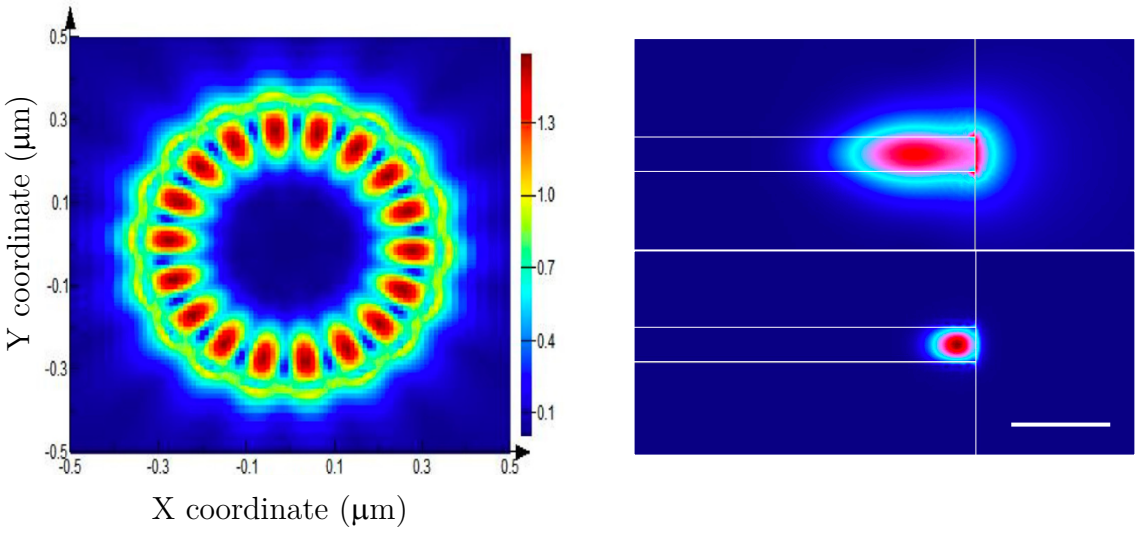

Figure 2.9 T_E Whispering gallery modes top-down cross-section for an 800 nm diameter disk, m=10 heatmap of the E field (left). Side profiles compared for two disk diameters, (right) 800 nm, illustrating the extent of the evanescent field (top), a 4µm disk with m=60 which has a far of more confined WGM. Scale Bar 500 nm. Adapted from Alexander Zagajewski, Master Thesis [58]

As these WGM are electromagnetic (EM) waves propagating in a dielectric material with a spherical/cylindrical geometric shape, their behaviour is dictated by Maxwell's equations. Though no exact solutions can be derived from the wave equation, approximations can be made for a useful model. Debye derived the solution for WGM from resonant eigenfrequencies for dielectric spheres, and through Mie scattering formulae, the separation of variables enabled by an enforced cylindrical or spherical symmetry can yield solutions [59], [60].

The latter solutions are extensively utilised to model the polymer microspheres were applied in attempt to predict the WGM behaviour of the disks. In particular, an EM analysis by Quan et al.[46] is used, reduces the dimensionality of the problem of a WGM in a spherical geometry to a planar structure. This enforces boundary conditions such that the edge of the cavity of radius a only changes the wave speed, and that the refractive index is a ratio of the wave speed outwith and within, it is possible to solve for the spectrum inside the cavity. This assumption to reduce the complexity of the system can be justified due to the equatorial symmetry of the WGM [59]. Two further mode numbers can characterise the modes in addition to m, the radial number (l) and azimuthal number (n). We can consider initially the scalar Helmholtz equation to describe the WGM coordinate:

$$\frac{\partial^2 E_z}{\partial r^2} + \frac{1}{r}\frac{\partial E_z}{\partial r} + \frac{1}{r^2}\frac{\partial^2 E_z}{\partial \theta^2} + k^2 E_z = 0$$

Where we have defined the wavenumber as a function of the frequency, permeability and permittivity respectively, as $k = \omega\sqrt{\mu\varepsilon}$. To solve the scalar wave equation, we can separate the variables into the form $E_z = R(r)\Theta(\theta)$ and then introduce a separation variable n to make two ordinary differential equations:

$$\Theta'' + n^2\Theta = 0$$

$$R'' + \frac{1}{r}R' + \left(k^2 - \frac{n^2}{r^2}\right)R = 0$$

Θ can be solved by defining an arbitrary reference line from which θ is measured; the separation variable n now represents the possible azimuthal modes.
For the two conditions it is clear that R has two solutions, for waves within the disk ($r<a$) and out with the disk ($r>a$). Equating the two solutions applies a boundary condition at $R_i(a) = R_0(a)$ to link the two results in the solution. The products of these solutions for R and Θ can be described using a series of Bessel functions:

$$\frac{n_1}{n_2}\frac{J'_n(k_1a)}{J_n(k_2a)} = \frac{J_n(k_2a)J_{\prime n}(k_2a) + Y_n(k_2a)Y'_n(k_2a)}{J_n^2(k_2a) + Y_n^2(k_2a)}$$

Where n_1 and n_2 are the refractive indices inside and outside the resonator, respectively. Approximate solutions of these Bessel functions can be made with asymptotic expansion [61], to solve for the position of the internal resonances.

It is, however, important to note that the scalar Helmholtz solutions that well described the larger polymer microsphere are of limited relevance due to the size of the proposed nanodisk resonators which approach the condition $\lambda \approx a$. Further calculations to more accurately predict the wavelengths of disks with different radii and in different media were obtained via finite difference time domain modelling (Lumerical) using the perfectly matched layer (PML) approach to obtain the complex eigenfrequencies for modes within the optical gain region (T_E mode |E| profiles in
Figure 2.9). PML thickness, z-distance, offset, and growth factor were optimised to avoid numerical instabilities [53]. Disks were modelled as solid isotropic structures with a uniform, isotropic refractive index of 3.6.

2.3.7 Quality Factor

The Quality factor (Q-Factor) can be used to understand the energy loss of a cavity during a cycle of the confined photons. It is also a measure of bandwidth ($\Delta\lambda$) relative to the resonant wavelength (λ), which are values that can be extracted from experimental data, such that $Q = {}^{\lambda}/_{\Delta\lambda}$. It can also describe a ratio of energy stored to energy dissipated per cycle as the wave travels around the resonator [52], so a higher Q factor would indicate that the energy stored inside the resonator is confined for proportionally longer [62], and therefore is related to the cavity decay time [63]. Alternative interpretations include the total energy of the circulating modes at equilibrium, indicating that for higher Q factors would result in higher intensity circulating modes at lower pump powers. It has a wide range of values, with nanorod lasers with Q factors of ~ 10^2 [64] with high-Q (10^3 to 10^6) characteristic of classic resonators like DBR mirrors [65], and ultrahigh-Q values recognised by nearfield WGM resonators (in excess of 10^7).

Radiative Q factors of spheres were modelled using a semi-classical (WKB) approximation for the Riccati-Bessel radial solutions [66] [67]. The Q factor for a given WGM mode can be approximated as

$$Q \approx e^{2mJ}$$

$$J = \tanh\left[\left(1 - \frac{1}{n_{eff}^2}\right)^{1/2}\right] - \left(1 - \frac{1}{n_{eff}^2}\right)^{1/2}$$

It can be noticed immediately that lower mode numbers, and hence smaller radii of the resonators, should have dramatically lower decreasing Q factors, which will result in a proportionally larger effective evanescent field.

As is apparent in the WKB approximation, and immediately visible in
Figure 2.9, the confinement and quality factor increases with increasing mode number, and therefore radius [47]. The more localised the modes, the less they leak out of the cavity and due to this tight confinement of the modes, such systems have very high intrinsic Q factors, reaching larger than 10^9 [49]. Therefore, High Q factor WGMs are localised near the edge of the cavity due to the effect of total internal reflection and exhibit better confinement than the majority of the other eigenmodes of the cavity.

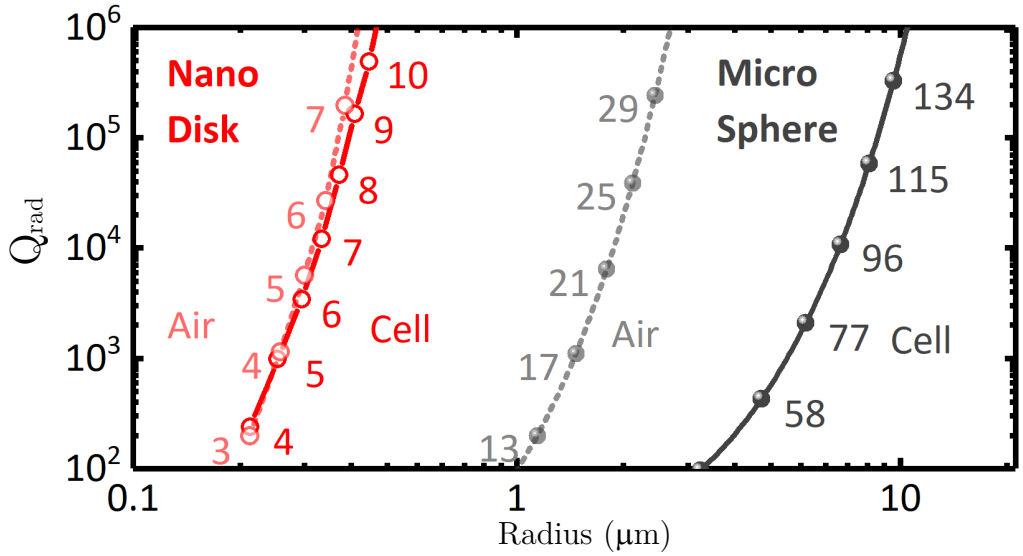

Figure 2.10 A graph of the results of finite element modelling (COMSOL) comparing the radiative Q factor for the lowest T_E mode supported in nanodisks and microspheres of different radii. Reproduced from [55]

Previous work utilising polymer preserved high Q factors in solution down to a minimum radius of 5-6 μm. The Q factors rapidly drop with size, which is a consequence of the insufficient contrast for total internal reflection

Figure 2.10) [68]. Here is where the high refractive indexes of the III-V materials are of importance, as the substantially higher contrast of n = 3.6 for this project resonator allows for an equivalently small resonator at 0.5-0.7 μm in diameter, with a 0.18 μm vertical dimension. This massive decrease in size potential allows for additional flexibility in applications which will be explored in this project. Additionally, modelling shows that the Q factors calculated for T_E modes are significantly higher than for T_M modes, which should result in the former dominating as the lasing mode.

It is important to note that what is modelled here is an intrinsic Q-factor, depending on the geometry, optical properties and dimensions of the structure. A general expression

$$Q^{-1} = Q_{rad}^{-1} + Q_{abs}^{-1} + Q_{ss}^{-1}$$

We can explain this expression of Q factor contributions using CaF_2 WGM resonators. It was no coincidence that CaF_2 was discovered as the first WGM resonator, as the material has very low absorption losses which enable it to maintain its experimentally derived ultra-high Q-factors (with records of 10^{12}). For resonators of this size, the Q_{rad} should be near-infinite, and the material properties are sufficient that the $Q_{abs} = 10^{14}$,

which would be the limit for a perfect resonator. Therefore, the limits to experimental quality factors are due to surface scattering Q_{ss}, which arise from defects from the material and fabrication as well as refractive index contrast [69], [70]. Advances in this fabrication process, including polishing and temperature annealing to reduce roughness of the crystal surface, which has seen some effort in the literature to model [49], which reveals that even for small contributions of surface roughness, which is expected of these materials can result in dramatically lower Q factors to 10^9.

The dominating Q_{ss} component for this example emphasises the importance on minimising surface scattering by ensuring a well-fabricated resonator. However, it is likely even with this included, that the instrument resolution, the spectrograph used for this work ($\lambda_{min}/\Delta\lambda_{disk} \approx 10^4$) will still be the principal bottleneck when calculating possible Q factors from experimental data.

2.3.8 Purcell Enhancement Factor

The Purcell enhancement factor is a commonly used term to describe the spontaneous and stimulated emission rates of a resonator, and it is also highly sensitive to size changes and may indicate another limit to the scaling down of nanolasers. This can be calculated by integrating over the |E| field (Figure 2.9) with respect to radius [71] we can calculate a mode volume (V) of approximately 2.6 $(\lambda/n)^3$, which is in agreement with typical such mode volumes for the smallest nano-scale lasers reported in the literature, and is comparable to the physical volume for the m=10 800nm diameter nanodisk $(\sim 7\ \lambda/n)^3$ [68], [72]. This combined with the calculated Q factors for such a disk, we can examine the Purcell factor, which gives a value for a laser emitters spontaneous emission enhancement [73].

$$F_P = \frac{3}{4\pi^2}\left(\frac{Q}{V}\right)$$

The Purcell enhancement factor for nanolasers, in particular, is a property of considerable interest, as the probability of spontaneous emission and stimulated emission greatly influences the threshold of the laser [71]. As there are no modelled effects of absorption and surface scattering in this work, we must use the experimental Q factors, which are limited by the resolution of the spectrometer ($\sim 10^4$). This results in a Purcell enhancement for the devices of this work in the range of 10^2-10^4.

2.3.9 Tunability and Sensing

Using WGM as refractive index sensors is one of the promising applications of this work/ Even small changes in the environmental refractive index can potentially result in a significantly altered resonant peak wavelength [47], [74], [75]. Further development, for example, coating or functionalising a resonator with a material of a refractive index that can be altered by adsorption of another substance can build on this potential by making the sensing much more selective [76].

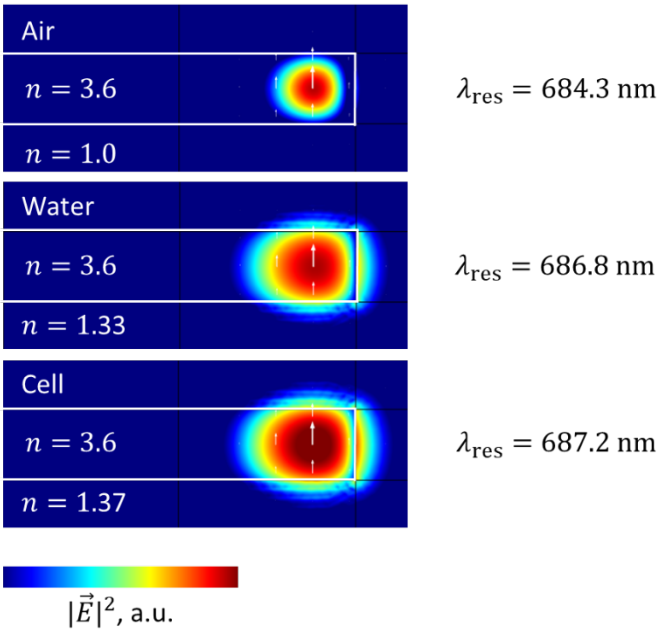

Figure 2.11 Finite element modelling (FEM) of the nanodisk laser that is the subject of its work, comparing the mode behaviour when subjected to different refractive index contrast (air, water, and inside a cell vs the isotropic disk). False-colour maps show |E|2 (in arbitrary units) of the lowest radial order TE mode that falls within the gain spectrum of the quantum well structure used in this work; λ_{res} represents the wavelength of the resonant mode in the three conditions. Reproduced from supplemental material of [55].

The sensitivity of a refractive index sensor is defined by $\Delta\lambda/\Delta n$ and is usually given in nm per refractive index unit (RIU). As described in Figure 2.11, the decreased contrast results in a higher n_{eff} which results in a detectable redshift of the system predicted to be around 10nm shift per RIU (Figure 2.11). Further work on the modelling of the system suggests that even higher sensitives of the order 180nm/RIU are feasible [58]. There are some additional properties to observe, however. As with the Q factor decrease,

the evanescent field extends further for smaller resonators (Figure 2.9). Smaller disks are therefore more sensitive to refractive index shifts than larger resonators.
Although competing models yield different results for the sensitivity of the disks to refractive index change, experiential analysis using solvents of known refractive index can be used to quantify this effect.

2.3.10 Other Sensing

This section will outline some of the potential sensing capabilities that have either been sporadically observed experimentally or have had some limited modelling. As discussed, whispering gallery modes are ultrasensitive to changes in the refractive index and size changes; this section is intended to describe the versatility of the nanodisks lasers and where future research and applications are directed.

Temperature
The evanescent field of a WGM is sensitive to external refractive index changes. However, thermal expansion could influence the optical properties of external material, or could result in a change in resonator diameter, which could potentially make it useful as a temperature sensor [77]. However it is important to consider both the thermal effects of optical pumping, as well as the likely an extremely small effect that might not be visible experimentally, with literature values for the coefficients of thermal expansion for the passive III-V semiconductors around 10^{-6} K^{-1} [78]. A 10K increase in temperature would cause a ~40 pm redshift in wavelength for a 750nm disk. Such a small shift might barely be within detection limits when accounting for other sources of noise. For the actively pumped medium it would be necessary, however, to ensure that the heating of the cavity via non-radiative thermal dissipation of the pump photons is not responsible for this shift, as well as an investigation of thermal properties of an active medium, which would be non-trivial and be a subject of further research [79].
Electric Field
Very briefly discussed in section 2.2.5 is the property of bandgap structures shifting when subjected to strong electric fields. Current research examining the quantum stark effect on quantum dots and semiconductor nanocrystals have shown merit for sensing neuronal voltage changes [80], [81]. This presents an area of future exploration, as certain shifts observed in the experiment could be a result of the stark effect, and as such is a subject of ongoing modelling and investigation.
Surface Modification

An effect that has been observed several times is an effective change in diameter when surface coatings are applied and removed. Likely, that this change is simply a result of a change in local refractive index, however, it could also be a result of band bending due to a change in charge carrier concentration. This could be refined further using coatings and selective binding sites. Such work has been accomplished as a biosensor by functionalising WGM resonators with groups that bind to molecules selectively, allowing for a local change in refractive index [16], [82], [83]. This angle of research is highly promising for biosensing in general, as lack of selectivity is a significant downside of pure refractive index sensing, but this also has substantial promise for lab-on-a-chip applications.

2.4 Photon Pumping

This final section briefly discusses the different pump sources utilised in this work, as well as a more specific outlook on the lasing mechanisms with the previous sections as guidance.

Lasers, in general, can be divided into three main categories: continuous wave (CW), pulsed and ultrafast. These describe the temporal profile of the laser, where CW means isotropic in the temporal space, while pulsed and ultrafast indicate a temporal profile that is periodic. The distinction between a pulsed laser and the ultrafast laser is arbitrary often a pulsed laser is >1 ns wide pulses and ultrafast is <1 ns [84].

Continuous wave lasers emit at a constant intensity. Compared to pulsed lasers and ultrafast lasers, the average power is similar, but over the short timescales, the peak power of a pulsed laser is significantly larger. When pumping the nanolasers of this work, a pulsed laser is used where the pulses are longer than the decay time of the resonator (a factor related to the Q factor as previously discussed) [4]. Additionally, a laser in CW operation could experience detectable, homogenous peak broadening as a result of a larger linewidth enhancement factor [35], [85], [86].

Using ultrafast lasers with picosecond or shorter pulses yield such high peak powers that they can force even normally non-interactive matter to have a strong light-matter interaction, overcoming the delay times for population inversion, and minimising the threshold. However, the interaction is so significant that it is likely that carrier overflow would result in changes to the refractive index of the material [87], [88], resulting in a 'chirp' or a wavelength distortion that results in peak shoulders [31], [89]. In this work, all three categories of lasers were used, with CW typically used for imaging, the majority

of the work was done using pulsed lasers, with some preliminary investigation of ultrafast lasers.

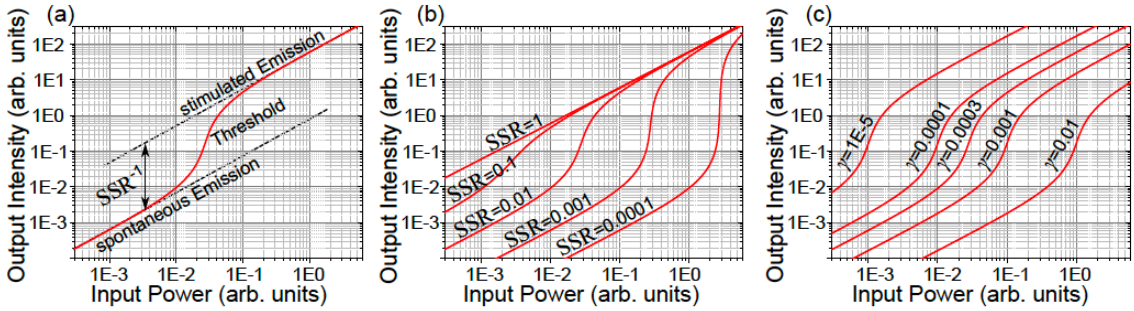

Figure 2.12 Threshold characteristics of a microcavity laser. a) A representative example of a threshold with SSR^{-1} = β=0.01 and a decay time γ. b) examples of different threshold characteristics for a β approaching 1 – a threshold-less laser. c) the effect of decreasing losses to the system is represented by varying cavity decay times. Reproduced from [90].

To characterise the threshold discussed in Figure 2.2, we measure the pump energy being delivered to the system and then extract from that the intensity of the excited peak. We also measure the light emitted by our laser for each pump energy. This allows us to plot a light in – light out curve, which can then be analysed to extract the spontaneous to stimulated emission ratio, SSR, where the inverse is defined as β factor [91]. When modelling such a system, we can derive an expression from the rate equations to give

$$I_{out} = \frac{k}{2\gamma}\left(I_{in} - \frac{\gamma}{\beta} + \sqrt{\left(\left(I_{in} - \frac{\gamma}{\beta}\right)^2 + 4\,\gamma\, I_{in}\right)}\right)$$

Where the dependence of the equation is depicted in Figure 2.12. From this, the threshold can be extracted from the β factor by plotting the experimental data: I_{out} – the intensity of output light integrated over a lasing peak, and I_{in} – the intensity of input light measured by power meter, and iteratively varying the constant factors cavity decay time γ and arbitrary constant k to fit the curve to plotted data.

2.5 State of the Art

Currently, there is a great deal of interest in the fabrication and optimisation of nanoscale devices. This section is a brief discussion on the current state of this research and where the work in this thesis resides [4], [6], [33].

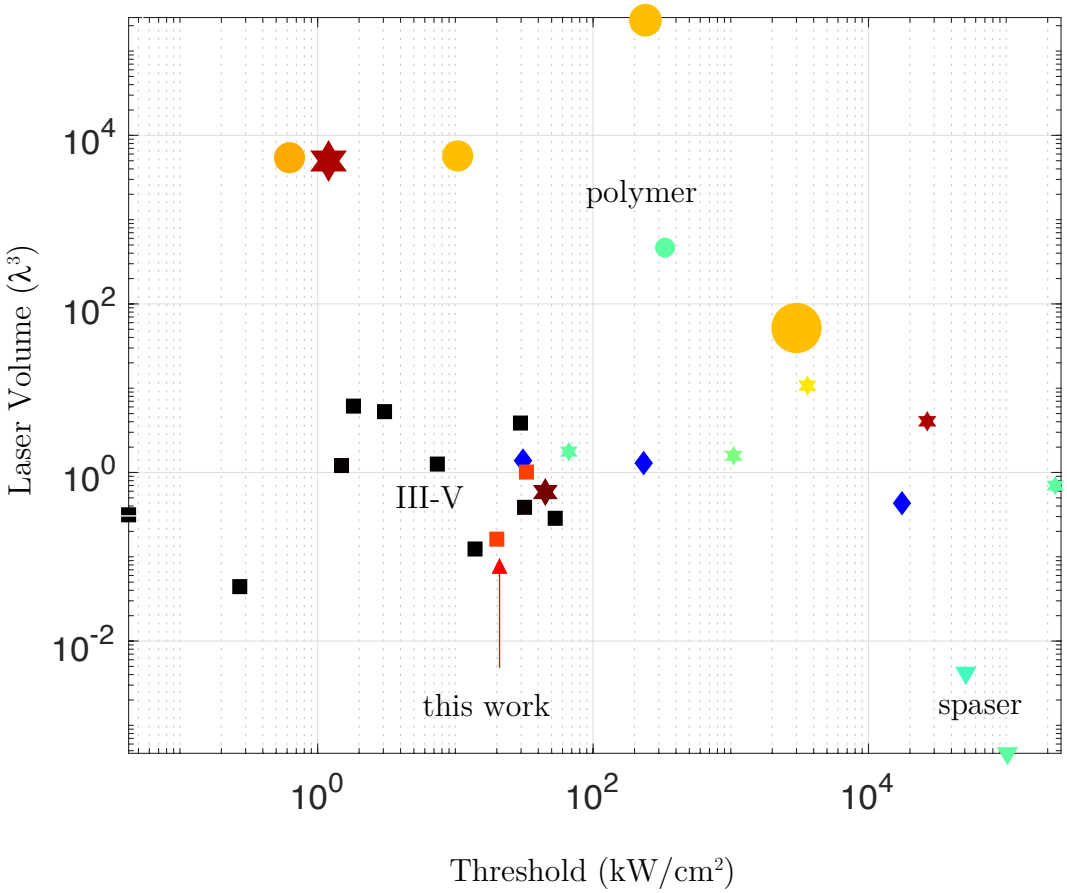

Figure 2.13 - A selection of the micro and nanolasers published within the last two years that operate at room temperature. The size of the markers is scaled to the laser critical dimension L, and are coloured according to their laser wavelength (infrared = black). The majority of perovskite (star) and III-V (square, diamond) nanolasers are fabricated to emit in the infrared and GaN (shown separately as diamond) with polymer and silica doped resonators (circles) as visible emitters. Spasers (triangles) utilise plasmonic resonance to trigger lasing and achieve the smallest sizes but require considerable energy density [92].

Pushing the limits of physical dimensions for all laser emitters requires a compromise between threshold and volume. Some of the latest research is plotted in Figure 2.13. For dielectric materials, the size restriction is the contained wavelength limit as discussed, however much smaller plasmonic devices (Spasers [15], [93]) can produce lasing at sub-diffraction limit sizes around 100 nm. To create lasing they also require a high threshold in terms of power density, which creates thermo-acoustic shock bubbles around the nanoparticles. Perovskites have been demonstrated with both large sizes and ultra-low

thresholds, as well as high thresholds in small sizes, which demonstrate the balancing act between size and efficiency [94]–[96]. Another consideration is the wavelength of emission, the majority of the micro/nanolasers developed are near or mid infra-red emitters, focusing on the compatibility with telecoms systems [6], [68], [92]. For this work, visible or very near IR emission is highly desirable for its compatibility with currently used fluorescence imaging and spectroscopy techniques. Short wavelength GaN emission, would scatter strongly optically complex environments of biological matter [97], [98]. The nanolasers utilised in this work find a minimum for physical dimension and power density required for threshold, while maintaining visible emission in the visible (red) spectrum.

2.6 Contributions

The modelling for the nanolasers, concerning Q factor analysis and mode positions was contributed by Markus Karl (PhD Student, Professor Gather's Lab), whilst Alexander Zagajewski (Masters student, Professor Gather's Lab) confirmed and furthered this work with a focus on mode profiles and sensitivity. Andreas Mischok (Post-doc, Professor Gather's Lab) provided guidance on the characterisation of the threshold behaviour of microcavities.

Fabrication

This Chapter aims to describe and explain the fabrication process for the III-V semiconductor nanodisks and random network structures. The literature for the processing of these materials is extensive, and this Chapter will discuss the most prominent methods used to create similar structures, their advantages and disadvantages, and why they were or were not selected and how they were optimised for the production of the desired structures. The structure of the Chapter will first discuss the broad outline of the wafer design and the intended outcome of the desired structures concerning the fabrication process, then discuss patterning, different etching approaches and finally discussing encapsulation and functionalisation of the structures.

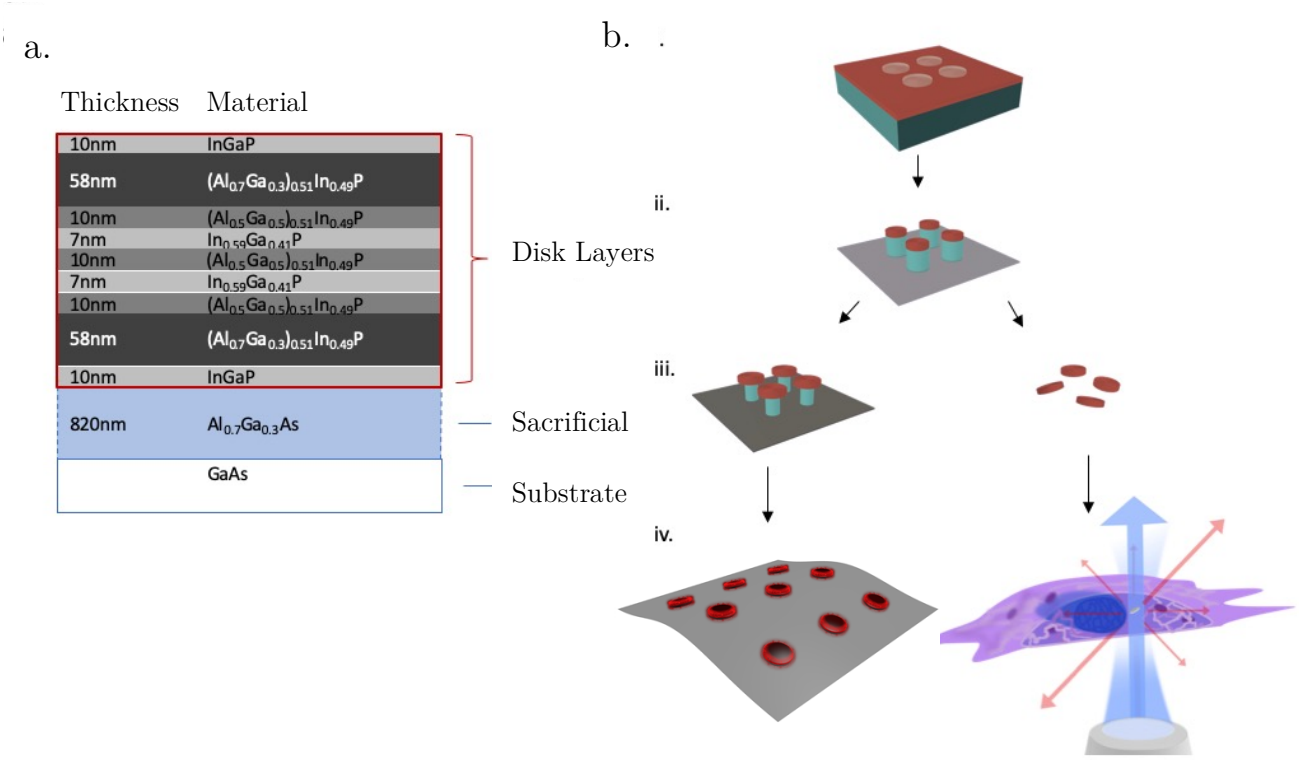

Figure 3.1 a) The wafer structure used in this project, with emphasis on layer thickness and elemental compositions (darker shades used to highlight a higher aluminium content). Red outlined region constitutes the final disk and network structure. In light blue is the sacrificial layer, which is selectively removed to release the disk from the substrate on which the crystal is grown. b) Simplified overview fabrication route, here the red outlined region in a) is simplified to the top red layer, and the sacrificial layer is in blue and GaAs substrate in grey. Steps i-iii can be used as a visual reference for the structure of this Chapter with step iv. represents the aim of the fabrication process with the applications to be discussed in Chapters 5 and 6.

3.1 Outline

To make high-quality optical nanostructures, semiconductors made of crystalline alloys of elements from group 3 and group 5 of the periodic table are used, henceforth referred to as III-V semiconductors, which were introduced in Chapter 2. Generally, high-quality semiconductors are produced from wafers grown using an epitaxy process, where atomic layers are deposited on a substrate, resulting in a multilayer Quantum Well (QW) superlattice structure described in Chapter 2 and depicted with emphasis on aluminium concentration in Figure 3.1 a [99]. To produce features and devices from these highly uniform crystals, a process referred to as lithography is used, which is a widely explored field with many approaches depending on the nature of the materials and their arrangement. For this project, two such approaches were used as illustrated in the

schematic of Figure 3.1 b [100]. This is done first, by defining the desired features using a 'mask', commonly a cross-linkable polymer or ceramic, followed by a controlled removal of the un-masked material, or etching stage. The different approaches to this step are explored in this Chapter, detailing their advantages and disadvantages to optimise the quality and outcome of the desired structures [47], [48], [101]–[103]. For the disks described in this thesis, a two-step chemical removal or 'wet etch' is employed. Though often described as a more uncertain etch than the 'dry etch' alternative that ablates material with accelerated plasmas, it is desirable for its speed, simplicity and its ability to mass-produce structures while minimising damage to the QW structures [68], [104], [105]. For more precise structures like the random networks, the first wet etch was replaced with a dry etch process which does have superior control and resolution, but with other disadvantages which will be discussed in depth in the following sections. Finally, the sacrificial layer can be removed, either partially, for more controlled characterisation or to transfer the structures onto other substrates as a transferable photonic structure, or completely, to have the disks as a freely suspended resonator, allowing them to be inserted into biological cells or onto other substrates.

3.2 Patterning

The principle drive for the use of III-V materials illustrated in the previous Chapter was that the higher refractive index and gain allows for the production of further miniaturised WGM resonators than the previously demonstrated polymer microspheres. However, a further advantage of producing intracellular lasers from a semiconductor quantum-well structure epitaxially grown onto a support wafer is the availability of well-established photolithography and electron beam-based nanolithography processes to accurately control size and shape [103]. These processes will be explored in this section, as the top-down lithographic process utilised has to be carefully selected to both remove wafer material in a controlled fashion and control surface defects which impede the performance of the desired structures [102].

This is particularly sensitive for the proposed structures in this project, where roughness or any deviation from circularity would reduce the resulting Q-factor [101], which needs to be as high as possible for the best lasing performance. The theory and modelling from Chapter 2 indicates that the Q factor, which faces sharp decreases with decreasing size, is already nearing instrument resolution assuming a perfect sub-μm structure [68].

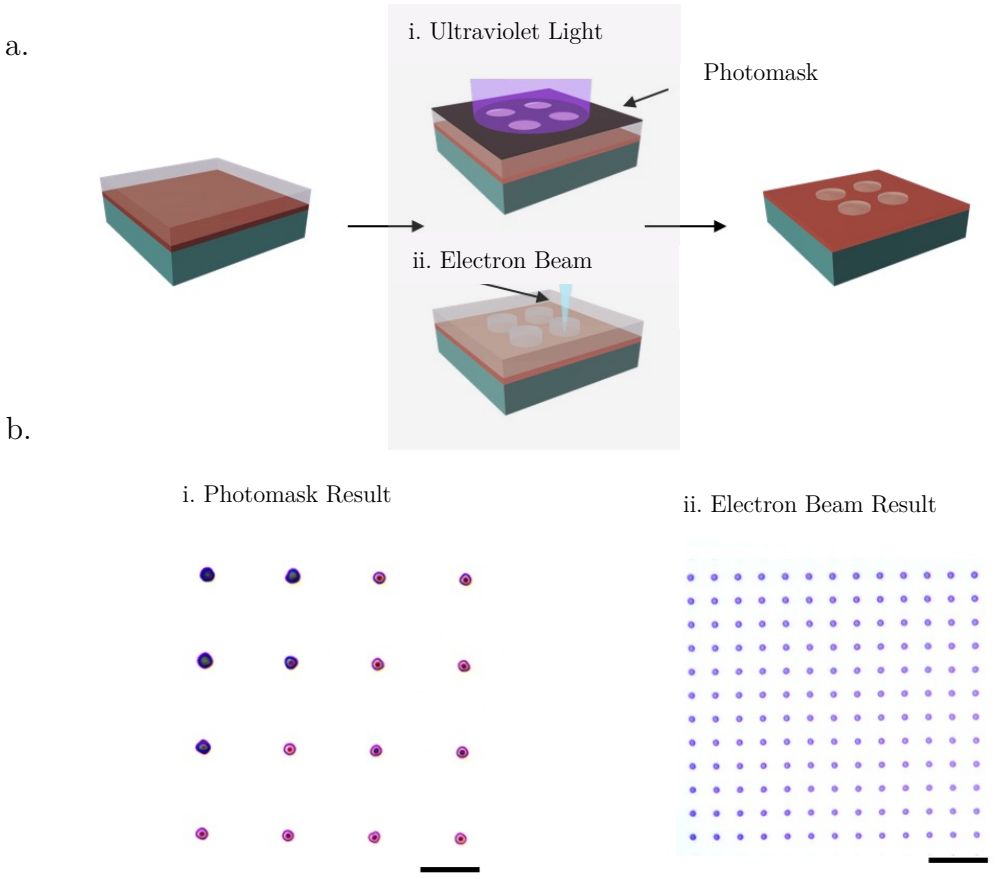

Figure 3.2 a) Schematic of photoresist patterning methods, with experimental result comparison. To crosslink the polymer, two approaches are compared: i. A schematic of the UV lithography exposure process, which needs a photomask, ii. Represents electron beam lithography which uses a focused electron beam instead of a photomask. b) Microscope image of resulting nominally identical mask structures, i. Indicates the photolithography result, note irregularities in the shape and size, as well as colour, indicating thickness differences and overexposure effects. ii. Electron beam lithography, with a denser, more regular better-defined structures. Scale bar for both 10 μm.

To define the pattern where the wafer is protected from the etch process, there are two principal techniques: photolithography and electron beam lithography were investigated by this project (Figure 3.2). Both the patterning technique and selection of the mask material use must consider the following etching steps, which will be discussed in the following sections. To illustrate why such considerations are important, consider another commonly used technique in the processing of semiconductor materials, which uses scattered polymer spheres as a 'shadow mask'. Dry etch processes that utilise accelerated atoms at ultralow vacuum pressures do not have sufficient energy or momentum to disturb the position of the macroscopic spheres, but the highly directional etch process casts a shadow, etching the 'illuminated; areas resulting in a circular mesa where the

'shadow' was cast [106]. However, it is immediately evident that this system would not work in a wet etch, which would immediately wash off the mask.

For this thesis, spin-coated polymer resists are favoured for wet etches for their adhesion to the substrate. Polymer resists are also compatible with dry etches. However, resist material chemical compatibility must be accommodated for; Hydrofluoric acid (HF) for example, permeates through thin polymers and etches ceramics rapidly [107]. Lift-off is also an issue with some polymers, which do not tolerate strong acids or oxidants, especially for small structures like the disks. The epoxy-based polymer SU8-2000.5 (MicroChem) is used throughout this project, as it has good chemical stability, thermal stability, a low glass transition temperature and can be processed to have excellent adhesion to surfaces, as well as requiring a reasonably low dose to crosslink. The typical process for a 500nm resist used a 5 krpm spin of the polymer, followed by a 1-minute soft bake at 60ºC and then followed by a 4 minute bake at 90ºC before exposure, where the gradual increase of temperature reduced the rate of bubbling. For thinner mask structures, the polymer could be diluted in cyclopentanone. Ratios of 1:1 and 3:1 were used for 200nm and <100nm thickness, respectively, an essential property for making high precision structures like the random networks. Polymer resists are either described as negative or positive, depending on whether the exposed area remains (negative) or is removed (positive) when exposed to a selective solvent, called a developer, which for SU8 is Ethyl Lactate.

3.2.1 UV Photolithography

Initially, the project used UV photolithography to crosslink the SU8 to form the masks, capitalising on the low exposure dose required, which reduced the time required and complexity of the fabrication. This process, (Figure 3.2 a.i.) uses a shadow mask of UV absorbing/reflecting material, for this project was chromium, deposited on a UV transparent material (quartz) to determine where UV photons react with the sample. Using a 365nm UV light source in a mask aligner for 60 seconds (Karl Suss MJB-3) was sufficient to expose a full area, however, such long periods accentuated the overexposure and irregular patterns. Therefore, a more intense source (EVG620, EV Group) required only 8-12 seconds to define circular disks, depending on resist thickness. A 2-minute post exposure bake follows the exposure for both. The principal advantage of this process is the simplicity and time, being able to expose an entire sample with a regular pattern defined by the shadow mask. The shadow mask was designed using AutoCAD and

prepared by Compugraphics, Glenrothes, with considerations of the different sizes and ranges expected to be required by the project.

However, there are significant shortfalls for disk caps and resulting structures by this method (Figure 3.2 b.i.). Principally the lower limit of the feature sizes possible in UV lithography are substantially larger than the smallest desired nanodisk lasers and any of the network structures. This is because UV photons diffract strongly through apertures of less than 2 μm. However, for specific applications larger disks are desirable. As described in Chapter 2 and further explored in Chapter 4, multimode emission can be used to precisely determine disk size. To pattern the smallest structures, extremely thin SU8 must be used, to reduce diffraction and overexposure in the SU8, as well as bringing the mask into 'Hard Contact' with the sample surface, again to reduce vertical space for photon divergence.

Consequently, this necessitates that the sample is perfectly clean and flat, as defects will result in tilt and thus a gradient of exposures. These conditions are challenging to ensure, as the samples are very small, resulting in 'rocking' when the mask is brought into contact. Also, the nature of spin coating results in a small variation of thickness towards the edges of the wafer. The consequence is a gradient of sizes and exposures, as seen in the colour and size change in the disk mask in Figure 3.2 b.i. Finally, the quality of the mask significantly impacts the output mask, and cannot be corrected for in the patterning process, but can be accounted for in the etch process.

3.2.2 Electron Beam Lithography

To address the shortcomings of UV lithography, an alternative patterning technique was explored. Much like an optical beam, electron beam lithography (EBL) guides the electrons using electrostatic lenses and apertures to control the beam size. The process is illustrated comparatively to photolithography in Figure 3.2 a.ii. For this patterning technique, there are a variety of different considerations to be made that are not as important for UV photolithography, firstly because SU8 is a negative resist, it becomes necessary to minimise the processing time, as the area exposure is done through a 'writing', maskless technique, where the controller (a Raith E-line plus), uses a focused beam of electrons to 'write' to expose the resist (Figure 3.2 b.i.) [108]. Therefore, if one can minimise the dose and area exposed by selecting the resist with the smaller writing area, one can minimise the amount of time the write takes. Both the disks and networks

are small structures that are relatively distantly spaced, so SU8 is well suited as a negative resist, developed for 60 s in ethyl lactate after a sample of millions of disks can be patterned in a few hours. Alternatively, one could reduce the write area but keep the popular positive PMMA resist and use EBL to write 'rings' around the desired disk structures [37], but the large doses required for PMMA and the number of disks required by the project make this resist unsuitable.

To optimise the quality of the structures and the patterning time, the following parameters were used: To define the disks seen in Figure 3.2 b.ii., an area dose of 5 $\mu C/mm^2$, an aperture of 10 μm and a beam power of 30 kV was used. The pattern of disks of desired size ranges was then patterned at a high density (up to 5 disks per 10 μm^2, compared to 1 disk per 10 μm^2 for photolithography). The design of the pattern could be modified to introduce a size increase to ensure the maximum range of wavelengths supported by the gain spectrum. This was accomplished either by patterning four closely spaced diameters and relying on inhomogeneity in the etch step to provide intermediary diameters or using a more involved design increasing the diameter in 1nm step sizes, but this seemed to result in much longer write times. The networks are still being optimised during the writing of this thesis, but to ensure that the nodes are not affected by multiple exposures or charging, a 7 μm aperture and proximity adjusted dose corrections were used to compensate for overlap of the pattern at the nodes, which would otherwise be overdosed. The final result for the disk structures (Figure 3.2 b.ii), produced with EBL has the desired reduced size and increase in density of objects, which optimises the wafer material usage. Additionally, the improvement in the outcome of size, shape and dose control compared to that of UV, enables confidence for the development of the smallest disk structures and network structures.

However, along with taking substantially longer than UV photolithography and requiring expensive instrumentations, there are some unexpected disadvantages. For the disk samples, EBL exposure generates a 'charging' effect, which results in a 'musk', or a thin (<10nm) layer of crosslinked mask that covers the unexposed areas of the substrate and resists etching even if no pattern is written. This effect does not occur in silicon control samples, and the working hypothesis is that the electrons do not just penetrate the wafer surface, but travel across significant distances, crosslinking the observed layer of polymer on the wafer interface. Lower doses were trialled as a possible solution, but instead of reducing the monolayer, the resulting SU8 mask was underdosed, with problematic loss of the desirable adhesion properties. Extended development periods

were also trialled, but this also resulted in a loss of adhesion. To accommodate for this effect, EBL samples require an initial cleaning step to remove this monolayer. The required cleaning step was a 60 s low power (20 W) 200 sccm O_2 RIE. However, the cleaning process requires that the resist is not diluted, as the substantial (up to 300 nm) reduction in the thickness of the SU8 caps during the cleaning step to remove the monolayer would also remove the thinner SU8 in its entirety. However, this can also clean the sample of any debris and organic contaminants from the development stage, which could interfere with the etch process. If the wafer is cleaned with this process for longer than 1min and 30s, the exposed wafer resists the following wet etch process, presumably as the surface becomes oxidised. The areas 'masked' from the cleaning process by the SU8 are not passivated in this way. While initially undesirable, this oxide etch stop has a valuable property and will be explored later. The second reason to have thicker resist is mechanical, a thinner resist will 'sag' as the acid under-etches the mask, restricting the diffusion of the acid and its products. A 'curing' step is introduced after development (20 minutes at 180°C), at which temperatures the SU8 undergoes a glass transition, which reduces the 'sag' and improves the adhesion of the smallest disk caps.

Considering both of these techniques, the UV photolithography has utility for rapidly producing samples and patterning larger disks, where the definition of the edges is not as crucial as Q factors are substantially large. It does also reduce the number of additional steps by allowing disks to be etched without a cleaning step to remove the EBL introduced monolayer or requiring that the SU8 is 'cured' to improve adhesion to compensate for the smaller size, which also allows the disks to be smoother than expected, exploiting the mechanical effects of the much thinner resist.

However, EBL is predominantly used in the project as it is far more versatile, allowing for better quality masks, optimal use of wafer material and the definition of smaller disks with specific sizes as required by the planned experiment, as well as more complicated polygons and the random network structures, and can avoid whole sample aberrations from induced angles in pre-patterning alignment steps. The additional complications in the development and cleaning steps arising from the formation of the monolayer are undesirable, adding further time and complexity to the fabrication process. Beyond the scope of this project, samples where EBL requires the thinnest resist (such as the random networks) this charging effect should not crosslink different resists, such as HSQ or Flowable Oxide, which require much greater doses so, will be explored in future.

3.3 Etching

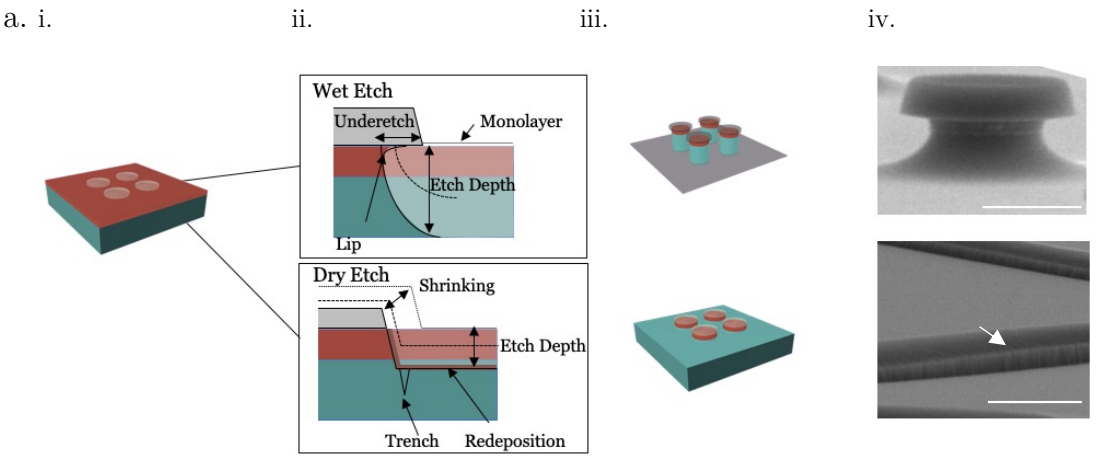

Figure 3.3 a) i-iii. Comparative schematic of etch techniques, with emphasis on the different challenges that each presents and an idealised outcome, as well as illustrations for specific terminology. iv. SEM images of a typical column (wet etched) and network structures (dry-etched). Note the rough boundary of the dry etch (white arrow) exposed surface compared to the smooth surfaces of the wet etch. Scale bar 1 μm.

Etching refers to the controlled ablation of material to define a structure from a mask. This can be done with dry or wet etching, which will be described and compared in detail here, as both techniques were explored for this project. Wet etching describes a purely chemical process using corrosion and solution to remove the wafer material. This distinguishes it from the directional plasma etches which are commonly referred to as dry etches, where some of the significant etch behaviour differences, results and specific terminologies are summarised in Figure 3.3.

3.3.1 Wet Etching

Wet etchants are superficially very attractive for the fabrication of microscale devices. They do not require expensive equipment; the etch is often extremely rapid so that the devices can be made promptly, the chemistry of the etchants can be adjusted to selectively etch different layers and directions with respect to crystal properties. They are often described as a route to mass production, allowing for the formation of complex and smooth structures with relative ease [101]. However, these chemical reaction are sensitive to a wide range of environmental conditions such as temperature and humidity, which can cause irregularities in etch rates, reducing the reliability of the process [109]. The etch homogeneity throughout the sample is also not as reliable as its dry etch

counterparts, with characteristically more rapid etches around the sample boundary [103]. To understand these properties, and how they can be better controlled, it is worthwhile to understand wet etching on a more fundamental level. One would start with a soluble reactant molecule which undergoes a process of transport to the active surface: initial adsorptive binding, reaction of the reactant to the surface, reaction product desorption, and then finally transport of the products away from this surface [110].

For this project, a wet etch was devised after comparing the various explored options in literature [100], [105], [111]–[113]. The crystal structure for the AlInGaP MQW is compatible with a wet etch, as typical GaAs crystals have a different surface activity depending on which face is exposed [114]. Arsenic faces have more unsatisfied bonds, which allows for recombination as well as etching faster than the Ga, which tends to expose crystallographic defects [115], [116]. However, despite being based on the crystal structure of GaAs, the principle challenge involved for this wafer material is the MQW structure, which contains several high aluminium layers followed by zero aluminium containing layers. Aluminium oxidises quickly, but its oxide is typically difficult to remove in acidic solutions [110]. This presents a difficulty for a wet etch, as this can dramatically change the selectivity, and therefore etchant required for the different layers in place of crystal faces. If the rate of desorption of oxidants of the aluminium layers is rate-limiting, then the surface will not be smooth.

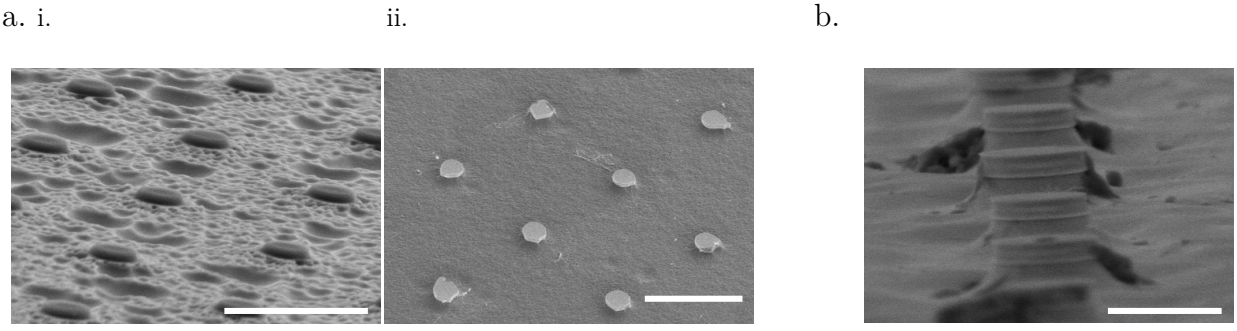

Figure 3.4 HBr etch stages. a. i. within the first few seconds the acid etches downward into craters. ii. After 7 seconds the resulting substrate is more smooth, but disks are not ideally circular. Scale bars 5 μm b. Final HBr columns are smooth, vertical and circular for etches of more than 10 seconds. Scale bar 1 μm.

To control the etch, we need to know what part of this process we are limiting. The most straightforward method to reduce acid etches is to dilute them, but to ensure that the etch is non-selective, we have to consider the reactivity of the different layers of the

MQW. This rules out common acids such as phosphoric acid (H_3PO_4) and hydrochloric (HCl), as they will preferentially etch the aluminium containing or InP layers, respectively [6], resulting in undesirable stepped structures [105]. Hydrobromic acid (HBr) in addition to being non-selective to AlInGaP/InGaP, results in smooth surfaces, making it highly desirable in the fabrication of microdisks in III-V materials [108], [117]. Additionally, the acid etches down in pores 2-3 times faster than sideways, though the rate is not well controlled, and seems dependent on many variables. The profile of the mesa-like columns (Figure 3.4 ii) [118] suggests a 110 crystal direction preference, but the pitting may suggest that there is an electrochemical contribution, for which the mechanism is not well understood [119].

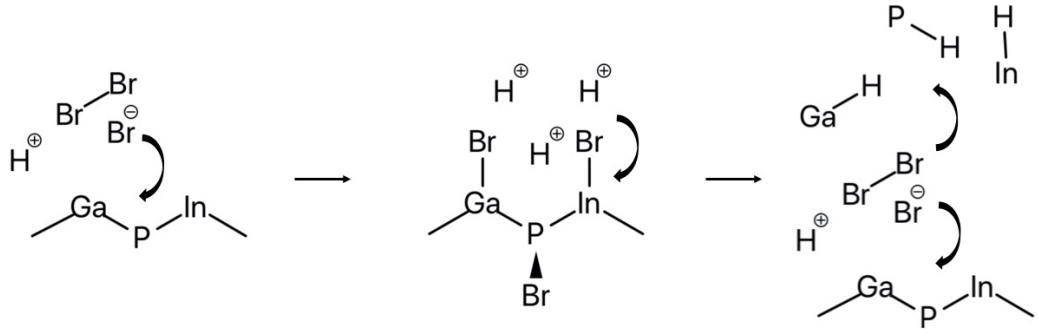

(3.1)

To reduce selectivity further, we can add an oxidiser to the acid. Typically used are peroxide and chromate, but for the materials to be etched here, elemental bromine is a better candidate [105]. In addition to being extremely desirable as an oxidiser, it also acts as an oxide remover [116]. In combination with HBr acid, which now complexes the resulting brominated bonds via protonation as depicted in Equation (3.1) [105], [120], the resulting ratio with water as a dilutant can both minimise mask undercut, and also be extremely non-selective for the layer, allowing for a mostly anisotropic etch, an often-touted unique advantage of the dry etch technique [105]. The ratio with the most reliable rates utilised for this project was determined by trial and error was 2:5:100 Br_2:HBr:H2O. This has an etch rate down 1 μm in 10 s, and etches under the mask between 300 and 500nm, with the resulting columns shown in Figure 3.4 a.ii. However, the acid has occasionally etched much faster and with isotropic proportions (possibly a result of dilution [117]) which has resulted in the unusable samples. These significant differences are difficult to explain with solely environmental explanations, as the temperature and humidity of the cleanroom are well controlled (22±1 °C and 44±2 % respectively). Therefore, the origin of the significant variability must be due to the mixing process, ingredients and sample condition. These factors can be controlled to an extent, the acid mixture is prepared fresh each time and used within 5 minutes of mixing. It is a known

phenomenon that the reactivity of acid mixtures diminishes with time [103], [121]–[123]. This should, however, be over much longer time scales than used in practice, and different etch rates have been observed for nominally identical samples etched simultaneously. The water has shown considerable influence on the reaction, as the purity of the water will change the behaviour and etch rate of the acid [103]. There are substantially slower, but more unpredictable etch rates with the cleanroom tap (10-12MΩ) water compared to using MilliQ deionised water (18.2 MΩ), where the resistance increases with fewer contaminants, which has resulted in the smoothest side walls and most reliable etch rates. This water must be collected fresh from the MilliQ source in the School of Medicine; stored water also produces unpredictable etch rates. Organic contaminants have been observed to be introduced by the RIE in its cleaning process and can also negatively affect the etch rate. This can be mitigated by a pre-cleaning step using a Hydrogen /Argon and Oxygen ash at high power (100W) before the samples are treated. The etch process is particularly highly sensitive to this sort of carbonaceous contamination [124], [125].

The temperature of the water was also controlled by pre-warming to 23°C, which allowed the final acid to have a more controlled and reliable final temperature. Any hotter and the etch rate would be substantially accelerated, as it affects both the transport and reaction of the oxidiser and complexant. The sample was etched immediately upon removal from the RIE cleaning step, as an oxygen coating from atmospheric contact over a period of hours also inhibits the etch. Methanol was briefly considered as a solvent for the acid mixture. Though commonly used, it is less viscous than water which results in a more isotropic etch due to better reactant and product transport, which is not desirable for this project in either instance [126].

Controlling for these factors, the principal disadvantage is the speed of the etch, and the significant uncertainty in etch rate (±20 nm/s) in successful etches, disregarding those that etch the structure entirely or not at all. Further dilutions result in unpredictable and inhomogeneous results, sometimes with no etching visible, which is likely due to a bottleneck of desorption, as the brominated bonds are easily protonatable, but not soluble in water [113]. Also, the etch must be 10 seconds or longer, as etches around 3 seconds show the irregular ‘pitting’ consistent with downward pore etches of the HBr. Etching for around 7 seconds will expand the pits and lead to a mostly smooth surface but will result in irregularly shaped disks (Figure 3.4 i). After 10 s, the irregular shapes are smoothed by the action of the oxidiser (Figure 3.4 ii). This suggests the source of

uncertainty and lack of control of the etch rate lies in the ratio of oxidiser and acid complexant.

Reducing the acid concentration did initially show some promise in reducing the etch rate, (1:1:50 ratio) however, has shown less anisotropy than expected and resulted in greater unpredictability between samples. Reducing the bromine in the ratio 0.1-0.5:5:100 resulted in very inhomogeneous and uncontrolled etches. This indicates that the ratio between the acid component and the Br oxidiser is reduced such that the Br_2 is the rate limiting component, which presents an issue as elemental bromine easily evaporates at room temperature, particularly in the mixing process and therefore cannot be relied upon to define the etch rate. Therefore to ensure a consistent reaction, it was concluded that it is essential for the reaction depicted in Equation 3.1 to have reliability and reproducibility, that HBr must be in excess of the Br by a molar ratio of 5:2 [113],[120].

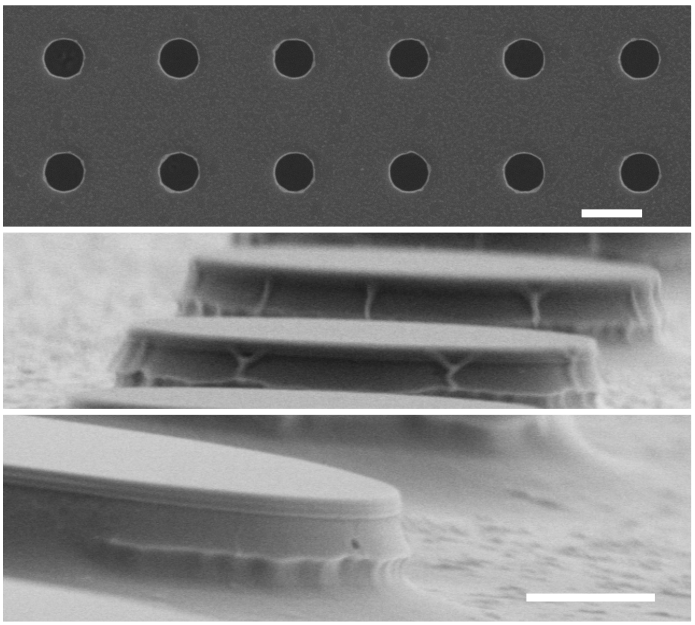

Figure 3.5 - Large disks produced by UV photolithography and etched with HBr:Br_2 solution for 25s. The top-down view illustrates much more circular final structures than the developed structures with SU8 coating in Figure 3.2 b.i. would have allowed. A side view shows that the reason for this is the SU8 resist is 'draped' over the final structure. Removing the resist shows that this has both protected the edges of the disk layer as well as providing a remarkably circular structure. Scale bar top 10 μm, scale bar bottom 1 μm.

The larger disks produced using UV photolithography exhibit an interesting and useful phenomenon: the roughness of the UV patterned disks discussed earlier does not introduce anomalies in the surface circularity of the disks during the etch process, which

would have impact performance. It was noted that the thinner resist was much more flexible, resulting in a "mean curvature flow" as it was under etched, which resulted in a circular and smooth resulting structure in contrast to the shape and irregularity of the defined mask (Figure 3.5). However, this effect seems limited to large disks with very thin SU8 (<100nm) and is not applicable to the μm sized patterns.

The wet etch has proven more than sufficient for both sub-μm and larger disks, producing high-quality smooth structures, with yields of around 80% when all factors are well controlled. The expected inhomogeneity of the etch rate over the sample surface (most likely due to wetting and reactant transport) contributes to a smooth and random distribution of sizes, which is desirable as small differences in resonator size allows for a full range of wavelengths provided by the gain region of the material.

3.3.2 Dry Etching

Reactive Ion Etching (RIE) combines the dry chemical and physical etch mechanisms by utilising a column of energetic reactive ions. This substantially reduces the redeposition rate exhibited by purely physical etch mechanisms by forming volatile products from reacting with the bombarded material. Much like in ion milling, the physical component of etching in RIE can become dominant, resulting in similar redeposition rates and overcut profiles. To correct for this, another chemically active component can be introduced, independent of the ion beam, that is comprised of inert argon ions. The consequence of this chemically assisted ion beam etch (CAIBE) is better control over the physical and chemical etch rates, resulting in steeper and deeper etches structures. However, the system becomes more sensitive to chemical etching parameters like temperature and reactant gas concentration and may yield rougher structures [104], [109].

However, as mentioned previously (Figure 3.3), very thin structures like those in the nanorod random network designs do not tolerate even a minimal under etching. For these types of structures, as well as polygons, dry etch processes have been explored. These include using a CAIBE for III-V structures as well as a purely physical high power Argon mill etch. As well as having the steep side-walls characteristic of an anisotropic trench etch, dry processes are often touted as a more precise and repeatable method for fabrication of nanostructures, particularly when coupled with the precision of the electron beam patterning. For the disk structures that make up the majority of this

project, this was not something we specifically sought to control. However, precision will be necessary for the fabrication of the network structures, and for situations where the disk diameter needs to be well controlled. The custom built CAIBE unit produced the steepest side walls with a suitable depth, in a short period of time, but instabilities in the chlorine delivery system resulted in unexpected contaminants, unpredictable coatings from re-deposited material and potentially also chlorine absorption, which can affect surface states and future etch processes [114].

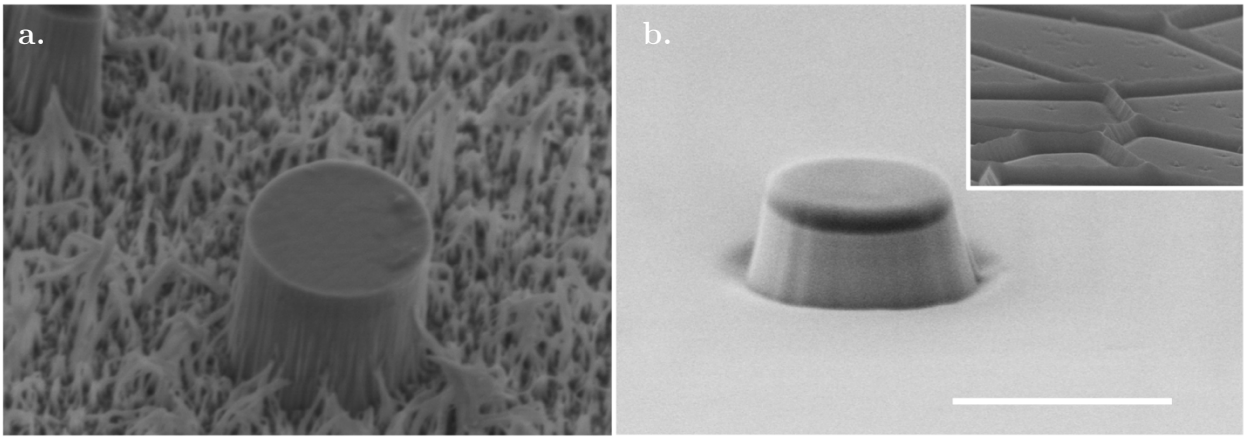

Figure 3.6 a. CAIBE etched structures. The chemical assisted process was not optimised, and the chlorine may have been contaminated with air, leading to increased 'grassification' and surface roughness. b. Argon only CAIBE etch, the final wafer output is much smoother, but the side walls are now angled, additionally the etch was much slower over a 20 min run. The argon milling has also resulted in a much smaller structure, 50% of its patterned size. Insert for network structures shows that narrower masks are completely removed, resulting in a triangular structure. Scale bar for all 1 μm.

The advantage of using a chemically assisted system is the reactant products of the chlorine – III-V interaction are highly volatile and can be easily removed, allowing for much deeper etches over shorter periods of time. In Figure 3.6 a, using 180 sccm Cl and 250 sccm Ar for 5 mins resulted in almost micron deep etches, with very steep side walls. However, the process was potentially contaminated with air, affecting the etch behaviour. Removing chlorine presented an issue, with just argon a much longer and high-power process would be required to remove top 180nm layers of the MQW. Heating the sample to 110°C can assist in volatility of reaction products, thus resulting in a surface that is both clean and relatively free of contaminants under these conditions. Argon milling, using 500 sccm at a low pressure, accelerated in a 1450V beam with 10% acceleration for 20 mins can etch beyond this 180nm layer and should etch down up to 300nm, however the thickness of the SU8-2000.5 resist is the limiting factor, as well as an etch slowdown in the AlGaAs containing layer of the wafer. As seen from Figure 3.6,

typically, the side walls are sloped at a steep angle compared with chlorine. The lateral etch 'shrinking' of the SU8 in long-duration Ar milling often results in unusable structures (Figure 3.6 b inset), that are thin and triangular. This has impeded the fabrication of the networks, as they require precisely connected nodes, which are not possible to make if the rod masks are too wide. Alternative resists, such as flowable oxide (FOx), may prove more appropriate for ion milling. An observed result in this project is the argon milling struggles to etch more than 200-300nm in any material tested here (resist, glass, and other materials like perovskite). However, even etches that achieved the required etch depth, have degraded the performance of the MQW wafer. A potential source for this effect could be due to re-deposition, as even etches that are deeper than the required 180nm often resist HF etch, and Argon and CAIBE etched structures often form a layer that resists under etching using HF.

The argon milling dry etch is otherwise almost suitable for the formation of disks and network structures and can provide suitable initial structures for testing and optimising of other etch processes. However, the process struggles to produce structures with good access to the sacrificial layer for following release steps, and often produces rough and steep profiles and has variable final sizes due to mask shrinking. Further research to optimise the fabrication of these regular structures will continue to explore alternatives such as the CAIBE and ICP processes.

3.4 Sacrificial Layer Release Etch

One of the principal advantages of the wet etch is that they can be highly selective for layer composition. This allows the etching of the AlGaAs sacrificial layer underneath the patterned structures and therefore release of the active layer from the substrate. The sacrificial layer material was chosen to be rapidly etched with HF, as As is highly reactive and the mechanism is quite well understood; the aluminium can be easily fluorinated[101], [108]. There are still some features of this etch to be aware of.

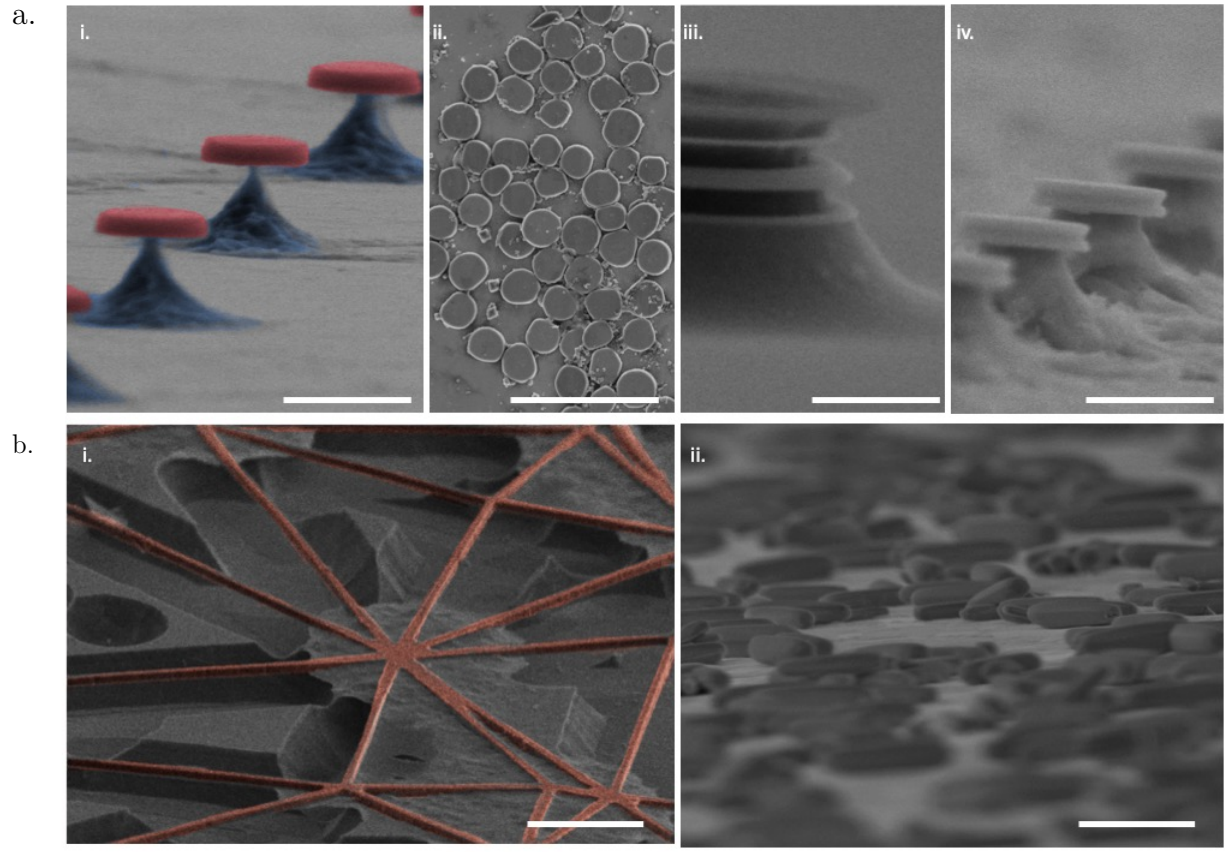

Figure 3.7 Results of HF etches a) i. A selection of under etched nanodisks on pillars (red) on AlGaAs pillars (blue) (scale 1 μm), ii. Some entirely under etched nanodisks, displaying some of the irregularities in shape that result from the wet etch (scale 5 μm). iii. Result of using buffered oxide etch (BOE), a 7:1 NH_4F:HF mixture, over 15 minutes, appears to now select for the Al containing layers of the disk rather than the sacrificial layer (scale 500 nm). iv. Apparent etching of the InGaP (non Al) containing layers after HF etch, a result of significant organic contamination of the DI water (scale 1 μm). b) Under etched network structure (the desired outcome of etch highlighted in red) The etch rate is proximity dependant on the structures, and the HF appears to have etched through the trenching features (scale 2 μm). ii. Commonly found nanorods after an HF etch, particularly for network structures. EDX composition analysis suggests AlF_3 (scale 2 μm).

As the AlGaAs sacrificial layer has a higher refractive index than the MQW layers, no optical mode is supported in the MQW without under etching. Because the WGM is a circumference effect, the sacrificial layer must be mostly removed. Partial etches to characterise the disks on pillars were initially used (Figure 3.7 a.i.), as having the disks lase in the region in which they were patterned allowed for SEM measurement and lasing of the same disk array. The results of this characterisation will be discussed in more detail in Chapter 4, but for the majority of the processes, the disks must be completely removed from the substrate (Figure 3.7 a.ii.).

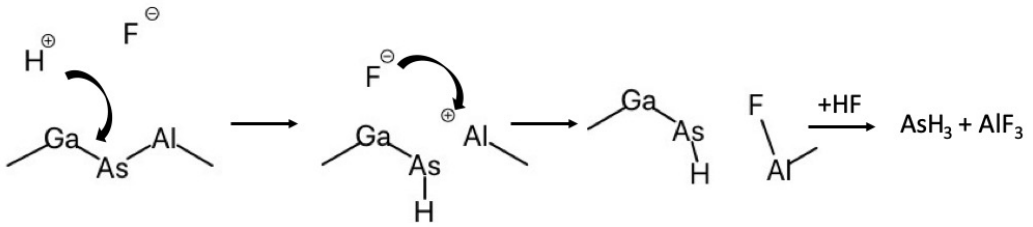

(3.2)

The chemistry of the HF AlGaAs system (Equation 3.2)[127] allows for a selective etch of the sacrificial layer without significantly damaging the valuable MQW layer by rapidly etching Arsenic and Aluminium but avoiding other MQW present elements. The etch needs to be fast to avoid damage to the MQW layers with high Al content, which are easily fluorinated over longer time scales. Fortunately for the integrity of these MQW layers, there is a substantial discrepancy from literature etch rates [100], [108], and the $Al_{0.7}Ga_{0.3}As$ layer etches much faster (40nm/s) in very dilute solutions (~1%). Attempts to slow down this etch with BOE for a disk on pillar structure result in a change of selectivity to MQW layers with lower Al content (Figure 3.7 a.iii.). The proposed mechanism is that As is highly reactive, and if sufficient AlF is in solution, it will react with the As surface, acting as an etch stop layer. It also appears that in the presence of organic contaminants, the InGaP layers can also significantly deteriorate, though the mechanism for that is unclear and beyond the scope of this research. It is apparent that AlF is not a generally soluble compound, and even slight impurities of carbon can result in the crystallisation of AlF_3 hydrate nanorods (Figure 3.7 b.ii.), which have been regularly observed and can be used to identify whether contaminants were present earlier in the process, particularly in the RIE cleaning or following SU8 cap ashing step [128].

The etch rates observed for the structures vary considerably, but tend to exhibit a 60nm/s rate for 2.5% HF, which results in very short etch times (~10s) to ensure minimal damage to the Al containing sacrificial layers, although complete under etching over time scales of 1 minute seems to preserve the performance of the disk. A possible explanation for the more rapid AlGaAs etch is that the AlGaAs is oxidised. The presence of oxygen is known to accelerate the rate of AlGaAs etching [127], which has been faster than the literature values, and reproducibly so. This compounds the effect that HF etches reduce in rate the longer the etch progresses, and in combination may explain the preservation of disk structure in the 1 minute HF etch. However, as introduced previously, oxidation of the surface after or during the monolayer cleaning step inhibits

the first step acid etching. This implies that oxygen also plays a dual role in producing etch stop layers of the active layers. The removal of the SU8 caps requires a 10 min, 200 sccm 20W oxygen RIE cleaning procedure before the HF step. This would seem to introduce a sufficient oxide layer to accelerate the HF etch rate, but it is also clear that this increases the stability of the active layer. Reducing the time of this oxygen plasma process, either by adding 10% SF_6 to accelerate the SU8 removal or by removing the SU8 with acetone and a cleanroom wipe, appears to be correlated with how stable the disks are after release into in an aqueous solution, as well as how sensitive the wafer is to the first etch step. It seems that excessive oxygenation restricts protonation of the wafer material.

The mechanism for this oxygen plasma etch termination is not entirely understood. Etch literature on similar materials indicates that oxygen based oxidisers like Hydrogen Peroxide (H_2O_2) are used to switch selectivity of reactants from Ga/InP to GaAs containing compounds [100]. As-O bonds are more readily protonated and can be converted into soluble AsF, whereas Ga-O bonds are very thermodynamically stable [129],[130], regarded as difficult to remove and are cleaned in strongly alkaline solutions [125]. This has been observed with silicon materials, where an oxygen passivation layer increases the longevity of biosensors in aqueous cell culture medium [124]. This is highly desirable for our system, as we want to be sure we removed this arsenic containing layer, but a subsequent oxygen terminated III-V layer could act as an etch stop/protection in the chemically diverse, generally slightly acidic to neutral cell solutions.
The protection layer will likely expire over long time scales. Cell environments tend to have low concentrations of HCl, which will likely degrade the AlO_3 compromising the disks after months in solution, in a similar mechanism to that seen in Si oxides. [123], [131].

For large structures, such as the currently produced network structures (Figure 3.7 b.i.) and the largest disks, under etching is eventually inhibited by insufficient material transport. Reaction products cannot diffuse quickly enough for the new reactants to replace them, which is further complicated by the interaction of HF reaction products. Diminishing returns for deep etches under larger disks were observed as the thickness of the proposed diffused oxide layer is likely surface level and does not penetrate so deeply. Additionally, fluoride reaction products are also reactive. Coupled with the highly reactive Arsenic, could potentially allow for a chemical re-deposition of Al and AsF etch stop layers over the column, inhibiting protonation of the As atoms, much like that seen

in when using buffered HF (Figure 3.6 a.iii.) [132]. Organic solvents have been utilised by others to induce the formation of crystalline AlF_3 nanorods like those seen on the material [128]. Deposition of organic contaminants on the column could possibly act in a similar way to nucleate the crystallisation of AlF on the surface of the columns, resulting in hollow shell structures, which have been observed in these larger disks.

However, because the oxidised AlGaAs etches extremely quickly (>60nm/s), it is also a difficult process to control. Once sub-μm disks were produced on thin columns, sufficient for lasing to be achieved, preliminary release into cell solution was obtained by concussive force to the wafer, which compromised the columns and released the disks into solution contained in a sample (Ibidi) dish. The yield for this was low, with only several hundred disks deposited over a large area, and even fewer in a suitable condition for lasing. This also results in large amounts of wafer substrate contaminants, which is not desirable as they contaminate future experiments and are toxic to cells.

3.4.1 HF of Dry Etch Structures

With the CAIBE etched structures, additional factors became apparent. Dry etch techniques have a well understood re-deposition effect. CAIBE should resolve this issue by ensuring that the reacted Cl volatiles are easy to remove, however, it is clear that 'sheaths' would form over the surfaces of the side walls, inhibiting HF etch. The development and removal of these structures are difficult to conclusively determine, as the system may have introduced air impurities into the chlorine gas inflow during testing. Similar issues are apparent in the Argon mill, where despite eliminating this contaminant source, much stronger HF etches (>5%) for longer time periods are required to perform the same etch that the structures etched with HBr require. This could be a result of a lack of need for the RIE oxide etch which the acid etch necessitates, bringing the etch of AlGaAs back in line with literature values. High temperatures can also assist the argon mill in removing the volatiles, which otherwise accumulate on the AlGaAs restricting HF attack and disturbing the laser structure. Difficulties appear to be related to how the etch rate struggles to deal with deeper etches due to the re-deposition process.

3.4.2 Release from Substrate

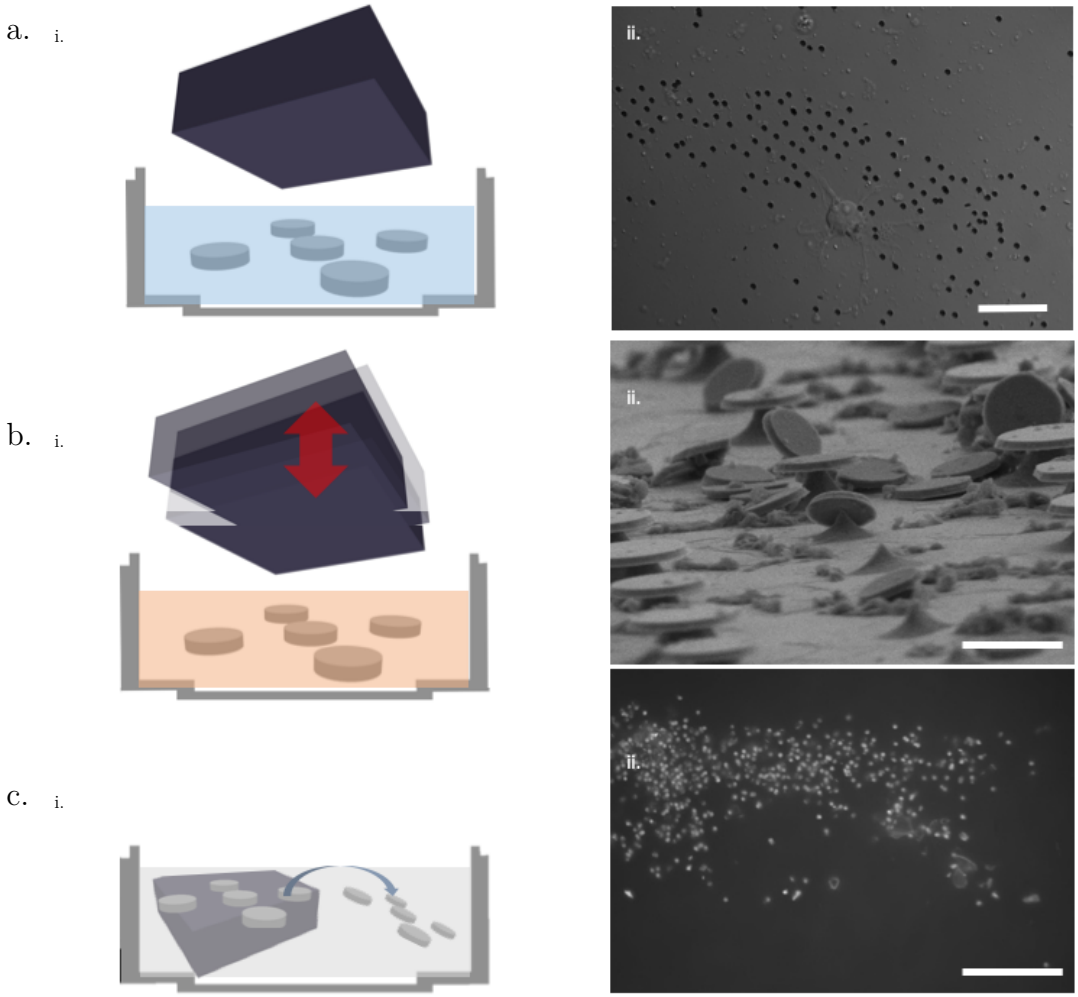

Figure 3.8 Schematic illustration of the different techniques explored for the release of disks into solution, with microscope images of resulting structures on the right. a) Complete HF underetch into future experiment receptacle. NaOH neutralisation was used to remove unreacted HF, scalebar 10 μm. b) Using concussive force to remove partially underetched disks, which removes the requirement of a clean starter experimental receptacle. Scale bar 1 μm c) Removing disks from a substrate via washing, scale bar 25 μm.

The principle and highest yield method to deposit disks into a biologically compatible samples dish is a combined complete under-etch of the sacrificial layer using 2.5% concentration HF and a washing process to detach the nanodisks from their support wafer and transfer them into a cell culture medium (Figure 3.8 a). Because HF is so reactive, it is relatively simple to add volume and concentration matched NaOH to consume remaining fluorine. NaF is highly soluble, so this can be removed with repeated DI water washes. With care, liquid substitution does not result in a loss of disks, and complete removal seems to impact neither future cell cultures nor disk performance,

which will be discussed later. The resulting solution should not be highly alkaline to avoid impact on the disks, which is vital for their long-term stability.

A primary observation of the resulting disks from this process is that the disks are 'sticky' and cannot float (Figure 3.8 a). This is likely due to an electrostatic attraction of the dielectric material of the disk. Occasionally, the disks are attracted upwards to the GaAs substrate instead of downward to the polymer tray. Once attached, the disks are very difficult to remove without further etch steps. This process does not happen with significant frequency, and is not clear what causes the effect from sample to sample; however certain charged polymer coatings (such as PDL) have been able to improve the yield, presumably by charging the disks and causing them to be repelled by their substrate (Figure 3.8 a.ii). There has been some success in using sonication to release the disks off the wafer surface. Combined with a more vulnerable pillar etched for long periods in 1% or less HF, large disk amounts have been successfully detached with significantly less wafer material, however, this still has resulted in significant rates of broken disks and non-lasing wafer material being deposited (Figure 3.8 b).
Occasionally the disks adhered to the wafer could be 'washed off' with ease. The distinction between disks that seemed stuck completely and those able to be washed off is still being explored, but methods such as by restricting access to the substrate with coatings and using solvents that appeared to etch air oxidised GaAs such as methanol allows the disks to be easily removed [125].
Furthermore, the disks can be permanently coated with materials to prevent this type of irreversible adhesion. Indeed, it is possible to functionalise these coatings, increasing the disks utility. Preparing the disks such that they are suspended in a biocompatible and transferable liquid, however, has been an ongoing challenge for this project, as the 'stickiness' of the disks causes them to be lost in transfer. Other partially successful methods of detaching those disks that are stuck on wafer or polymer involve using cleaning solvents like methanol, or abrasion / lift off methods.

Briefly explored was a direct method of under etching the GaAs substrate. Citric acid with a peroxide H_2O_2 oxidant can be used to selectively etch GaAs without impacting the InGaP MQW substantially. Citric acid is often used as a polishing etch for these structures to reduce the effect of the roughness introduced by dry etch processes. The proposed ratio is a commonly used (10:1). This had substantial success in removing adhered disks very quickly and did not seem to etch the MQW. This etch is also endothermic and needs to be kept warm to allow for the desired reaction to occur. This

etch was also explored as a method to remove the disks on a membrane structure (Figure 3.1 b.iv). However, despite initial results being promising, the etch rate was still too slow to allow for membrane lift-off and eventually damaged the disks as NaOH washes, optimised for HF neutralisation, did not seem to consume the complexant and oxidant as effectively for this mixture, eventually resulting in the loss of disk samples. This could be due to the H_2O_2 diffusing into the crystal structure of the disk, resulting in oxidation of the Al clad layers, changing the internal properties of the disk, or the reaction of Citric acid and NaOH may not be sufficiently rapid, where residual acid could have eventually damaged the MQW.

3.5 Encapsulation

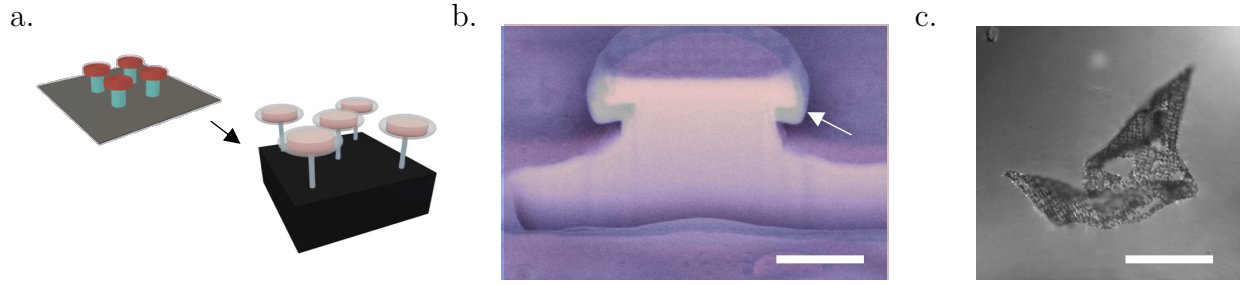

Figure 3.9 Encapsulation Schematic. An atomic layer deposition process of ZrO2 is used to coat all surfaces of the exposed disk with a uniform thickness, which can be tuned with more steps. b. scanning electron microscope of a focus ion beam (FIB) cross section of the disks with the unencapsulated disk light purple, and the overlay indicating a 100nm encapsulation darker colour (arrow). Scale Bar 1 μm c. membrane lift-off of the coating with embedded disks after HF exposure, scale bar 100 μm.

There are some situations where the native oxide passivation of the disks is not appropriate for their application, for instance where the disks need to last for several months in solution. In order to accomplish this the evanescent field must be contained within an optically inert shell, which we refer to as 'encapsulation' (Figure 3.9 a). There are multiple routes to accomplish this, but some of the most promising are Sol-Gel processing, and atomic layer deposition, which will be discussed briefly here.

Atomic layer deposition (ALD) works by using an evaporated oxide and binding agent. Here, Zirconia dioxide ZrO_2, a successful, biocompatible, encapsulant being tested on ERISM chips is explored (PhD Thesis: Andrew Meek [DOI not yet available]). For this we can use disks on pillars. These use a precursor gas to functionalise the surface, then a gas to react with this precursor coating to form an atomic layer. This process can be repeated for multiple steps to increase the thickness in a controlled manner.

This encapsulation is predicted to increase the stability of the disks further, allowing for experiments over several months, even for very thin coatings, we explored 10 and 20 nm thickness. To investigate if disks can be made non-sensitive to changes in external refractive index, we tried thicker layers 100nm thickness (Figure 3.9 b). Neither coating seemed to properly isolate the disks from refractive index sensing in this as IPA addition to aqueous solution was still detectable as a noticeable redshift. The predicted extension of the evanescent field, and therefore the maximum thickness required is around 300nm, which may take too long with this process.

The ZrO_2 membranes were relatively easy to lift off (Figure 3.9 c), allowing for large scale diffusion of HF through the structure leaving it mostly intact, though with substantial folding, something which could be controlled in future with a polymer scaffold.

The advantages of encapsulation warrant further investigation. Binding of antigen targeting molecules to III-V materials is not a well explored area, and although bio-coatings have shown preliminary progress, discussed in Chapter 5, much research has been done in functionalising silica. Since this mostly inert substance can be so versatile in all ways but in optical gain, a combination of the two approaches could lead to a very powerful tool to investigate biological functions.

3.6 Contributions

The optimisation and troubleshooting of the various fabrication stages, from selecting and optimising a non-selective wet etch to replacing the traditionally used dry etch, to developing a high yield release for biophotonic and transferable experiments, took a substantial amount of effort and literature review, and represent a substantial portion of this PhD project. The optimisation of the fabrication route for the disks; including patterning, acid mixture and HF release; and the dry etch process for the networks was done by myself. Optimisation of the patterning of the network structures was done by Soraya Ciaxeiro, a postdoc in Professor Gather's Lab) the preliminary tests and initial optimisation of the photomask for the SOI disks and the membrane lift-off was performed by Stefano Verme, a final year undergraduate project student whom I co-supervised, the Encapsulation with ZrO_2 and tests of the longevity and sensitivity as well as the FIB and EDX cross section was done by Lia Irvin, another project student whom I co-supervised, with the support of Changmin Keum (post-doc, Professor Gather's Lab).

Characterisation

In this Chapter, I will discuss the nature of the setups designed and utilised to characterise the lasing performance of the nanodisk devices discussed in Chapter 3. The principle points of investigation for this Chapter are spectral linewidth and threshold, and then investigate how such devices behave in the environment which they are designed to operate in. This will involve an exploration of their sensitivity to refractive index changes and sensitivity to input wavelength, stability over time, environmental refractive index, as well as potential influences of temperature and encapsulation.

4.1 Outline

In such a diverse collection of miniaturised light sources explored in the field of photonics, there are several processes that have the appearance of lasing whilst exhibiting other phenomena [26]. This originates partially from the increasing variety in the different gain and cavity designs. Indeed, in the citation, a commenter states a rule of thumb "no beam, no laser." As seen in Chapter 2, whispering gallery modes emitters exhibit many of the principles of the laser and their usual particular signature mode of operation [102], but they do not form a beam.

However, whispering gallery modes are sufficiently well demonstrated [133], [134] and have analytical solutions [46] in the literature that the question of whether they form lasing isn't generally brought into contest, it is nonetheless vitally important to characterise in order to ensure proper laser performance. This chapter describes the setups used, and how they were applied to characterise the lasing properties of the fabricated nanodisks.

4.2 Setups and Lasing

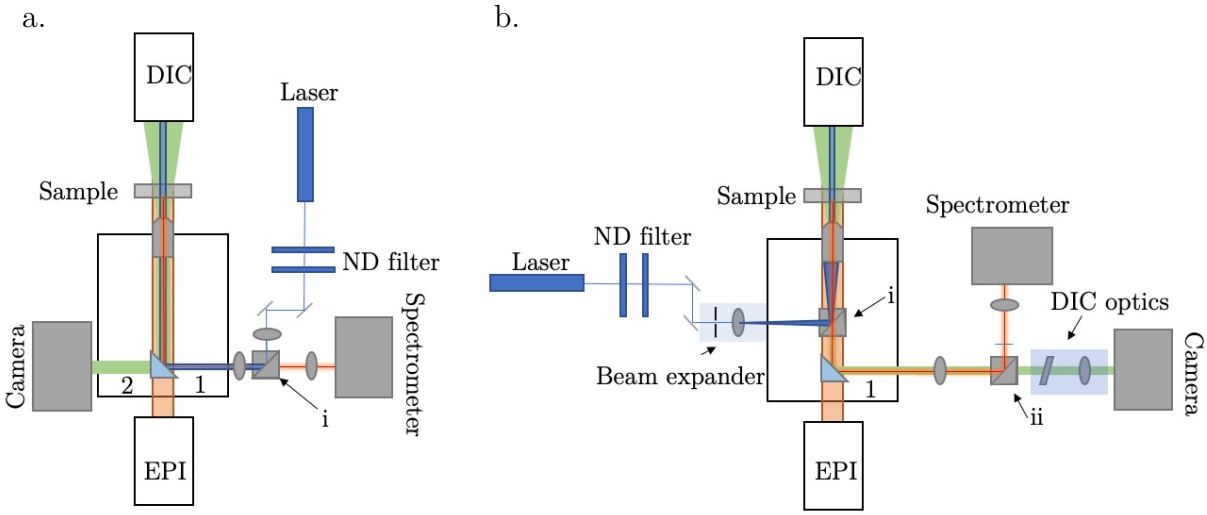

Figure 4.1 Utilised Inverted microscope setups. Equipped with epi-fluorescence (Orange), differential interference contrast (DIC) {Green}. Sample lasing collection path (Red). a) Input output paths controlled by internal mirror (light blue) to laser / spectrometer (split by dichroic 480LP {i}) {1}, and camera {2}. b) Couples the excitation laser with beam expanding optics just under the objective, splitting input / output with the dichroic mirror {i}. Output path for both camera and spectrometer {1}, split by dichroic mirror{ii}. Possible laser sources included the Alphalas frequency doubled diode-pumped solid state 473nm laser (a,b) as well as an optical parametric oscillator (OPO) source set to 20Hz and a picosecond pulse optical parametric amplifier, (OPA)* set to 1000Hz, with tuneable wavelengths (b).*

The nanolasers were tested initially on pillar configuration discussed in Chapter 3, where their positions could be fixed, and the sample more easily handled for investigation and could be transferred between solvents and imaging microscope setups (e.g. SEM). For lasing analysis, they were characterised on an inverted optical microscope (Nikon TE2000), described in a schematic Figure 4.1 a. The pump fluence was adjusted using neutral density (ND) filters (Chroma). The pump laser path was coupled into the microscope via a dichroic mirror {i} (Reflection cut-off 480 nm, long pass) and passed to the sample, initially using a 20x long working distance. The collected laser emission is then passed to a spectrometer (Andor Shamrock 303i), which was equipped with gratings: 600 lines per mm (lm) was often employed for scanning the devices, resolution of 150pm, but with good signal to noise and had sufficient bandpass (128 nm) for any nanolaser emission wavelength supported by the gain. When a higher resolution was required, 1800 lm grating could be used, with a resolution of 70pm and centred on the emission peak, allowing for more detailed peak fitting and characterisation. However, the 1800 lm had a narrower bandpass (28 nm) which resulted in adjustments to ensure all emission wavelengths were recorded. Additionally, was operating outside of recommended optimal configuration for these wavelengths which may have resulted in some chromatic aberrations. This provided preliminary data of lasing detection, but due to wide FOV and low NA of the 20x objective, it was challenging to identify and characterise individual disks. For optimum emission collection, the output required a precise focus onto the spectrometer slit. However, optimising for collection affected the path of the pump laser, moving it away from the disk, as the output and input paths are coupled (Figure 4.1 a).

To streamline the characterisation process, it was important to be able to independently adjust the collection and excitation path, so the setup was adapted (Figure 4.1 b), which also allowed for simultaneous imaging and spectroscopy. A 60x oil immersion or a 40x long working distance objective, depending on experimental setup, were used to identify and characterise the nanodisks, however now the adapted setup for Figure 4.1 b also allowed imaging fluorescence or DIC light transmitted by a dichroic mirror {ii} (Reflection cut-off 638 nm, short pass) via a cooled sCMOS Hamamatsu camera (ORCA-Flash4.0) to image the devices. The majority of the data was collected in this configuration. These adjustments also allowed for further optimisation of the spectrometer collection pathway, which reduced spectroscopic artefacts.

The pump sources utilised in this work are discussed briefly in Figure 4.1. The Alphalas laser, which has a 473 nm wavelength with a 1.5 ns pulse duration; and used the

telescopic focusing lens to adjust the diameter of pump spot on sample between 10-4 µm. This was exchanged for beam expanding optics for multiple disk excitation, as well as a more uniform pump energy density. The laser was operated at a 100Hz repetition rate, but some experiments required this be increased to 1000Hz for an increased time resolution. The optical parametric OPO (Opolette 355 LD) can provide a tuneable wavelength range of 210 – 2200nm (characterisation of the lasers utilised 450-650nm), with a maximum peak energy of 9.4mJ at 450nm, a 20Hz repetition rate and a 5-7ns pulse width. The OPA laser is also a tuneable light source, but has a 1kHz repetition rate as well as a picosecond pulse width, with a max power output 70µJ.

4.3 Fluorescence and Initial Lasing

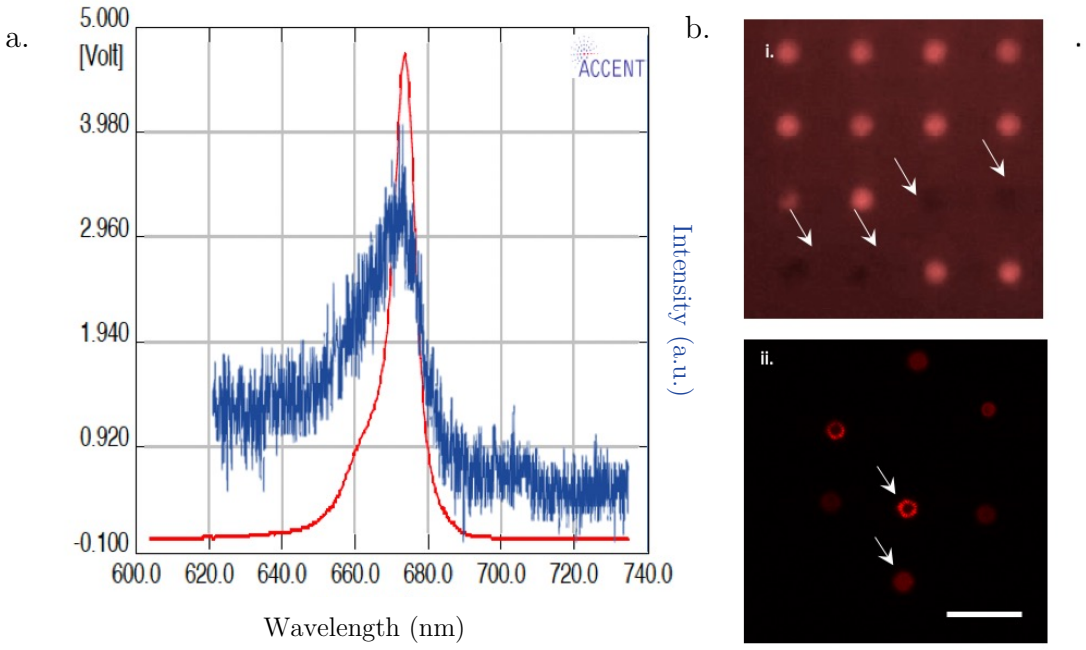

Figure 4.2 Disk material fluorescence investigation. a) Provided wafer fluorescence data from Sheffield (red) compared to fluorescence collected by laser excitation (blue) indicating the similar emission spectrum with the proposed setup (slight shifts likely indicate different calibrations of spectrographs). b) i. An array of columns with darkened structures after experiencing thermal damage. ii. a fluorescing disk vs a lasing disk (mode pattern evident) under uniform density pump beam. Scale bar 5µm.

This section outlines the basics of fluorescence characterisation. The first aspect to be investigated was the material from which the disks would be characterised. Datasheets were provided by the manufacturers (Sheffield and Tyndall) of the wafer material in each case but is also examinable by exciting large sections of the wafer under fluorescence excitation with the lasing setups. This gives an indication of the region of fluorescent

gain that the lasers would be excited in, the mechanics of which were discussed in Chapter 2.

As discussed in earlier chapters, the refractive indexes were derived from literature sources [72], [135], [136]. The structure of the wafer an obstacle for lasing characterisation as the sacrificial layer of AlGaAs had a significantly higher refractive index (3.79) than the calculated effective refractive index of the active layers, (3.6) and exhibited a similar fluorescence emission (Figure 4.2 b.i.). Numerical modelling predicted that this would cause an insufficient confinement of the light inside the disk to allow for lasing, as light would 'leak' into the sacrificial layer and be dispersed by the substrate. This was confirmed experimentally: pumping the columns produced bright fluorescence but no lasing. The fluorescence band of material emitted in a region of light between 640 and 690 nm (Figure 4.2 a), which was considered to be the region of sufficient gain to support a lasing mode. This bandwidth is also consistent with the strained InGaP MQW structure discussed in Chapter 2.

Pump pulse energies that exceeded ~25 mJ/mm^2 per pulse appeared to produce irreversible changes to the fluorescence profile, for columns in Figure 4.2 b.i. No lasing was recorded from this sample, as was predicted from numerical modelling. This could be used as an estimate the maximum thermal tolerance for future experiments investigating the lasing properties to prevent damage to the sample. Once the disks were underetched sufficiently for light confinement, the fluorescence profile of a lasing disk, which exhibited characteristic mode patterns, could be compared and contrasted to a regular non-lasing fluorescence (Figure 4.2 b.ii.).

4.4 Lasing Properties

This section will discuss the main results of the lasing characterisation, beginning with an overview of the observed lasing phenomena whilst the disks were on wafer, then follows an analysis of the detached disks and a discussion of emitted wavelength, threshold and linewidth and their possible origins, for instance the significance of fabrication outcome on the resulting quality factor.

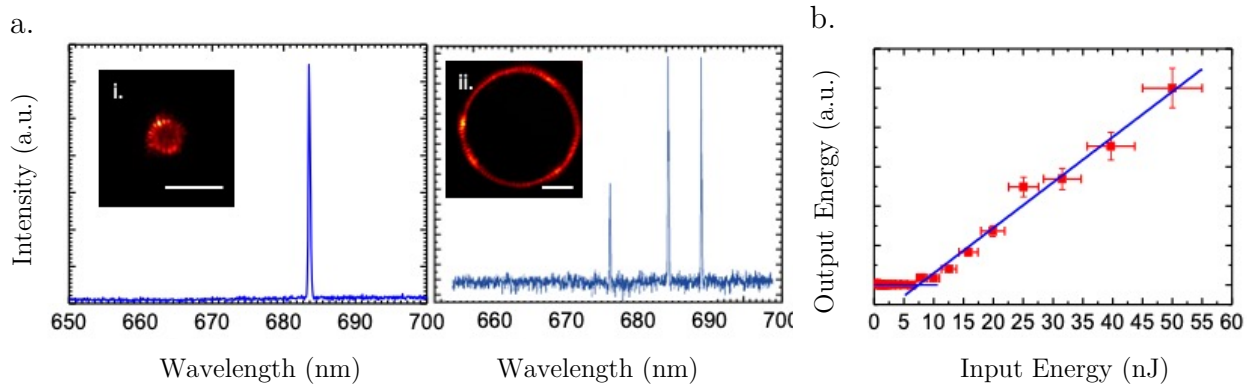

Figure 4.3 Example spectra from a) i. sub-μm disk showing single mode emission ii. 5 μm disk with multi-mode emission, scale bar 1μm. (inset: microscopy pictures with laser fluorescence visible.) b) Typical lasing threshold test for disks on pillars.

4.4.1 Emission Behaviour

The fabricated devices from this wafer were investigated and compared to similar devices in the literature [37], [66]–[68], [117] to confirm the properties of the wafer and compatibility with the proposed fabrication process, which potentially could cause compromise the disk MQW. The results indicated that the disks narrow linewidths (~0.1-0.25 nm) which indicated comparably high Q-factor for equivalent devices, as well as very low thresholds, which suggested the fabrication process yielded high quality devices. Additionally, performance needed to be confirmed at warmer than room temperature and in an aqueous environment, a potential pitfall for microcavities which operate more optimally when cooled [73], [137] or with already low Q factors. Using sufficiently underetched disks-on-pillars, the lasers could then be characterised [101], [109]. Initially, the sample was simply checked to lase, so the disk arrays were pumped with the diode laser at a comparable power to the microsphere resonators (~500 μJ/mm^2) [13]. These preliminary investigations, shown in Figure 4.3 a, indicated that the disks exhibited characteristics of laser spectra: emission wavelengths that are highly monochromatic, narrow linewidths and high intensity compared to fluorescence, with smaller disks supporting only one mode in the gain region, and the larger disks supporting multiple. The resulting peaks had linewidths much narrower than 1 nm, with values of down to less than 100pm recorded – approaching the resolution of the spectrometer. The initial disks were large (~3 μm in diameter) and had very angled side walls, so were not ideal for further investigations. However, since the side walls were smooth, which impacts the resulting Q-factor more than verticality [60], [138], it was still possible to make some preliminary investigations [72]. The disks were large, and as expected they emitted

multiple peaks (Figure 4.2 a.ii), however it could not be confirmed as to whether this was multiple T_E modes due to the large diameter, or T_M which were not expected [106]. Furthermore, the spacing of the disks was also not sufficiently large to rule out that multiple disks were being excited. This initial data was collected in the configuration in Figure 4.1 a. The emission from the nanolaser was collected through the same objective, filtered from the pump light and passed to a digital camera and a spectrometer (spectral resolution, $\approx$ 0.15 nm FWHM). Initially the excitation spot size could be adjusted by changing the telescopic lens position. This could shrink the spot down to below the spacing between the disks allowing for individual excitation and examination. However, as discussed, this configuration resulted in a compromised focal position on the spectrometer CCD.

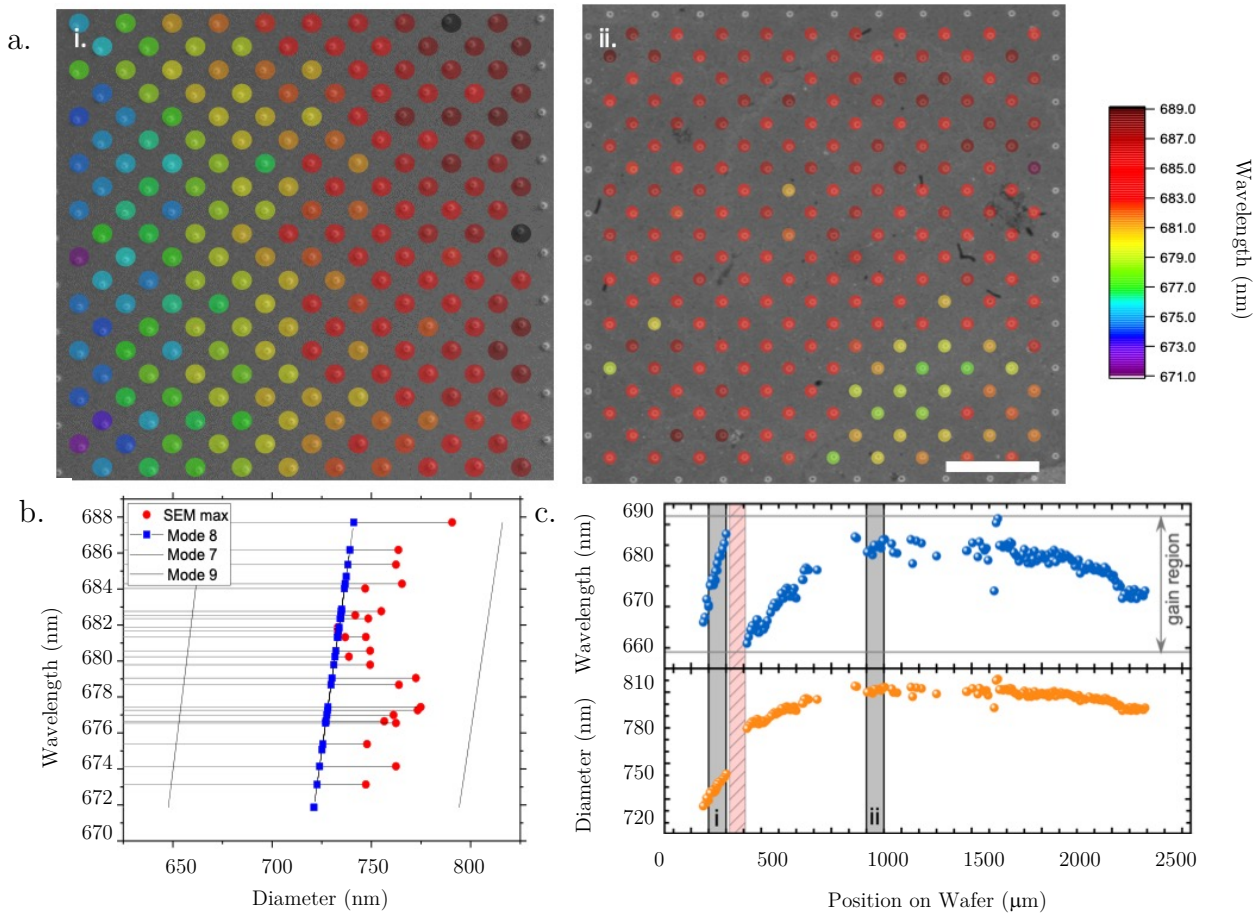

Figure 4.4 a) SEM maps of 10 by 10 area disks. Markers indicate collected wavelength from each disk, note the difference between the gradient area (i) and the uniform area (ii). b) Diameters calculated from thresholded SEM images plotted against collected wavelength (red) and the theory predicted mode (line). (blue) determined diameters for each disk wavelength based on proximity to mode. c) Wavelength spread over a whole wafer, marked regions i and ii correspond to those in a).

In this configuration, a wafer with a set of disks on pillars that were nominally identical were resolvable, however the sub-μm disks had significant optical diffractive artefacts that limited size calculation from acquired images. Two areas were selected (Figure 4.4 a) and marked such wavelength and position data could be compared with SEM images of the same region to measure diameters more accurately. A gaussian peak fit was applied to the data from the spectrometer. Additionally, wavelength information along with a cross section of the wafer was acquired. These scans were automated using a Prior stage control script to correlate x-y position information to wavelength, which allowed the generation of the wavelength maps in Figure 4.4 a. From these maps, it is possible to ensure that statistically the disks were behaving similarly. To determine if this was the case across the whole wafer, a total cross section of the wafer was analysed to determine the uniformity of the etch. The SEM images clearly showed that the vast majority of disks produced on the wafer were sub-micron so were predicted to only be able to support a single mode. By increasing the x-y resolution by using 10 μm/s step sizes during raster scanning, the disks could be excited and sampled with 0.1s integration times such that any peak doublets could be matched to the nearest appropriate disk and exclude the possibility of anomalously large disks. Figure 4.4 b shows maximum sizes calculated by thresholded image analysis from SEM images vs the predicted mode pattern from Chapter 2 of the nanodisk lasers. This was investigated across the wafer to examine the behaviour and consistency of the etch process, as discussed in Chapter 3. A 'gradient' region was used to determine the spread of wavelengths producible from a range of diameters, such that this could be reproduced (Figure 4.4 c.i.) A more uniform region was used to check the homogeneity of the wet etch (Figure 4.4 c.ii.). These results confirmed models from Chapter 2 that if there is an introduced gradual increase in disk size (over ~20 nm), there was a corresponding increase in the wavelength emitted (~ 16nm), up to a dark region where lasing did not appear to be supported (which was predicted in Chapter 2, for areas where the free spectral range was too wide for any mode to be in the gain region). Further increase in size the next mode was supported (Figure 4.4 c). Because wet etches have an intrinsic uncertainty due to the variety of factors discussed in Chapter 3, even homogeneous regions have a significant spread of wavelengths (~10nm). Further control was not an aim of the work, as a spread of wavelengths are desirable for unique identification. Provided the disks could be fabricated within a narrow range and ideally a single mode, the diameter could be trivially calculated. Additionally, this evades the issue that there are small differences between the radiative Q factors for different mode numbers, as predicted in Chapter 2 which would result in different properties. As discussed in Chapter 3, if further specificity

over the size and homogeneity was required, a dry etch would have to be utilised. This could produce a specific size in a specific position, from which more predictable wavelength information could be used to fully optimise the optical modelling of Chapter 2.

From the data shown in Figure 4.4 c it was possible to experimentally determine the range of wavelengths supported by the gain medium with the distribution being focused between 650 and 700nm. These data were then used to refine the models in Chapter 2. The data for measured diameter using the SEM images had a significant (100 nm) uncertainty when the diameter of the disks was calculated from the SEM images with FIJI, which tended to overestimate the sizes due to an exposure gradient across the image. However, free spectral range is so large that this uncertainty can still be used to determine which mode is supported, even by using the geometric solution to the optical path equation $\lambda = \frac{\pi d n}{m}$ [99], [101] (where the diameter is d, the effective refractive index is n, and the mode number m). It was determined that should a larger resonator with two or more peaks be present, the free spectral range should lie within the bandpass of the spectrometer, provided a 600 lm grating was used. Thus, the diameter of the disk was determined first by fabricating a narrow range of diameters, then measurements from initial SEM images which could also confirm the homogeneity, finally the more precise size information offered by the lasing wavelength, mode number and optical models could be used instead (Figure 4.4 b).

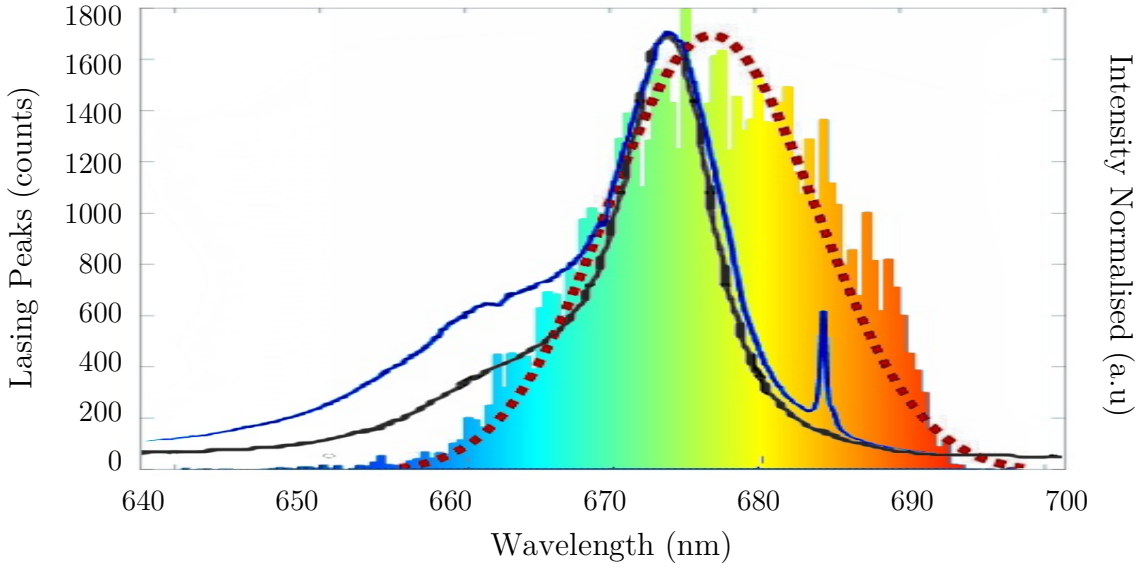

Figure 4.5 A histogram of collected lasing wavelengths across 10 samples (rainbow) with fit (red dashed line). Manufacturer fluorescence peak (black) and fluorescence from CW excitation (blue) plotted for comparison.

Once disks were detached, and higher NA objectives and setup in Figure 4.1 b was used lasing spectra showed a high signal to noise ratio even when single pulse excitations were used which allowed for more rapid scanning of large areas (400 μm/s, with peaks up to 300 counts above background at 600 Hz). Limits to the scan speed and disk tracking software were limited by inaccuracies in the reported position of the stage and the true position that could be determined from reference images. This could be exacerbated due to potential movement of the sample, causing there to be substantial discrepancies in the resulting spectra map and image acquired. Keeping these factors under control, ensuring that the stage was calibrated for each scan, and using the beam expanding optics, allowed for systematic scanning. Across several samples, it was possible to construct a histogram of the disk wavelengths, which are plotted Figure 4.5. Compared to the spontaneous emission spectrum provided by the manufacturer and when a disk is excited with continuous wave lasing, the distribution of wavelengths emitted disks seems redshifted. This could indicate that the blue-shifted wavelengths supported by the gain have higher absorptive losses, resulting in a lower Q_{abs} factor. However, this could also be an effect of band bending, briefly introduced in 2.2.5, which may have shifted the resonance and slightly reduced the bandgap, which has been noted as an effect of native oxide formation on other semiconductors [42].

As expected, the FWHM of the disks exceeds the spectral resolution of the instruments used, suggesting Q factors of ~10^4 as initially expected and predicted by simulations in Chapter 2, indicating very low scattering and absorptive losses. It was also confirmed that the devices continued to work at a high efficiency in liquids: de-ionised water, IPA, phosphate buffered saline (PBS) and cell culture medium were all tested.

Larger disks were also investigated, where it also confirmed that the disks exhibited either two or more modes for larger diameters. It was confirmed that these modes were not T_M modes, like the pairs of modes expressed by the polymer microspheres, as these modes are not well confined within the disk and experience lower Q-factors, and thus the T_E dominates [67]. To further confirm the presence of the single T_E mode emitted by disks, their polarisation was analysed. For this, disks that had been detached and resting perpendicular to the pump beam were analysed. A polariser was rotated whilst exciting the disks to determine whether the light output was polarised. The mode is indeed at least partially polarised (~a dip of up to 1/3 compared to non-polarised intensity) as well as showing identical behaviour for all peaks for multi-mode emission. This confirmed the lack of T_M modes which should have an opposite polarisation. The lack of complete polarisation is likely due in part to the scattering nature of the medium the disks are in as well as the high NA of the objective used, and also – probably more

significantly, irregularities on the surface of the disk as an artefact of the fabrication process, which could be used to assess fabrication quality in future [139].

4.4.2 Spectra Linewidth and Disk Quality

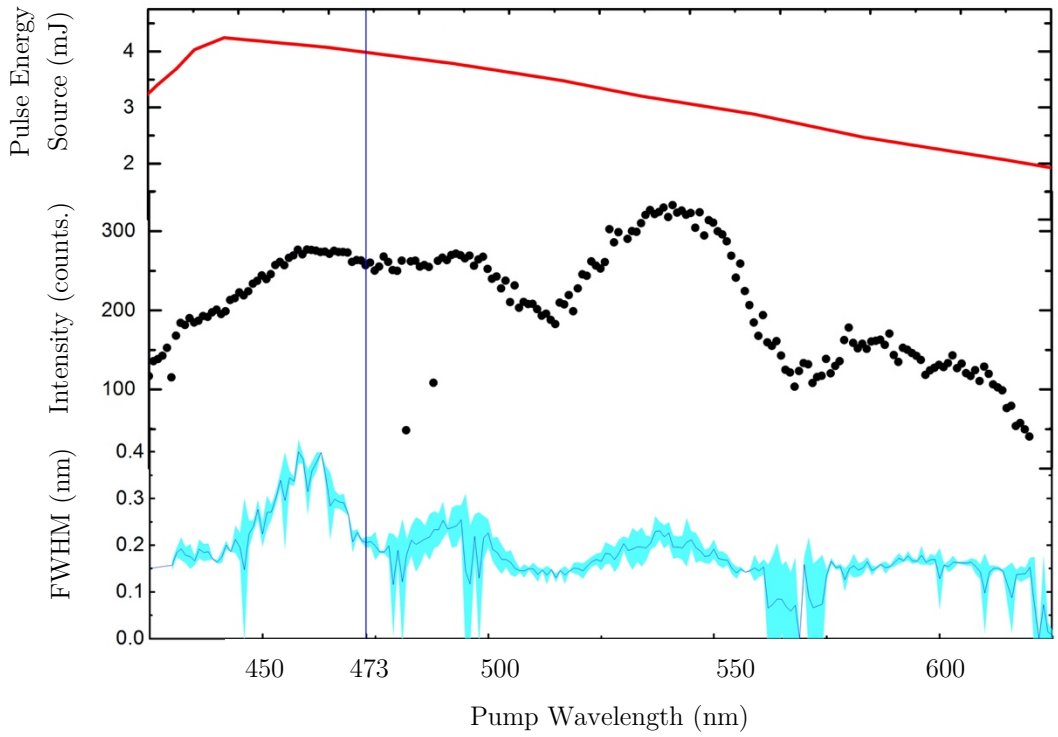

Figure 4.6 Relationship of Excitation wavelength and power (red) with respect to average intensity (black) and FWHM (blue) for 5 nominally identical disks. Annotated line at 473nm to reference the predominantly used Alphas laser wavelength. Note the peak in intensity at 542nm, despite lower input power. The blue line represents an average FWHM, with the range of values indicated by a min / max curve.

The spectral linewidth of the resonators needs to be extremely narrow for barcoding and sensing so that multiplexing can distinguish closely spaced wavelengths. The nanolasers produced by this project generally produce very narrow linewidths around 0.2 nm at emission wavelengths around 680nm, a factor that is closely correlated to the Q factor of the resonator, which can be described as the peak wavelength over the peak linewidth. The FWHM have been measured for a variety of nanolasers in agreement with this estimation, the results of 5 such disks can be seen in Figure 4.6. However smaller linewidths (0.1nm) were observed for the larger (>1μm) disks, with a high fabrication quality entailing smooth vertical surfaces, whereas larger linewidths being exhibited by the smallest disks produced (650nm) or those with irregular shapes. This is an expected result of a lower quality factor as predicted in Chapter 2 [66], [74]. Additionally, the linewidth varied substantially over increasing input pulse energy, with the narrowest

peaks appearing just beyond the threshold transition into spontaneous emission, with later broadening likely a thermal or carrier effect. Even considering this, the linewidth of a single disk also varied with pump excitation wavelength using the OPO (Figure 4.6). From the figure, we can see that higher peak widths do correlate with higher intensities, but not significantly so. For wavelengths <480nm, the broadening could originate from refractive index changes induced by charge carriers, with the higher energy pulses resulting in more non-radiative decay processes [87], or could result from the charge imbalances could enhance band bending due to excited surface states [43]. Finally, others have observed Sagnac effect rotational symmetry breaking resulting in degeneracy lifting of the clockwise and counter clockwise propagating modes, with whilst difficult to resolve with spectrometer resolution, might manifest as broadening [48].

4.4.3 Threshold measurements

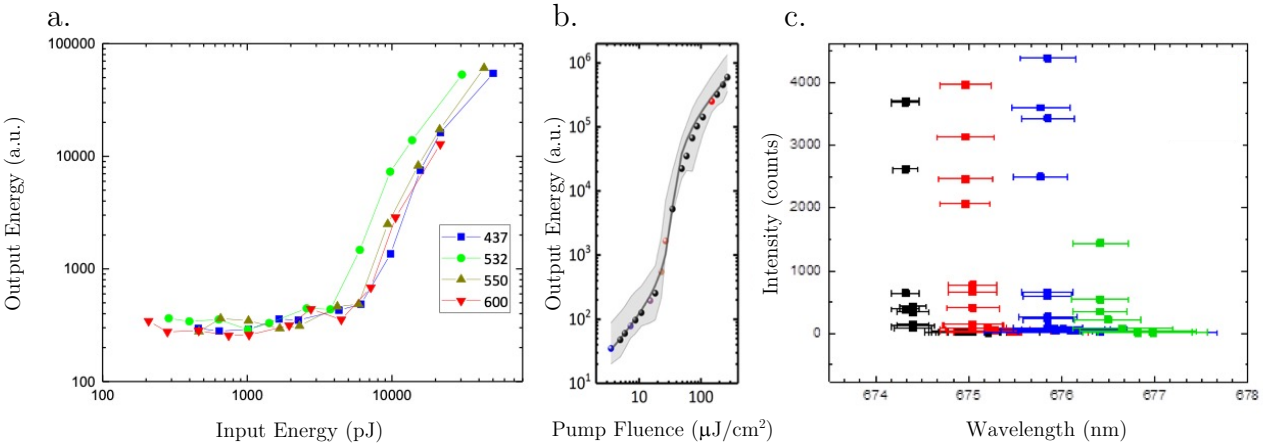

Figure 4.7 a) Threshold similarity with wavelength change over a batch of disks. The spot size is similar to that used in early tests. b) statistical threshold test from one batch of disks, statistics on disks over several batches, with a measured spot size diameter used to calculate the pump fluence. c) Peak intensity and wavelength variation of 4 disks, increase due to increasing pump energy, FWHM depicted as error bars.

One of the most defining features of a laser is the threshold, defined as the point when the linear output of spontaneous emission transitions to the nonlinear process of stimulated emission [26]. The threshold contains a substantial amount of information which can also be used to extract certain properties of the laser emitters. As explored in Chapter 2, these MQW structures are expected to have extremely high gain efficiency, and as a result we expect a correspondingly low threshold [140]–[142]. For optically pumped lasers, the threshold can be determined from a plot of the log of the in the pump energy density vs the log of the integrated peak area [26]. The setup to acquire this data,

described in detail in Figure 4.1 b: used the 60x, high NA objective, as thresholds were done on detached, well separated disks to ensure minimal interaction or mode leakage and to eliminate the substrate and other sources of fluorescence. Small disks did not contain much fluorescent material, so the high NA objective and long integration times (10 s) were vital for subthreshold increase calculation (Figure 4.7 b). Detached disks were preferred also as to remove any doubt that the pillars were reducing light confinement. To supply sufficient disks for statistical analysis necessitated the development of detachment procedure developed in Chapter 3.

Initial threshold data acquisition (Figure 4.2) had a number of issues: the disks may have still leaked some photons through the column, and the 20x objective used in Figure 4.1 a had been unable collect sufficient light to detect a threshold. The 2.2 μm disk examined in the initial threshold observation required a pump fluence of 380 pJ, which is much higher than the measurements shown in Figure 4.7. Using the initial setup of a 20x objective or 40x long working distance objectives, sub threshold fluorescence was not detectable for a light in- light out curve, due to the aforementioned small footprint and therefore fluorescent material of the disks. Additionally, the spot size was large enough to excite nearby disks, such that the total energy flux on a single disk was certainly much lower than the total pump power measured.

Using the adapted setup, the disks were compared for excitation wavelength using the OPO, in order to determine whether this had an effect on lasing threshold, which confirmed the disks appear to exhibit lower thresholds around 532 nm (Figure 4.7 a), complimenting the higher intensities detected in Figure 4.6. For the majority of the threshold analysis the Alphalas laser was used. The data was plotted on a log – log light in light out plot show the change from linear to super-linear lasing transition. The devices were then lased using up ramp and down-ramp of the neutral density filters to check that no degradation had occurred and to confirm symmetric behaviour, which was a concern for the shorter wavelength pulses. Disks that have sustained minor thermal damage would exhibit higher thresholds as well as a reduced total output intensity, and thermal strain on the disk would result in unpredictable and irreversible behaviour. Higher thresholds were also experienced by those disks that had non-ideal etch patterns such as slopes or irregular shapes. The threshold could then be used to confirm that the disks were of sufficient quality before experiments were initiated, such as the statistical distribution in Figure 4.7b, which is the light-in light-out curve of 10 disks from a single sample. This illustrates the similar thresholds for disks across a sample, where the grey boundary is the minimum and maximum values for the disks in the test sample. These disks were checked in solution to see what the threshold would be in a static but similar

environment to future experiments, such as the cell experiments discussed in Chapter 5. Comparing from the initial threshold estimations, the thresholds for the detached disks in solution measured over an order of magnitude improvement (~10pJ threshold/pulse, corresponding to ~0.1pJ incident flux on the disk). The 60x oil immersion objective was used to detect the linear increase in light out below threshold, which still required long integration times of 10s – equivalent to 1000 pulses. Though an increase in fluorescence was observed in this configuration but a sub threshold peak was not detectable, so peak narrowing was not observable, hence FWHM threshold line narrowing was not detectable. As a result, the thresholds were calculated as before by identifying the final peak position as before at the highest energy per pulse and integrating over the peak position for this and also integrating the same region below threshold. Each following point was measured with the same integration times until just before the detector saturated (or for down-ramp of threshold, when the signal to noise would obfuscate the measurement), the acquisition would be repeated at a different order of magnitude of time (10s repeated at 1s). The size of the spot, important to determine the fluence incident on the disk, was approximated using a combination of techniques, including images of the spot on fluorescent film such as spin-coated ITDT on glass, to measuring the size of hole that a single high intensity pulse burned into the film, to observations of how much the beam could deviate from the disk and still induce lasing output. For the 60x oil immersion objective operating at the smallest possible spot size, the excitation pulse was estimated to be around 5 μm diameters of approximately uniform excitation. This allowed a calculation of the photon flux incident on the disk, which was used to calculate an energy per area dose of 13μJ/cm^2 (Figure 4.7 b).

To further this investigation, threshold curves were acquired on the same disk at different excitation wavelengths were repeated using both the OPO and OPA sources. This was in response to the narrower linewidths observed for wavelengths in the green (540nm) and red (600nm) which may indicate better performance for the nanolasers. The power curve of the OPO for wavelength dependant sources in Figure 4.7 a was repeated using the OPA with the same disk samples showed a further order of magnitude reduction of thresholds, however, excitation at any wavelength showed significant peak broadening and distortion likely due to excessive carrier mediated 'chirp' effects due to the ultrafast pulses, rather than the high energies observed for the OPO [89], [143].

Once the data was collected, it was then be fit to an analytical model described by the equation from Chapter 2.4:

$$I_{out} = \frac{k}{2\gamma}\left(I_{in} - \frac{\gamma}{\beta} + \sqrt{\left(\left(I_{in} - \frac{\gamma}{\beta}\right)^2 + 4\,\gamma\, I_{in}\right)}\right)$$

Which describes the steady state solution for lasing derived from the rate equations. The spontaneous emission factor, or β factor, is a ratio that describes how efficiently the photons in the resonator are converted into laser photons [91]. As this factor is strongly related to the dynamics of a laser cavity, from this a number of output characteristics can be estimated. The beta factor fit of 3% gives a measure of the efficiency of the system, where a 100% conversion would indicate a 'thresholdless' laser. The beta factor can also be thought of as a product of the resonator Q factor and the inverse of the mode volume and can hence be estimated to be close to the measured value. The values of k, an intensity correction constant and γ, the photon lifetime was determined by iterative processing to approach best fit values. Typical lifetimes of microdisk lasers are in hundreds of picoseconds [4], which is consistent with the nanosecond pulse length suitability of the OPO and diode laser. The long lifetimes and high beta factor indicate a strong light-matter interaction leading from the Purcell effect.

Future investigations on the lasing of the nanodisks will focus on the red excitation wavelength, which required similar, very low pulse power to the conventionally Alphalas laser. This was due to a combination of the lower linewidths, as well as lowest energy in excitation pulse. Also avoiding short wavelength excitation sources is desirable in long term biological experiments and other areas, for both potential decreases in cytotoxicity for biological samples specifically as well as increased scattering and interaction of shorter wavelength light more generally. Promisingly, the very low pump thresholds in Figure 4.7 b and some fluorescence observation using 1064 nm trapping beam lasers used for optical tweezers, two photon excitations would be possible.

4.4.4 Threshold Behaviour

The change in wavelength as a function of peak intensity was expected for the near threshold effects, though initially surprisingly this was a blueshift, instead of the expected temperature related redshift (Figure 4.6 c). However, this is a commonly

observed effect in the literature. Initially, particularly in the superliner region, the disk is redshifted compared to the lasing from the linear high-power region until the carrier inversion reduces the n_{eff}. [144], [145]. To ensure this did not distort results, when used in experiments the disks were operated at a power of 100 $\mu J/mm^2$, which was significantly above this near threshold distortion but also did not result in deterioration of performance.

4.5 Wavelength Sensitivity and Stability

Because the proposed WGM nanodisks are highly sensitive structures, as just discussed, there is an anticipated issue of how reliable the wavelength would be in a complex environment like that of the cell [146]. The different avenues for sensitivity are discussed at length in Chapter 2, but experimentally several unexpected origins of environment changes had to be kept under control. The disks were first tested in already used CO_2 dependent cell culture medium, which used a chemical reaction with CO_2 gas input to mediate pH, in a similar manner to that found in-vivo. Typically, the balancing of the gas and solution is not necessary to control to high degrees of precision, however the disks are more sensitive to environmental changes than cells in this instance. Both Sensitivity and Stability refer to a change in wavelength, but in regard to terminology, sensitivity is defined as a reversable shift in wavelength and stability refers to an irreversible change in wavelength or no longer lasing.

4.5.1 Stability in Solution

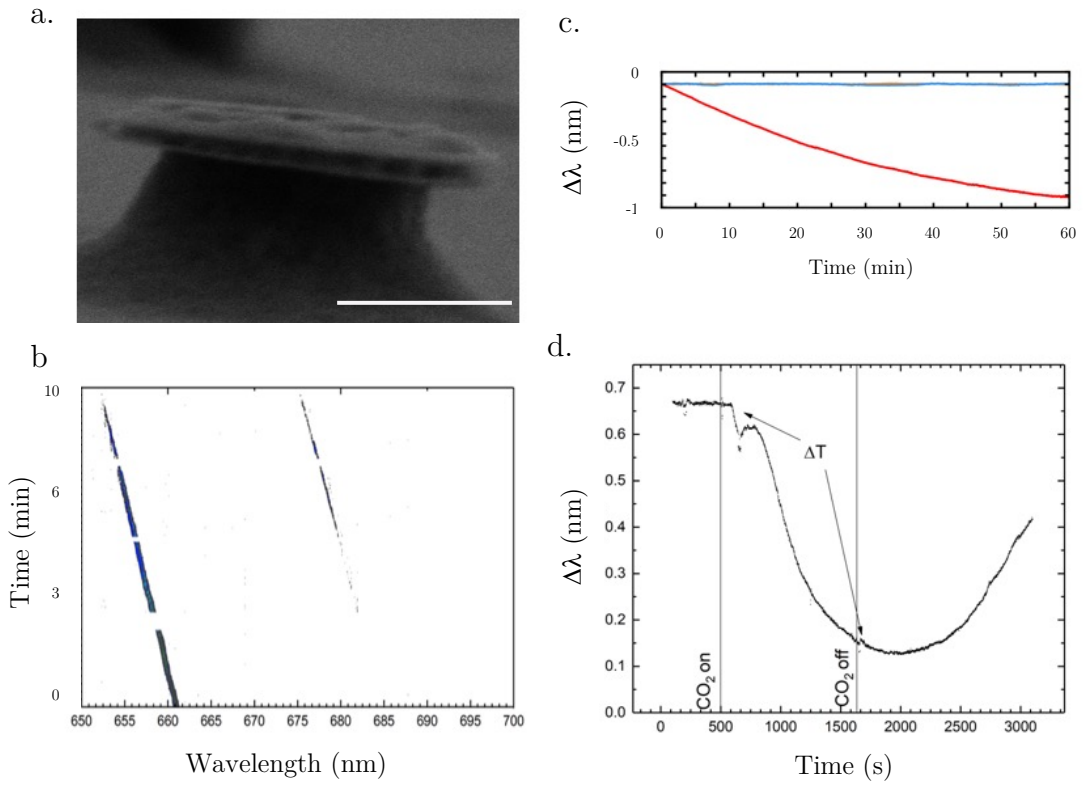

Figure 4.8 a) SEM image of a disk after 3 months in DI water, showing extensive degradation. Scale bar 500 nm. b) Disk wavelength variation in a low pH solution (~2 measured with litmus paper), indicating the shift due to reducing size. c). Stability of lasing over continuous excitation with native oxide passivated disks (blue) and non-passivated disks (red). d) solution of calcite accumulation and reduction in inappropriately balanced CO_2 environments. ΔT indicates a possible temperature fluctuation as the gas flow was started.

To attempt to decouple the effects of sensitivity and stability, it is most important to first to check the material integrity under solution with regular lasing investigation, where disk degradation could be observed by comparing SEM images. After 3 months of continuous immersion, many disks had stopped lasing, due to a degradation of the material in solution (Figure 4.8 a). This was sufficiently beyond the expected duration of a cell experiment, and therefore aims of the project, but encouraged some development of the previously discussed encapsulation route to prevent this. Detaching the disks into solution initially resulted in trace acidic components from the detachment process, as CaCl was used to ensure that HF was not present, this resulted in trace quantities of HCl. Though not anticipated to be of concern, the disks gradually etched (100nm in 10 minutes) in this solution, Figure 4.7 b shows such a shift of wavelength as a result of disk etching. The disk was sufficiently large (1.2μm, calculated from the FSR of the two modes) that, as the wavelength reduced, a second mode became visible. Once the disks

could be detached in neutral solutions, the disks were scanned in statistically significant numbers with the automated stage scanning that was used on the wafer sample investigated in Figure 4.2. This process relied on reference landmarks, so were typically unsuitable for dynamic conditions as the accurate positioning of the stage could not be ensured, and significant stage drift couldn't be corrected for. These interrupted scans were used to check that the material would not deteriorate rapidly to allow for long term, in solution experiments.

However, instances where there was a significant blueshift in the wavelength when the disks were characterised in cell medium (Figure 4.8 c). After controlling known variables, it was difficult to confirm whether this was an etching effect as previously discussed, as the intensity remained unchanged during this blueshift, though it remains a possibility this was a photochemical oxidation process [147]. The observed blueshift is also non-linear, in contrast to the etching effect. It can also be confirmed by an observed blueshift under continuous excitation that it does not continue when the disk is not pumped. To correct for this effect, the prolonged RIE oxide passivation process discussed in Chapter 3, was intentionally introduced before the HF detachment process. This completely removed the blue shifting trend for the majority of samples; however, a minority of samples still experienced a reduced effect and likely was a result of fabrication issues. In an ideal situation of stable disks, long term scans in the environmentally controlled medium taken under continuous excitation show no substantial shift. A variety of environmental factors needed to be controlled for long acquisitions, so typically a single disk could be continuously pumped for an hour before irregularities in climate control interrupted the experiment. This issue has been resolved recently, and repeats experiments over longer timescales are planned. For this work, it was determined for the majority of cases, the native oxide passivation was sufficient to ensure wavelength stability over experimental timescales in temperature-controlled environments.

Additional effects were observed when varying the CO_2 gas flow into the cell culture medium solution (Figure 4.8 d), the proposed medium for cells needed to be investigated. It was observed that in a cell incubator in cell medium, this progressive blueshift could be recovered by varying the input gas, and hence was interpreted as due to the formation and dissolution of a calcite layer over the disk, as an effective ~200pm diameter change, consistent with the wavelength shift. This is a consequence of the chemistry of CO_2 dependent medium, which requires gaseous CO_2 to moderate a calcium carbonate disassociation to keep the pH stable for cell cultures, a analogous situation to the in vivo

environment. However, while for cell cultures it is not strictly important to keep this value precise, the disks are far more sensitive to environmental changes. The process was completely reversable, by adjusting the CO_2, but it proved to be impractically challenging to hold stable. Using an excess of CO_2 would ensure no calcite would form, but solution would become too acidic, which could compromise the disk structure or cell viability in the experiment. Instead, it was determined to be more effective to eliminate this potential variable and to pursue a CO_2 independent medium. In CO_2 independent medium the process doesn't require gas exchange, the disk wavelength was extremely stable over long time periods (8 hours) and pulse exposure. (Figure 4.8 c).

4.5.2 Sources of Environmental Sensitivity

The disks are expected to exhibit sensitivities to their environment, due to the changing contrast and of the environment and how this interacts with the evanescent field. This is a desirable feature of WGM resonators and one that this project attempted to preserve by avoiding encapsulation layers. However, on top of refractive index sensitivity the role of temperature is significant, as this changes the internal refractive index of the disk and environment. First and foremost, a brief description of the shifts using refractive index were explored [74].

4.5.3 Refractive Index Sensing

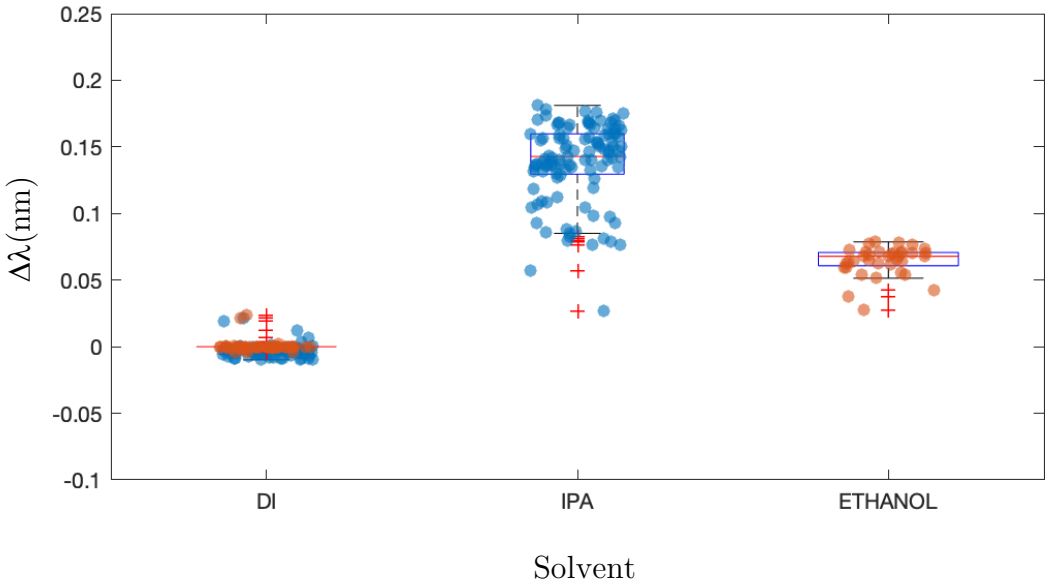

Figure 4.9 Refractive index shifts from DI water to IPA and Ethanol. Solution was substituted in dish, with focus on keeping an individual disk continuously excited to ensure it was not a different disk. Disks that were already detached represented the easiest target for sensing, but the shifts are likely partially influenced by contact with the dish base.

The refractive index sensitivity of the disks is of considerable interest, and attempts have been made to extract usable values for the sensitivity by introducing the disks to different solvents from DI water or Air. Most commonly used are Ethanol (n = 1.36) and Isopropyl Alcohol, (n = 1.3772) due to the compatibility of these samples with the testing dishes (Ibidi). Shifts in the wavelengths could be correlated to the change in refractive index, allowing for sensitivities to be calculated (Figure 4.9). The highest measured sensitivity was IPA at 3.35-3.84 nm/RIU whereas ethanol 2.30-2.54 nm/RIU for these solvents, whereas drying the disk from DI water to air – which could have represented the largest shift in possible index, had a sensitivity of 1.584nm/RIU. All of which are below predictions, as simulations discussed in Chapter 2 indicated a change of around 10nm/RIU. Possible sources of uncertainty are likely due to the experimental design, which attempted to drain and replace liquid, in a dish holding the disks which could not be guaranteed to completely substitute the liquids, particularly at the liquid/dish interface where refractive index of the dish is likely to play a significant role. So the most likely explanation for the smaller than modelled change in wavelength is simply an experimental design limitation which resulted in insufficient mixing a much lower change in refractive index than complete liquid substitution. Furthermore, the final wavelength did not settle, and it is likely that evaporation of the solvents from the

sample dish may have played a role in cooling of the resonators, resulting in a decrease of temperature and changes in solvent refractive index. Further experiments are planned to use a microfluidic system with known refractive index oils to make a full characterisation of this effect.

Efforts to isolate the sensitivity of the disks using encapsulation layers discussed in Chapter 3, resulted in a sensitivity of 0.45nm/RIU. However, the 100 nm encapsulation layer was either not stable in DI / IPA solution or was being otherwise affected, as a continuous blueshift of 60pm/min made analysis with this sample inconclusive. Optimisation of this coating and setup improvements are in development. Additionally, simulations discussed in Chapter 2 suggest that a thicker coating than the 100 nm tested would be required to fully isolate the disk from external refractive index shifts.

4.5.4 Other Sensing

Temperature fluctuations are a proposed reason for large fluctuations in output wavelength in long term stability measurements. A substantial 30°C fluctuation resulted in a several hundred picometer shift, which was completely reversable when temperatures were corrected. However, attempting to investigate this further by causing local temperature changes to fully quantify this effect were not successful. However, it was required to keep temperatures as stable as possible, as biological cells also need to be kept in a temperature-controlled environment. Further work is required to fully characterise this aspect of sensitivity.

Quantifying and characterising the sensing capabilities of these nanolasers is an open area of research, which includes an investigation into the nanolaser wavelength response to electromagnetic fields via the quantum stark effect, which arises as a phenomenon of the MQW structure and its properties discussed in Chapter 2, as well as investigating the sensitives of different laser geometries, which may have a reduced evanescent component.

4.6 Contributions

In this Chapter, I was responsible for the collection of the size and wavelength data collection, as well as acquiring and processing lasing threshold data and optimising the stability of the disks for use in future experiments. Marcel Schubert gave assistance on long term experiments.
The inverted microscope setup and lasers were previously utilised by Marcel Schubert and I made adjustments for these experiment with his assistance.
Andreas Mischok (Post-doc, Professor Gather's Lab) provided guidance on solutions for calculating the beta factor.
I assisted Lia Irvin (project student that I co-supervised) when preparing and preforming some refractive index calibrations on unencapsulated and encapsulated nanolasers.

Biophotonics Platform

In this chapter, I will discuss the utilisation of the nanodisk lasers in a biological context. This chapter will initially discuss an outline of the potential advantages of the nanolaser emitters over conventional imaging methods, followed by the setups and techniques to prepare cells and disks for investigation. The latter sections of the chapter will discuss experiments on the disks, comparing them to previous work using polymer microspheres [13], [51] to ensure consistency, as well as live/dead assays and proliferation rate assays. I will also discuss barcoding of cells and tracking through membranes. Finally, discussion ongoing work on intracellular sensing, which will touch on functionalisation efforts. Additional biologically relevant experiments are referenced as context to illustrate how the disks are a unique and useful investigative tool in environments that are uniquely constrained.

5.1 Outline

The previous chapters have described the high optical performance and potential of these nanolaser emitters in the context of a photonic structure, with some reference already on how to apply the devices in the chemically diverse environment such as cell culture. It is important to note that to apply them in biophotonics, different optimisations and trade-offs must be considered than more conventional photonic applications [148]. It is obvious that the nanolasers have highly desirable properties over conventional imaging techniques, which currently are limited by low intensity and broad colour emission, have substantial overlap between excitation and emission wavelengths, suffer from autofluorescence, and often require intense excitation that often can be destructive to the cell in order to get high resolution or contrast [16], [18], [102], [149]. However, nanolasers must be able to overcome their own performance constraints to succeed as an imaging tool.

5.1.1 Biocompatibility

Firstly, we again briefly discuss the materials used. Typically III-V materials are seen as both reactive and expensive compared to silicon and polymers, which see greater use than III-V materials irrespective of their higher material gain which provides their desirable optical properties [45], [135], [141]. This impacts the proposed platform in multiple ways. We need to ensure the disks are stable in the cell environment, so that disks do not degrade on the timescale of an experiment. In practice, this means that the disk should be stable in the chemically diverse biological environments over a week or more, which means that the disk materials need to be relatively inert in the cell medium discussed in Chapter 4, but also cell cytoplasm itself, which will be discussed later. Additionally, it must be reasonably optically stable. A common critique of nanolasers on-chip WGM lasers for these applications, but also one of their most desirable features, is that the emission wavelength is very sensitive to environmental changes [10], [16], [150], [151]. If too sensitive, the disks become less useful as a probe, as sensitivity would obscure selective sensing targets.

A second aspect is how the cells might react to potentially toxic constituent III-V materials [17], [152]. Testing for this required a large and dense sample of disks to make a viability assay statistically significant. The initial expectation was not optimistic despite the stability of the disks in solution, there were concerns about the toxicity of many of the group III and group V materials, like Gallium, Indium, aluminium and

particularly arsenic materials utilised in the wafer, are known cytotoxins and could interfere with biological experiments. Should cell health and behaviour be affected, it would necessitate further exploration of ALD encapsulation layers and bio-coatings such as biotin or mode complex crosslinked phospholipid membranes [76], [153], which are often used to make other toxic nanoprobes bio-compatible [154], [155].

5.2 Setups and Procedures

The setup to investigate the nanolasers is as described in Chapter 4 (Figure 4.1 b). However, work with the cells required additional equipment to be added. The samples were examined in a cell incubator, initially using a bioscience tools (TC -1-100-I temperature controller, with CO_2 Pressure controller) setup, but then moving to a reference temperature gathering setup to ensure accurate and precise temperature control (okolab H301-K, Stage top incubation system). These incubators promise the control of temperature to within 1°C of the set temperature, required for cell health as well as for removing any environmental influence on disk behaviour.

Biological contamination is a risk when attempting to transfer a foreign body prepared outside a sterile environment (such as the nanolasers) to a cell culture. To ensure this is mitigated, additional washing steps are used to disinfect the disk dishes (70% IPA: DI Water solution, autoclaved DI water, then finally PBS and cell culture medium) in a sterile laminar flow hood. The cells are then cultured in these disinfected dishes in the same sterile environment, ensuring proper practices to reduce cross-contamination. NIH-3T3 and other dividing cell cultures were kept in a continuously reproducing state, using a process called splitting: by releasing the cells using Trypsin to suspend cells, then add a few thousand detached cells (calculated as a concentration from a cell counter plate) to a flask of cell medium. Cells were given time and space to divide, they would typically reach confluence (a monolayer of cells) in 3 days. Non-dividing cells, such as Primary human macrophages, were used as soon as possible after preparation, ensuring the cells had fresh medium every 3 days should it be required.

Staining the cells with fluorescent dyes was used as a supplementary tool to allow for cell counting, live/dead assays and confirming disk internalisation. These cells were live stained in the laminar flow hood. The majority of stains used in the project are listed as follows. Nuclear stains (Hoechst 33342) and Propidium iodide (Invitrogen), Cytoplasm stains such as Calcein AM (Invitrogen) or Celltracker Green (CMFDA) and membrane stains Wheat Germ Agglutinin WGA (Alexa Flour 488, 633). A combination of these stains were used to enhance cell structures of interest for counting and accurately

defining boundaries. In some experiments, NIH 3T3 cells were used that were genetically modified to express Green Fluorescent Protein (GFP) to image the cells over long time periods.

These stains could be examined using the EPI-Fluorescent light discussed in Chapter 4, but for 3D localisation the inverted microscope was additionally equipped with a laser scanning confocal scanhead (Nikon TE2000 and C1si) which was equipped with a 404, 488 and 561 nm CW lasers and 515/30, 590/50 and 650LP detectors as well as a transmission detector for brightfield imaging. For higher resolution and more fine control of the excitation and emission detectors, a fully equipped confocal microscope with modern imaging enhancements (Leica TCS SP8) was used. This could achieve nm resolution over long scan durations utilising 4 lasers providing 10 possible excitation wavelengths between 405 and 633nm with adjustable detectors to provide well resolved channels.

For long term imaging and investigation or to halt the experiment, cells were 'fixed', a process that uses chemical crosslinking agents (4% paraformaldehyde) to kill and preserve cell cultures. These fixed cultures allowed for investigation in non-incubated environments and for long-duration investigation of the samples. The samples still had to remain in solution to retain shape, but should the fixed samples require to be dried, required for SEM imaging, further steps included either supercritical drying in methanol, or using hexamethyldisilazane (HMDS) as a chemical drying agent.

5.3 Disk Identification

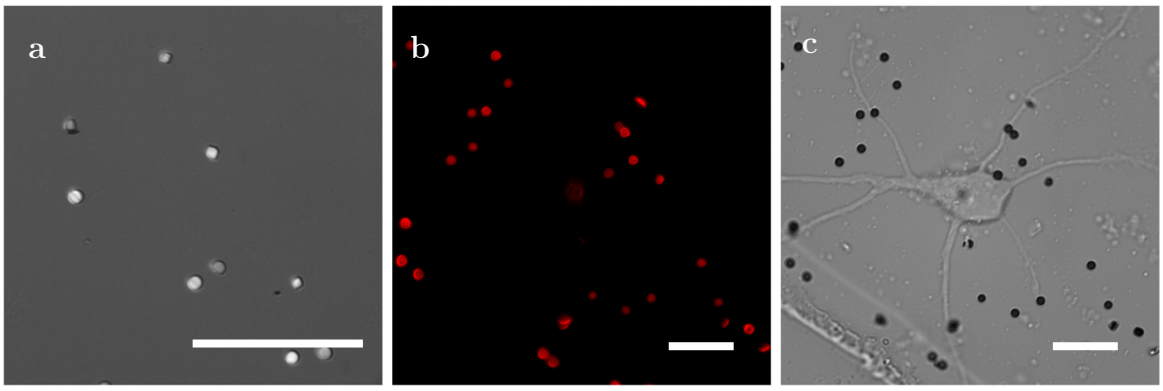

Figure 5.1 Images of disks in microscopy, a) Reflection, note that the intensity is angle dependant. The white light from the fluorescence bulb is UV filtered to reduce cytotoxicity but the intensity is still likely dangerous to cells, so this modality is most often used on fixed cells or dishes before cell introduction. b) Fluorescence using DS-red filter for excitation at 548-580nm, collected using a 600nm LP with an exposure of 2 seconds. c) In brightfield imaging, the disks are opaque and are relatively easily resolvable in this configuration, however, if obscured by cells (see the disk in the central neuron) they are easy to mistake for other naturally occurring structures. Scale bars, 10 μm.

As discussed in Chapter 4, many of the characterisations of disks were done on wafer to aid in identifying and locating the sub-μm devices. Once detached into an environment that was optically complex, it was essential that the disks were able to be identified easily from the cell and other matter in medium. Though this was typically straightforward, as the disks are dark, opaque objects, occasionally it was important to distinguish them from other circular translucent objects. This was accomplished by two principal methods as depicted in Figure 5.1. As the disks are highly reflective as well as non-transparent, in simple dish experiments the disks could be easily identified by using their reflection of the unfiltered epifluorescence light source. However, there is a substantial phototoxicity risk involved with such bright light sources [156], and small bubbles could lens the light and thus be mistaken for a disk. The second approach is to use fluorescence as described in Chapter 4. Typically, they would fluoresce when excited with any wavelength shorter than the emission profile, however, to ensure minimal phototoxicity to the cell and to avoid exciting and bleaching other potential fluorophores in the experiment, wavelengths with insufficient photon energy to excite these fluorophore was used. This was achieved with a DS-Red filter illuminating with 548-580nm and collecting wavelengths past 600nm [157]. Fluorescence imaging required second long exposure times as the disks are small. The most effective excitation could be accomplished with the OPA and diode laser at 1000Hz repetition rates, exciting at just below laser threshold (~20 $\mu J/mm^2$). However, this required beam expanding optics to be useful, which were not implemented until late stages of the project. CW lasers also provided good illumination capability, so for more optically complicated experiments and exact positioning of the disk within the cell, the confocal scanning lasers (561, 633nm) provided excellent illumination and contrast from other fluorophores and localisation of the disk to confirm internalisation, which will be discussed further in the following section.

5.3.1 Confirming Internalisation

In previous work, the polymer microsphere WGM lasers were functionalised with antibody labels which would express different emission depending on whether inside or outside the cell body [13], which allowed for quick and easy quantification of internalisation. For the nanodisks, functionalisation using this technique would require additional fabrication refinement and exploration, as the binding of antigens and bio coatings to III-V materials is not as well explored as for polymer [158], silica and metallic nanoparticles [159], [160]. Other potential avenues included a Transmission Electron

Microscopy (TEM) slice of a fixed cell, which would have required refinement of a cell fixing process that preserved both the nanodisk and the cell structure, as well as optimising the TEM procedure.

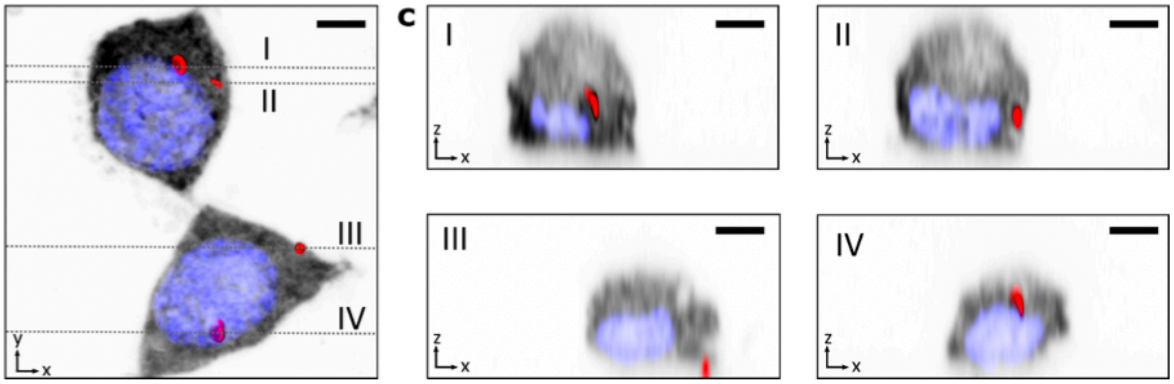

Figure 5.2 Confocal images of 3T3 cells post division. Note the presence of 4 disks (red, I-IV) with respect to the cytoplasm (black) and cell nucleus (blue). The optical sectioning of the cells is more than sufficient to conclude disks I, II and IV are within the cell cytoplasm and are co-localised with the nucleus, however disk 3 can be concluded to be under the cell. Disks that co-localise with the plane of disk 3 can be considered not-internalised, even if the cell is above them. Scale Bar 2μm. Figure reproduced from supplementary material [55].

With these approaches considered, confocal microscopy was selected to confirm internalisation as it provided excellent optical sectioning and the combination of bright fluorescence profile of the disks and good localisation of non-specific fluorescent molecules (Figure 5.2) [45], and was previously used to confirm internalisation of the polymer microspheres [13]. Using the Leica confocal system, very precise localisation of the nanolasers could be accomplished (Figure 5.2), which enabled the identification for disks within or under the cell. For ideal imaging conditions, the cells were fixed and stained with fluorescent indicators, including the membrane stain WGA and Hoescht stains. The disks are much more strongly fluorescent than the dyes used, and fluoresce in the far red, so can be resolved separately from the even the most red-emitting dye used (WGA-633). However, the inverse is not true, as disks fluoresce strongly enough to be detected in the detection channel of WGA.

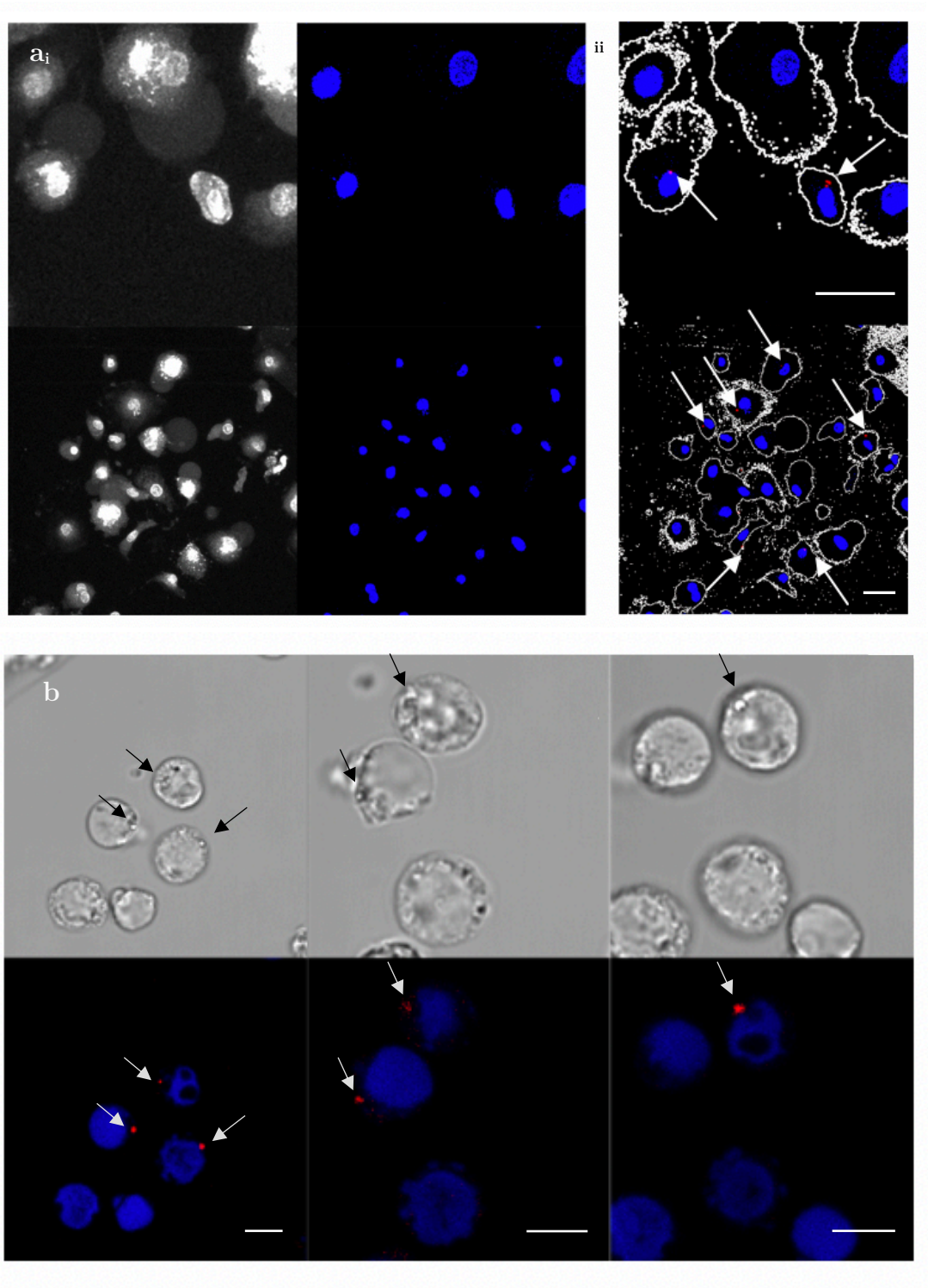

Figure 5.3 Distinguishing disks in macrophages and human T-cells, a) i. maximum intensity projection of confocal slices of macrophages. Showing cytoplasm stain (CMFDA) white and nucleus (blue). ii. The membrane boundary of the cell can be easily determined in the macrophages in i., and the highlighted disks (arrows) are within the membrane boundary. Scale bar 30μm. c) Human T-cells are not adhered, and these slices indicate disks that are co-localised with the nucleus within the membrane of the cell, an indication that the disks are internalised, scale bar 5μm.

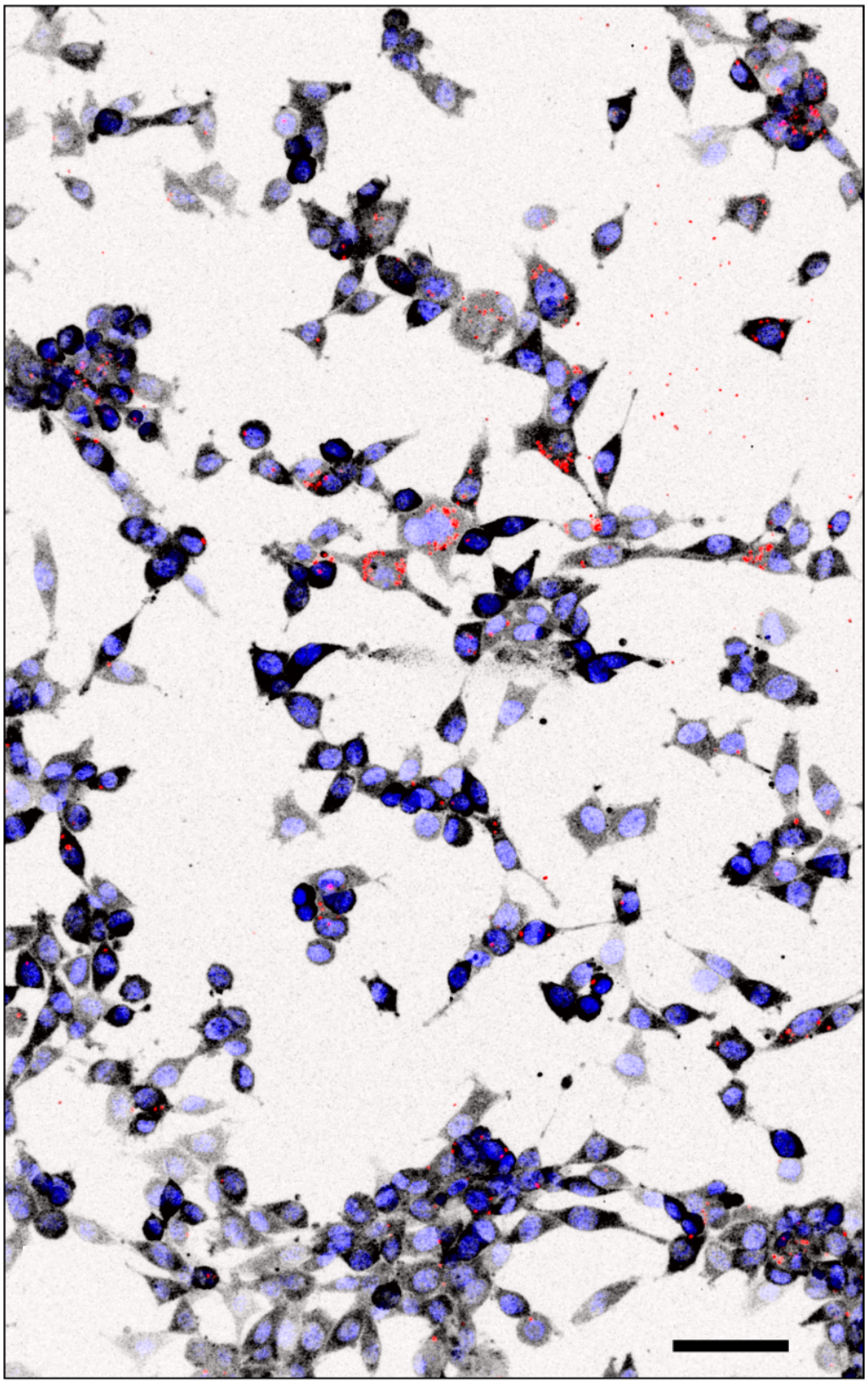

Figure 5.4 Widefield view of a 3T3 sample after 24 hours of disk uptake, with disks (red) and Cytoplasm (black) and cell nucleus (Blue) Most disks (>70%) have been uptake in this image, and the largest body of uninternalised disks (see arrow) are likely in a region where cells have not explored. A more motile cell line or allowing the cells to reach confluence would approach 100% uptake. Scale bar 50μm. Figure reproduced from supplementary material [55].

This allows for relatively easy identification of the disks instead of fluorescent material, and because the disks are so small compared to the body of the cell, it was straightforward to distinguish disks within the cell body to those under it. Live cells moved too quickly to acquire high enough resolution to confirm that the nanolasers were in the cell body, so the cells needed to be fixed and stained (Figure 5.3 a,b). For cells that were free floating, like T-cells, Brownian motion of the fixed but detached cells was still significant so the quality of the capture had to be reduced. Nonetheless it is possible to confirm that the lasers are co-localised to the nuclear membrane in these images, as well as their motions corresponding to the cells motions (Figure 5.3). To make statistical inferences of the amount of disk uptaken by cells, large numbers of disks and large viewing areas were used of cell cultures fixed after 24 hours. From FOVs such as the representative example in Figure 5.4 that for the NIH 3T3 cells, a disk uptake efficiency of $(76 \pm 5)\%$ was deduced, which was comparable to other qualitative cell investigations. By refining the stains and optical sectioning with respect to working distance, the disks could also be located in 3D environments, see 5.5.3.

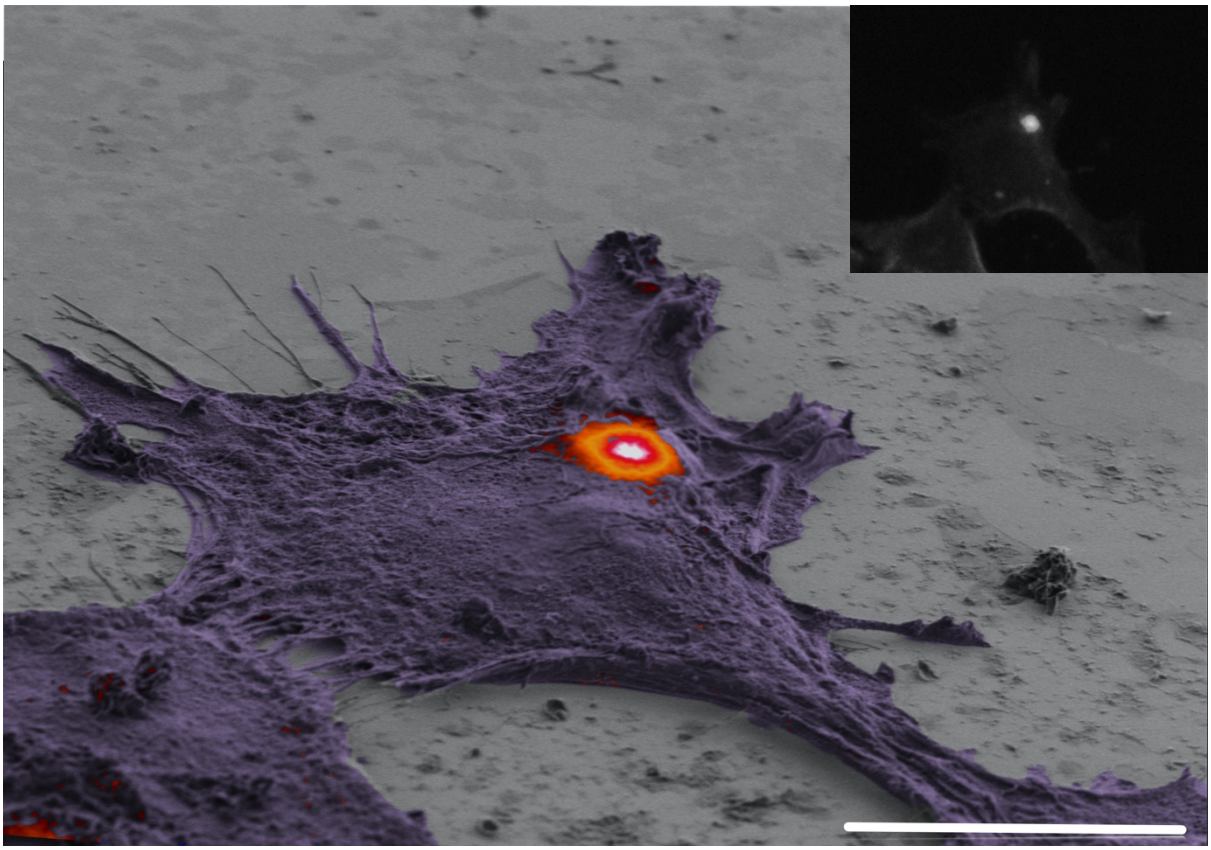

Figure 5.5 False-colour SEM image of a fixed and chemically dried NIH 3T3 cell (purple) with internalised disk revealed by fluorescence signal (red overlay and inset). The disk was not resolvable within the cell through SEM but was easily visible using fluorescence. Scale bar 10μm.

Efforts were also made using SEM to image the disks through the polymerised cell membrane (Figure 5.5). This required the either critical point drying or chemical drying to accomplish a dry, fixed sample with preserved cell morphology. This procedure was successful; however, the scattering of electrons was too strong to resolve this without FIB and TEM slices, which would require precise foreknowledge of the location of disks within cells. The most success using this technique utilised the high refractive index wafer substrate with scattered disks, introducing cells to the wafer substrate and measuring possible intracellular disk candidates (This was not typically done as the GaAs is not an ideal environment for the cells to be introduced). In this configuration, it was possible to exclude the possibility of a lasing disk being under a cell, as a resonator would not lase due to the lack of refractive index contrast with the substrate. By correlating laser excited fluorescence to a SEM image of the same cell, it was also possible to exclude the possibility that a disk was on top of the cell.

Finally, rather than relying on the natural cell endocytosis, efforts have been made to inject disks into desired cells. So far, the yields for disks in solution have been limited, and they show preference to adhere to dielectric surfaces like the tapered glass needle used for injection. In addition, the magnification of the micromanipulator (10x used) makes identifying the disks extremely challenging. Nonetheless, improvements to the setup and disk solubilisation make this a promising avenue to control uptake of resonators and select cells of interest to analyse.

5.4 Investigated Cell Types

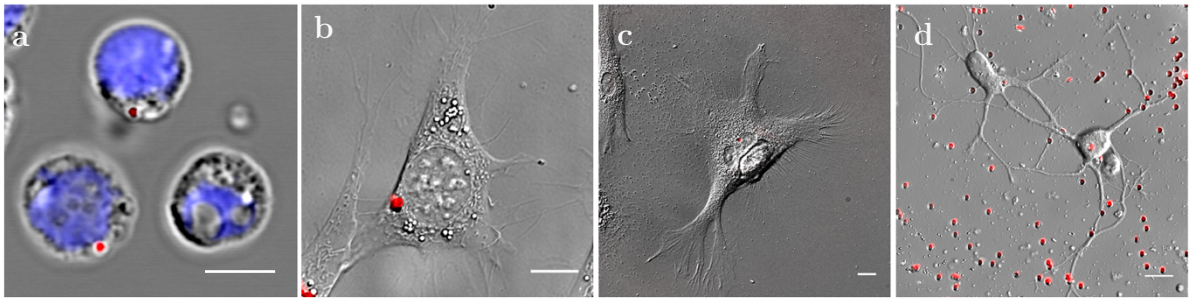

Figure 5.6 Representative cell examples investigated in this project. a) Human T-Cells, immune cells that are not substantially larger than their nucleus (blue). Disks (red) are co-localised and are carried with the fixed cells as they exhibit Brownian motion.Sscale bar 5μm b) DIC image of NIH-3T3 cells with 2 closely spaced lasers (red fluorescence). c) Macrophages can exhibit 2 phenotypes, a more motile, bunched cell and a wide adhered cell. These wide, more stationary cells can be used to attempt to sense cell dynamics. d) Neuronal cells. These cells are not typically motile or phagocytotic, so present a challenge for natural disk uptake. Large numbers of disks (red) were deposited to maximise chance of uptake. Adapted from [55].

To properly understand the versatility of the nanolasers as an intracellular probe, internalisation of disk lasers was tested for a range of different cell types (Figure 5.6). This included the previously discussed primary macrophages and 3T3 cells, as well as Dendrocytes, T-Cells, Neurones, Cardiomyocytes and modified HEK cells. In all cases, the action by which these cells absorb the disks is via natural endocytosis or phagocytosis [161], a process by which the cells enclose a foreign body or chemical using its membrane. The process of endocytosis results in the formation of fully enclosed intracellular vesicles which contain the internalised material. It is likely that without membrane rupturing antibodies [162], the disks are most likely enclosed within this membrane for the duration of the experiment, which may need to be addressed for future intracellular sensing experiments.

Different cell types have merit for different experiments. NIH 3T3 cells provided a good model to investigate migration through confined environments and provided a good analogue of a generalised fibroblast cell [163]. They could be prepared to express GFP, allowing for long term experiments that required a fluorophore that could resist bleaching over the timescales of the experiment. Primary Macrophages were cultured from human blood samples. They are specialised immune cells for absorbing foreign bodies. They are highly mobile and do not divide, providing an ideal cell to investigate barcoding and tracking for initial tests, but are also of interest to study in a broader context as their invasive characteristics could elucidate cancer metastasis [164], [165]. Stationary cells, such as Cardiomyocytes provide an excellent cell type to study, as these adult cells do not endocytose objects, and provide a dynamic environment - the beats of the cell – which can be sensed by the shift in wavelength – suspected to be an increase in refractive index through to more dense myosin fibres [166]. The disks therefore act as a remote, local, ECG, measuring distributed changes across the same cell. Cells, such as Neurons and T cells that are typically considered too small to engulf large objects, allow to showcase the value of the sub-μm diameter and 180 nm thickness of this work's nanolasers, as previously reported cell lasers are all substantially larger. Additionally, these cells are of particular interest as many of these smaller immune cells represent an important target for cell tagging due to their complex role in cancer progression and immunotherapy [167]. The uptake of nanodisk lasers into the soma of cultured primary neurons, which are also typically not substantially larger than the cell nucleus it contains, presents significant potential to investigate the cell dynamics within individual neurons, a field of active research [81], [168], where the quantum stark effect briefly discussed in Chapter 2 could potentially be able to detect neuron firing [80].

5.5 Cell Viability Investigation

As described in the outline, it is vitally important that the investigated cells tolerate the III-V materials. Otherwise, encapsulation would be an essential fabrication step. Initial tests introduced Human Embryonic Kidney (HEK) directly onto the material substrate, with disks on columns, which presented the largest amount of disk material to the cells, as there is a much greater surface area of the harmful material than we expose them to by only introducing the individual disks. This was done to observe whether the material was immediately toxic and to inform the planning for future steps. In leu of any live/dead assay, we wanted to observe if a characteristic 'Death Halo' was visible around the III-V material, so it was exposed to a large amount of cells.

Fortunately, after three days no such halo was formed, and the cells were securely adhered to the surface and had undergone some division. The cell shape, such as elongation, can indicate good or poor cell health, and this indicated that the cells were indeed stressed from this level of exposure. Even with this concern, the result was encouraging. The conclusion reached was to generate large numbers of disk material to explore the viability of the nanolasers without the substrate of GaAs, which is known to be more soluble and cytotoxic than the other materials in the MQW structure [152]. Similar increased rates of cell stress were observed if fragments of GaAs were present near cells as a contaminant during the detachment processes outlined in Chapter 3.

5.5.1 Live/Dead Assay

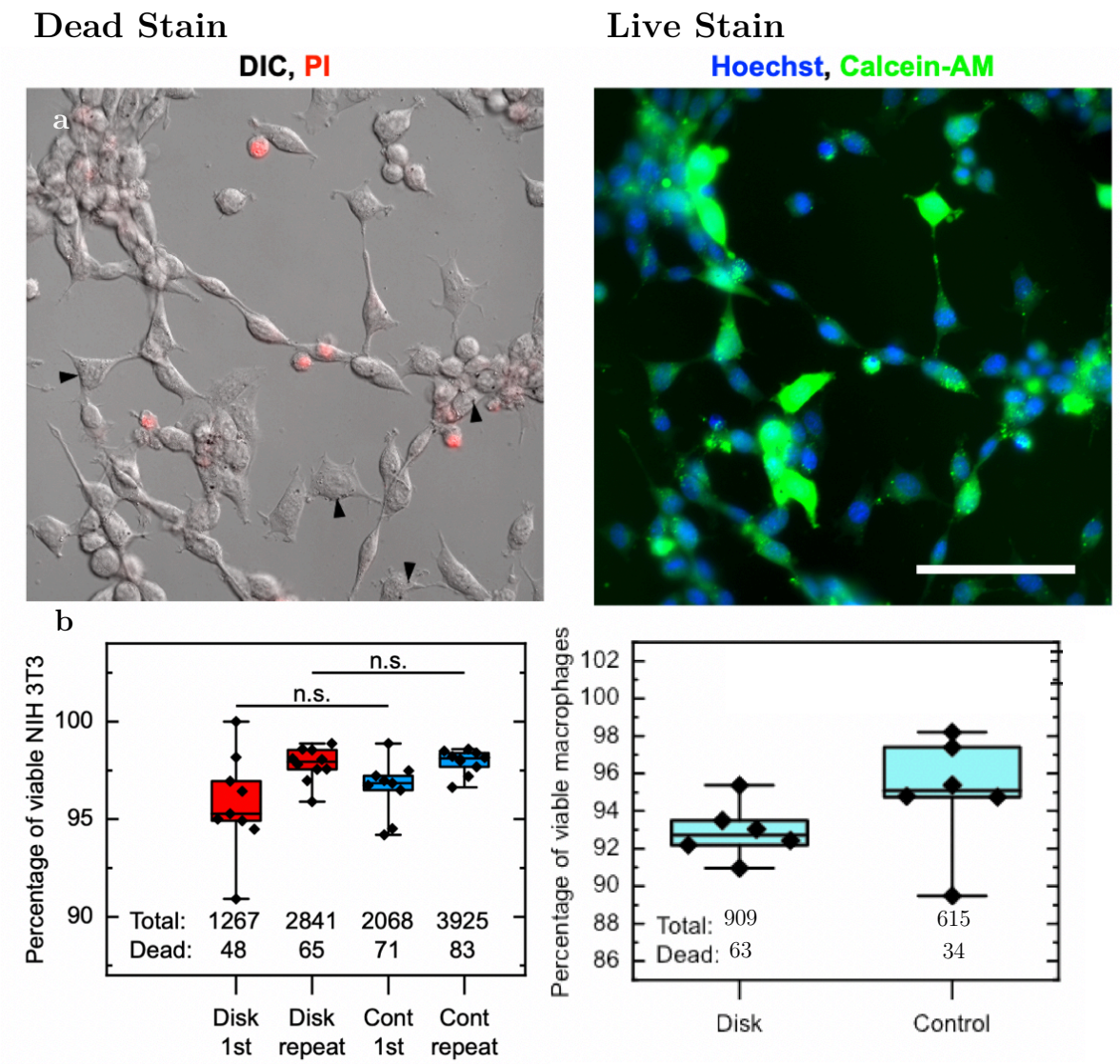

Figure 5.7 Live / Dead assay to investigate possible disk cytotoxicity risk. a) Representative FOV of 3T3 cells, arrows indicate disks in cells. PI (red) indicates a dead cell. Only PI co-localised with Hoescht (blue) is counted as a dead cell, as the PI dead stain is a DNA stain. Calcein-AM (Green) is used to confirm cells that are alive. b) Box and whisker plots displaying the distribution of the percent of viable 3T3 and Macrophage cells. The overlap of the interquartile range of disk exposed and control cell cultures was compared to assess statistical significance. Adapted from Supplementary information [55].

Using the more refined disk detachment procedure, a set of commonly used viability assays were preformed [169]. These Live / Dead assays, use Calcein AM and Propidium Iodide (PI). Calcein AM is a 'live' stain, or a molecule that only is fluorescent if the cell is alive and able to absorb the precursor molecule, where it is converted into a green emitter in the cytoplasm of the cell. PI is a red fluorescent 'dead' stain, that will only

be internalised and concentrated in the nucleus of dead cells with a ruptured membrane. With statistically large numbers of cells and disks, this can confirm more quantitatively what the effect of disk presence has on a cell by comparing a disk containing dish to non-disk containing control samples, cultured simultaneously in sterile dishes. These assays were applied to Primary Macrophages and 3T3 cells as representative examples of non-dividing and dividing cells respectively (Figure 5.7).

5.5.2 Proliferation Rate Assay

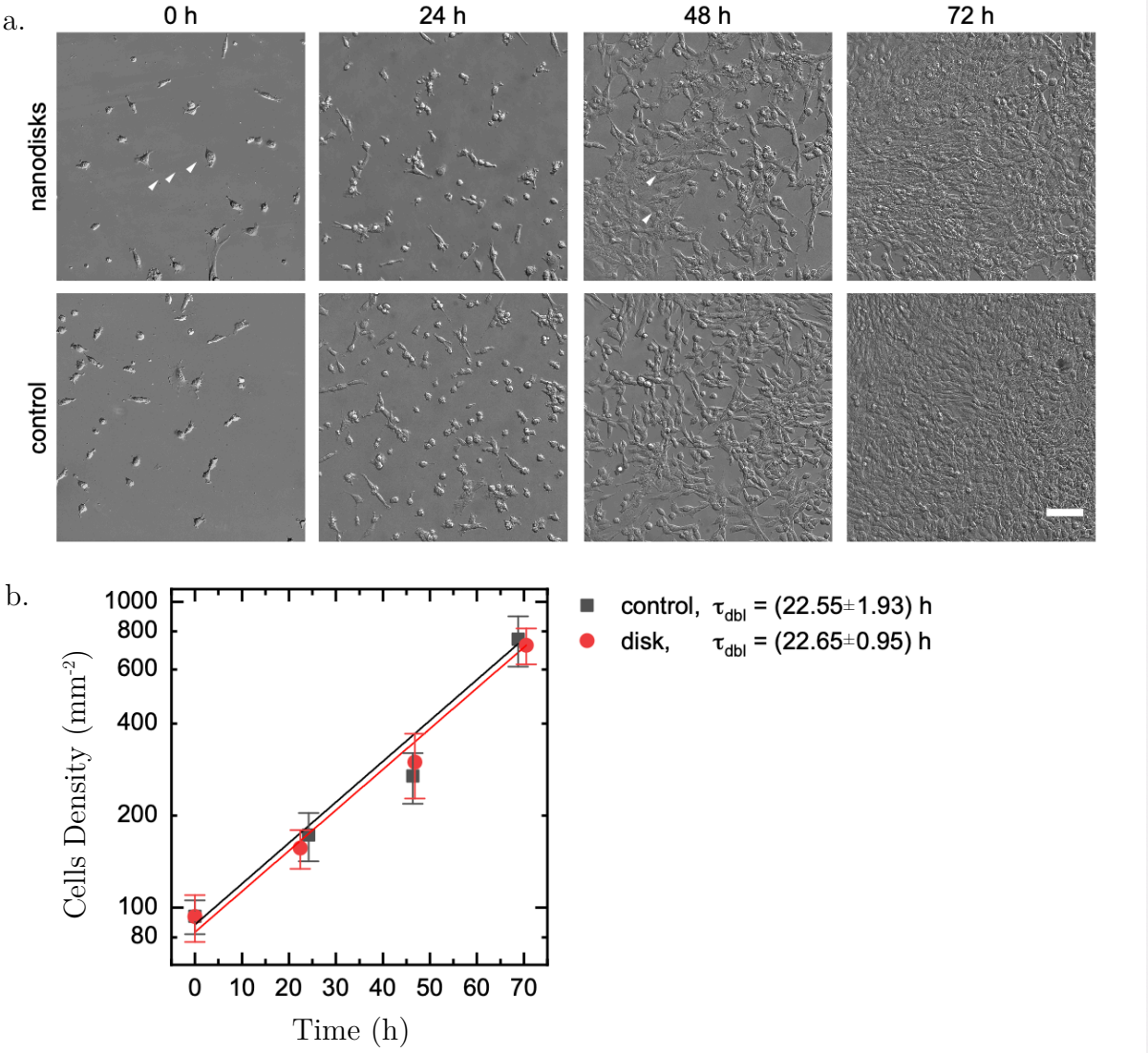

Figure 5.8 a) Representative image of cell proliferation in 24-hour intervals, until confluence is reached. Confluent cells were counted using a smaller representative frame and assuming uniform density. Scale bar 25 μm b) Statistics from all FOVs for 2 independent trials, comparing 2 control samples. Adapted from supplementary material [55].

The proliferation rate of NIH 3T3 cells was not affected by the presence and internalisation of nanodisk lasers (doubling time, $\tau_{dbl,disk} = (22.65 \pm 0.95)$ h versus

$\tau_{\mathrm{dbl,control}} = (22.55 \pm 1.93)$ h, Figure 5.8). Additionally, to see if the disks affected the behaviour of the cells more subtly, a reproduction rate analysis or proliferation assay was prepared using 3T3 cells, as it was assumed that any small disturbance or minor toxicity would become more visible over longer time scales and accumulated effects through several daughter cells.

Cultures of primary cells containing disks were found to remain viable for at least 2 weeks. Whilst the live/dead assay showed no statistical difference for the two independent trials of 3T3 cells, macrophages appear to have a small statistical decrease in viability, which is likely a result of difficulty interpreting the fluorescence results due to irregularities in the fixation process, where the PI has a very high background fluorescence and di.

5.5.3 Additional Viability Assays

A minor concern was the toxicity of the polymer resist, which should be substantially less of a threat than the materials in the disk but a removable one. Two glass slides coated with developed PMMA and SU8 were exposed to HEK cell cultures and had no effect on their behaviour after 2 weeks. It was concluded that it was not a significant factor in cell health. In any case, the amount of SU8 apparent after RIE oxygen ashing should be negligible and did not show any significant peak for carbon under EDX.

To further refine this investigation, further tests on the viability will focus on the utilisation of potentiometric dyes to monitor cell health via mitochondrial membrane potential (JC-1 Invitrogen), which detects the early stages of apoptosis and mitochondrial poisoning, which would reveal possible cytotoxicity and cell stress of disk containing cells, particularly for more sensitive cells such as neurones.

5.6 Cell Lasing Experiments

Once introduced into the cell environment and confirmed to be safe and stable for long term experiments, the focus fell on utilising the disks as intended. This section will outline the different laser tests performed on the cells, focusing principally on the macrophages and 3T3 cells for in-cell laser characterisation, then discussing the tracking and membrane experiments. There will follow a discussion on the sensing capability of the cell, which is an area of ongoing research.

5.6.1 Intracellular Lasing

Nanodisks continued to produce narrow band laser light when inside a cell with stable linewidths, 0.2–0.25 nm. This observation is based on statistically significant sample sizes; lasers were introduced to more than 50 independent cell cultures. A macrophage with 2 nanodisks lasers was followed over 8 h and found that its intensity and peak position varied over time more so than when characterised in solution, where fluctuations were only 80 pm. This is presumably due to cellular motion which would induce changes in the position and orientation of the nanodisks, thus affecting both the excitation energy received and amount of emission that is collected by the microscope objective, as well as affecting the immediate environment of the disk through the dynamics of the cell. As described in Chapter 4, the performance and quality of the disks could be estimated by checking the laser threshold.

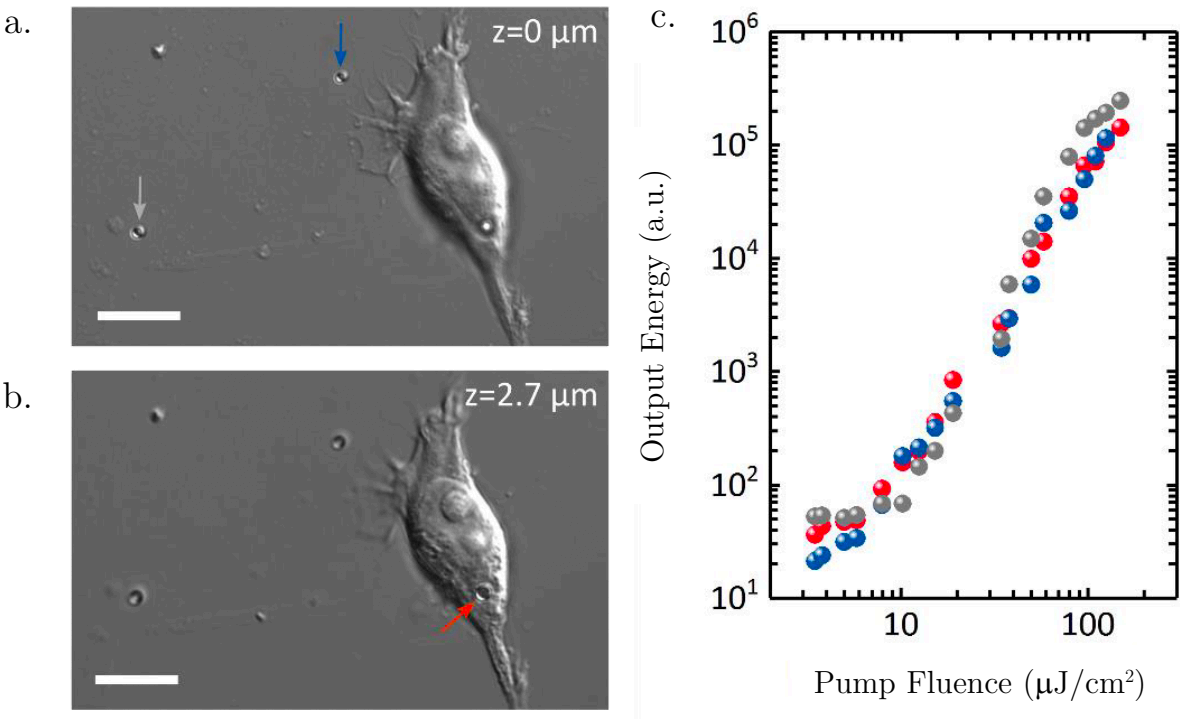

Figure 5.9 a) Two disks outwith a fixed cell that have never been internalised, but are otherwise identical to an intracellular disk (b) which has been exposed to the cell cytoplasm. c) Threshold measurements for the 3 independent disks in a) and b) indicating no substantial difference between them. Scale bar 10µm.

Threshold measurements carried out in solution were compared to disks in the cell medium outwith a cell to those within a cell (Figure 5.9). This would indicate whether the thresholds were negatively affected by being within a cell. The cell had to be fixed for this test as the aforementioned fluctuations in position and orientation make accurate recording of a light-in/light-out curve in live cells impractical. This is because the

threshold measurement occurs over timescales of visible cell motion. It was not expected that the thresholds would be substantially affected, as the Q factor of the high refractive index nanodisks (3.55) is expected to reduce only marginally when going from cell culture medium (n=1.33) into the cell ($n_{cell} \approx 1.37$). A fixed cell, however, could provide information as to whether the decreased contrast of refractive index and time of exposure to the cell environment had any effect on thresholds. After 24 hours, a disk containing cell culture of NIH 3T3 cells was fixed and an isolated cell with two nearby uninternalised lasers were measured for threshold and compared. In this configuration, it was confirmed that lasing threshold of a disk located in a fixed cell was not significantly different from the threshold of the nearby disks that were not internalised. In addition, typically nanodisks located in live cells reliably showed lasing well above threshold at pump fluences ≤100 µJ cm^{-2}. Lasing spectra also maintained high signal-to-background ratios of above 20 dB.

However, several cell cultures of the project experienced a progressive blueshift of the laser wavelength for lasers within cells, presumably from an incomplete or otherwise ineffective oxygen passivation step, as the most affected samples were correlated with contamination in the RIE. The rate of blueshift ranged from unusably rapid (1nm / hour) to almost imperceptible. If the resulting blueshift was slow, the disks could still be relatively useful for certain experiments, e.g. for sensing over short time scales, as the blueshift typically did not affect the intensity of output. For optimised lasers, this blueshift did not constitute an issue.

5.6.2 Optical Barcoding

The previously demonstrated Polymer microsphere lasers exhibited multiple modes, due to the FSR and broad optical gain of the spherical resonators allowed for first order TE_x-TE_{x+1} mode spacing (as seen with the larger micro disks in Chapter 4), as well as TE_x-TM_x mode pairs, which are not found in the nanolasers. This spectral information alone allows for accurate diameter measurements without co-modalities of measurement such as microscopy that the nanolaser disks require [51]. Additionally, it was possible to disperse a large spread of sizes (up to 10um) into a cell culture and distinguish each from the FSR, whereas the single mode emitting nanolasers are not so easily distinguishable, although larger resonators could use dual modes in the FSR to measure in this way. With the single mode emitting nanolasers, in optimal circumstances, 300 disks could be confidently distinguished from each other, assuming a 200pm spectral bin.

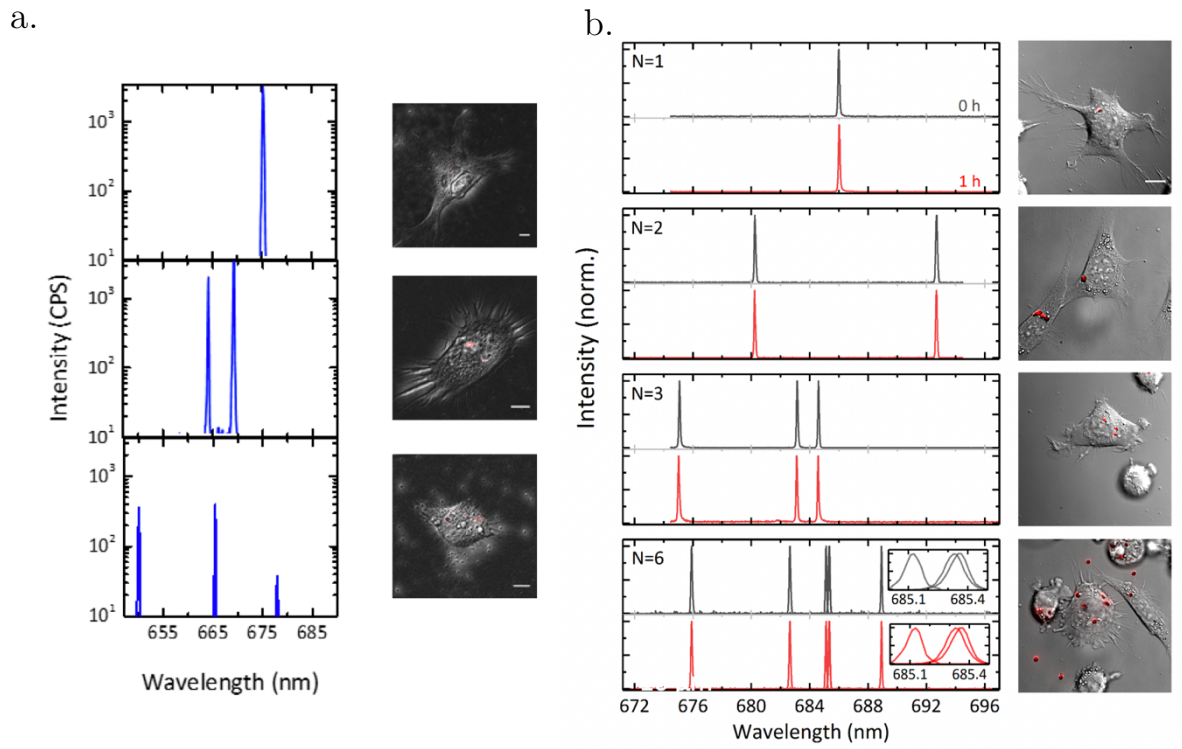

Figure 5.10 Optical barcoding examples. a) Macrophage tags simultaneously excited with an expanded beam. Showing the good peak shape and small size of nanodisks (red) in the representative images. b) 3T3 barcodes, separated by 1 hour time periods to show good peak confirmation and stability. N=6, features 3 very closely spaced wavelengths that are resolvable even with significant overlap. All scale bars 10 μm. Adapted from supplementary material [55].

For some experiments this could be sufficient, however, by considering multiple single mode nanolasers as a multiplet, these devices can potentially be used to barcode larger numbers of cells than the microspheres without significantly changing the load on the cell. The volumetric footprint of each disk is such that each cell can internalise multiple nanodisk lasers without incurring a significantly greater payload. The consequence of this is that the multiplexed emission spectrum of all the internalised lasers in a cell provides a highly characteristic optical barcode, thus uniquely labelling large numbers of cells by relying on the statistically improbable likelihood that, for 3 or more disks, the same number of disks and wavelength distribution would be identical between cells (Figure 5.10). To test the viability of this barcode, this project tracked NIH 3T3 and macrophage cells with $N = 1, 2, 3$, and 6 lasers using conventional microscopy, and compares spectra recorded 1 h apart. The spectral shape of all lasers remained highly conserved. The emission from cell with 6 internalised lasers illustrates that even very closely spaced lasing peaks can be resolved separately due to the large signal-to-background ratio of the laser emission. As a conservative estimate, it can be assumed that lasers can be clearly identified if their peak wavelengths are >0.4 nm apart (i.e. five-fold more than the maximum wavelength shift observed in the figure). Given the

wavelength tuning range of the nanodisks lasers demonstrated in this project (40 nm) and the ability to tune lasing wavelength during fabrication demonstrated in Chapter 4, and assuming there are $N = 6$ disks per cell, one could thus uniquely tag $>10^9$ cells. These initial tests indicate that it is possible to label cells with $N \geq 6$ disks, although further optimisation may be necessary, particularly if these cells are designed to be used as a barcode, it may be advantageous to investigate methods of binding the disks together as an indivisible multiplet before introducing them to cell cultures, e.g by encapsulating groups in polymer or otherwise inert low refractive index agent. This would combine both the advantages of encapsulation and unique barcode development.

5.6.3 Intracellular Lasers in Confined Environments

This project wanted to provide an illustrative, biologically relevant example of the advantage of using nanodisk lasers and demonstrate that cells tagged with nanodisks were unencumbered. In vivo, cells typically move within a 3d confined environment, regularly squeezing through gaps smaller than the cell, with extreme examples involving macrophages and neutrophil type cells passing through ~μm sized pores that require disassembly and re-assembly of the nucleus [170], a phenomenon that requires that the nanolaser tags are even smaller than the size of the largest cell organelle. This cellular process of nuclear disassembly/reassembly is a key part of cancer metastasis and invasion, so demonstrating that the disk containing cells can migrate within such a spatially confined environment would indicate the disk's capability as a tool to investigate these processes. For this, a transwell migration assay was adapted from the widely used procedures utilised in cell biology as an tissue membrane analogue to study tumour cell invasion [171], [172], transepithelial transport and paracrine cell-cell interactions. [173] This study was attempted with macrophages, using a nutrient gradient and chemoattractant, however, the large working distances required reduced the quality of optical sectioning, so presented difficulty in determining what side of the membrane the cells were on. Attempts were made to use a fluorescent blocking opaque membrane such that only cells that had crossed the membrane would be visible, but this presented difficulties in acquiring data for successful disk containing cell crossings as the top surface was not imageable. Additionally, the setup described in Chapter 3 with the incubator stage was not equipped for the automatic exchange of the nutrient depleted medium and nutrient rich medium, so the experiment was limited by diffusion of the nutrients across the concentration gradient. To address these issues, the adapted setup utilised eGFP expressing, disk containing NIH 3T3 cells. These cells were initially

'starved' in nutrient deficient medium, then introduced to the membrane, and then using a similar concentration gradient, attracted through the pores of the transwell membrane. The design utilised a larger membrane and dish area, allowed for medium to be more easily manually exchanged before and after experiments, and the working distance required was minimised by using spacer beads to closely separate the membrane and dish base, which allowed for the use of an oil immersion objective. Utilising the integrated confocal microscope with the laser characterisation setup, it was possible to observe the top and the bottom side of the membrane with good optical sectioning. Attempts were made to make a time-lapse of a cell crossing, however the membrane still introduced significant scattering, so to image the top surface required cytotoxic levels of excitation light and this adversely influenced the cell behaviour.

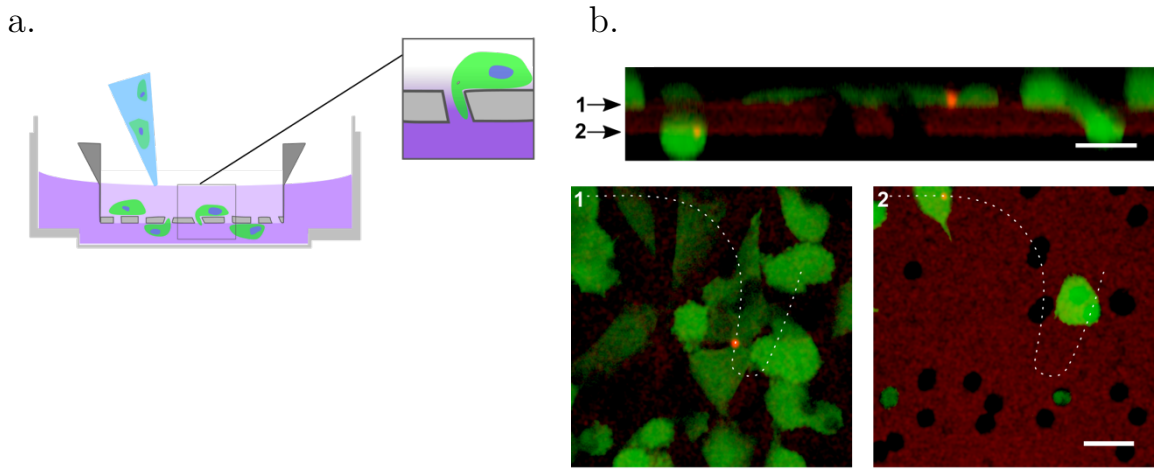

Figure 5.11 a) Schematic of membrane transwell assay, with invading cells (green) deposited on the top surface and migrating through 8um pores into the bottom surface, attracted by a rich nutrient suspension. b) Confocal image of a representative slice, showing disks (red) on the top and bottom surface internalised within the body of the (Green) cells, with the slicing to indicate the holes in the membrane for the orthogonal view. Scale Bar 15μm. Adapted from [55].

Figure 5.11 shows confocal microscopy data of a region with one disk-containing cell that has migrated through the membrane and one cell that has not, as well as a cell with multiple disks in the process of crossing. In a typical membrane experiment, >10 cells with disks were found to have crossed the membrane in the investigated 1 mm × 1 mm area; with no substantial discrepancy of disk containing cells above the membrane compared to below. There is some indication that, due to the lower number of disk containing cells observed above the membrane compared to those that had crossed, that such cells were perhaps more likely to cross. This is likely an artefact of the experiment, as healthy cells that are able to endocytose are also more likely pass through membranes. Additionally the top surface is difficult to resolve. The crossing of disk-containing cells was be confirmed in four independent experiments, though several other potential

crossings were observed in the process of developing this experiment. Nanodisk lasers were visible and exhibited narrowband spectra regardless of their position on the membrane, which only affected how much pump light the disks received. This demonstrates how these lasers can be used to barcode individual cells during migration through spatially confined environments. Using a similar technique, others have built upon this work to label large numbers of cells with a similar but infrared emitting disk in a cultured tumour cell aggregate and track them as the tumour droplet spreads [147].

5.6.4 Optical Sensing

This section addresses another significant property of the nanolaser resonators: their ability to sense the refractive index changes of their environment. Additionally, the other sensitivities discussed in Chapter 2 and 4 give promise that the disks could be highly useful, versatile intracellular monitor.

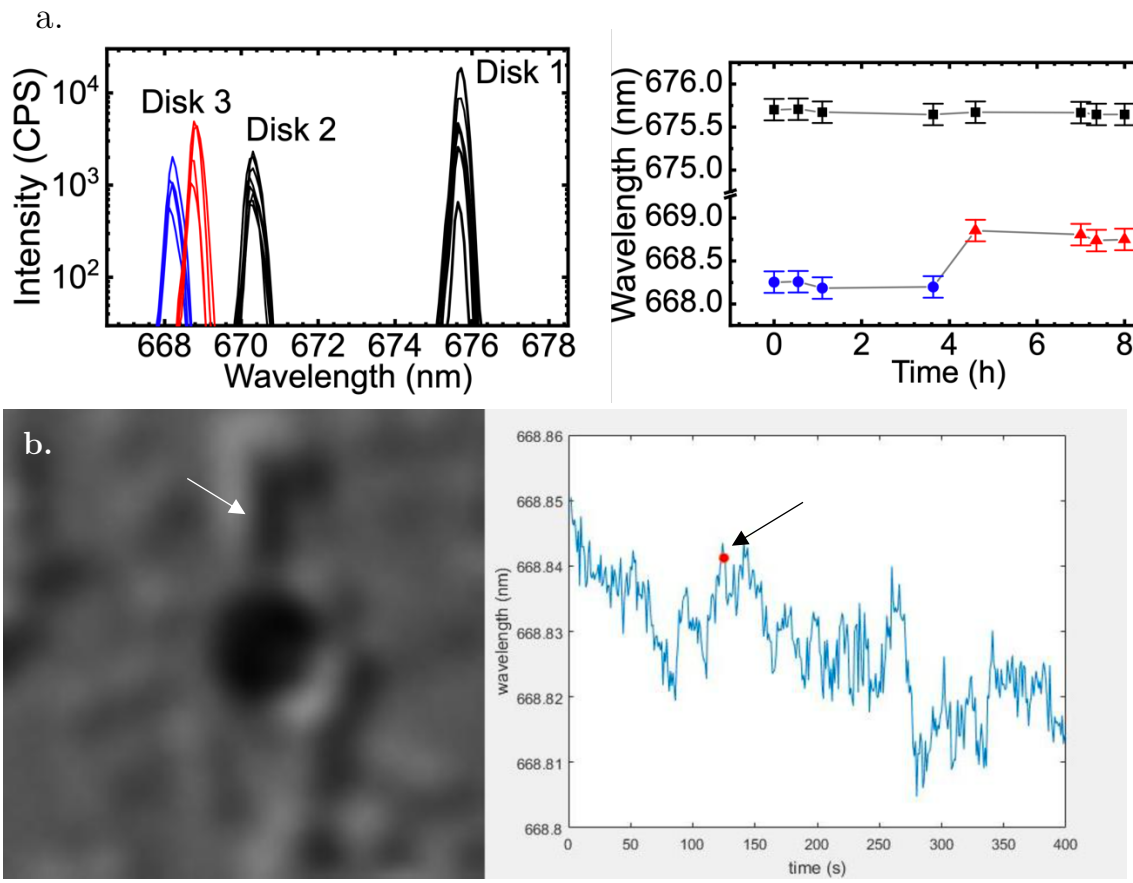

Figure 5.12. a) Wavelength scan over 8 hours of 2 internalised disks (black) and a disk before (blue) and after internalisation (red), adapted from [55]. *The wavelength shift is 0.6nm corresponding to an approximately 15nm/RIU shift, consistent with modelling in Chapter 2. b) Attempts to correlate the dynamics of near-disk dark regions with time resolved wavelength tracking, which could indicate higher density regions in brightfield (white arrow) with peaks in emission spectra (black arrow).*

The largest shift expected in the context of intracellular lasing is the change in local refractive index upon uptake of the resonator, a similar shift to that of IPA and DI water briefly characterised in Chapter 4. However, continuous monitoring of a disk during cellular uptake proved challenging, as the disk would move substantially which was difficult to follow. It could then not be confirmed that what was seen was a wavelength shift or was perhaps a different disk without fixing the sample and interrogating the structure at the level of resolution that the confocal microscope provides. However, the optical barcoding experiment proved useful here. Tracking an individual cell with 2 already internalised nanolasers approaching a 3rd over 8 hours showed a substantial change when the nanolaser was absorbed (Figure 5.12 a). This relative shift allowed for a quantification of refractive index sensitivity to 15 nm / RIU (depending on the current refractive index of the cell culture medium), much closer to the expected values from modelling in Chapter 2. After uptake, the disk did initially fluctuate more than the two already internalised disks, possibly reflecting a dynamic reflection of the refractive index upon uptake, but the wavelength stabilised over the last hour of the experiment.

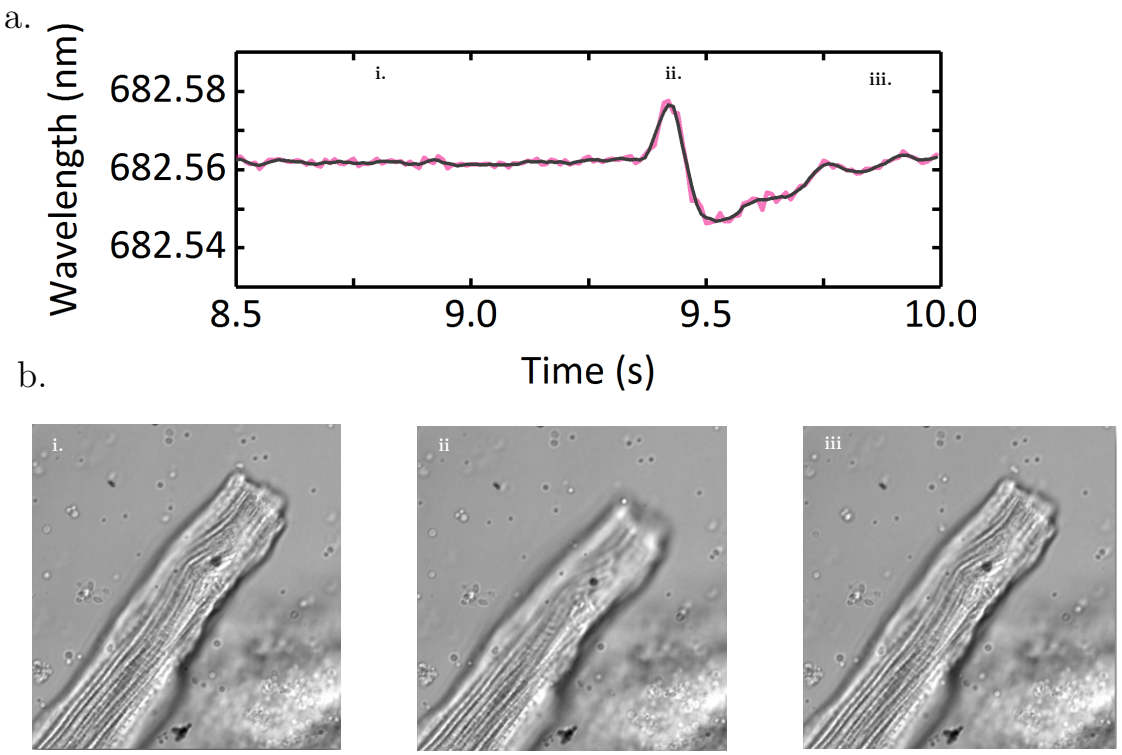

Figure 5.13 Adult Cardiomyocyte contraction resolved by shift in wavelength, showing a clear increase in wavelength (a ii.) that correlates with the cell contraction (b ii.). As before, it is important to try and find a cell that can beat and not substantially shift the resonator outside of the collection slit. Adaptions to the collection method would allow for more versatile measurements for more motile disks.

Once internalised, attempts were made to continuously excite and observe cell lasing with simultaneous imaging, with efforts to try and correlate the local change in brightness with a change in wavelength output (Figure 5.12 b). This was not initially successful due to the very small wavelength shifts, however, but developments in the process, including switching from highly motile macrophages to cardiomyocytes and utilising fluorescent probes to characterise changes to the local environment as opposed to simple changes to the DIC image, led to more success in correlating the change in wavelength to a change in environment (Figure 5.13). These shifts indicated that the disks are highly sensitive to the environment and can be used alongside the previously demonstrated polymer microspheres [166].

Finally, the project investigated neurons and neuronal activity. This is an area of ongoing research. Disks near or on top of the axons that neurons connect to each other were investigated under 1kHz excitation to attempt to correlate any potential wavelength shift to neuronal 'spiking' where the neuron uses a flow of ions to induce a change in membrane potential. This is also modelled using modified spiking HEK cells, as neurons are a highly sensitive cell line that requires great care, and a more robust analogue can be used to model the same environment before focusing on the effects of neuronal spiking. So far, although internalisation has been successful, it has not been possible to correlate spiking with a change in wavelength.

Using the disks as sensors within cells is a highly promising area for further research, as the lack of necessity for thick, biocompatible coatings allows for full exploitation of this effect. Functionalisation of the disks remains a key focus, as controlling where the disks are close to will significantly improve their usefulness as an intracellular sensor. Although many of the antigens have been formulated to attach to silica and polymer structures, work is required to develop their compatibility with the nanolasers, with preliminary success with simple fluorescent-tagged biotin coatings adhering well to disks on wafer, then detached using the acid-free disk release techniques. Other approaches, such as phospholipid bilayers like those around cells, have been used by others to functionalise whispering gallery mode sensors on-chip [76]. Once accomplished, large numbers of cells could be monitored by using a combination of multiplet barcodes and sensing to build a more complete picture of the internal workings of the cell.

5.6.5 Contributions

In this section I was principally responsible for preparing lasing samples for investigation, seeding the cells and investigating stability in cells, tracking uptake events, confirming cell internalisation and acquiring data from the membrane experiment.
Dr Marcel Schubert assisted with early confocal methods adapted from previous work, macrophage culturing and adaption of the microscope, and utilised the disks to investigate the cardiomyocytes, as well as developing a process for injection of disks with micromanipulators.
Dr Soraya Ciaxiero assisted in sensing experiments as well as furthering experiments with neurons and modified HEK cells. Andrew Morton was responsible with neuron culturing. Dr Dinesh Kumar (Post-docs, Professor Gather's Lab) assisted by culturing NIH-3T3 cells for use in membrane transit GFP expression and assistance troubleshooting membrane tracking experiment.
Simon Powis and Fiona Cooke (Collaborators, School of Medicine) were responsible for the culturing of primary cells (human T cells, macrophages, dendrocytes.)

Transferable Photonic Platform

This section will discuss the use of the III-V material as a general laser platform. The advantages of the laser discussed in earlier chapters combined with a controlled, tailored substrate provides a powerful investigative tool. This section will discuss the successful methods used to transfer the laser onto a membrane, and then attempts to characterise this platform and apply it to sensing optical enhancement on ENZ metamaterials. Finally, it will discuss applying these techniques to transfer random network structures onto a similar membrane.

5.7 Introduction

Transferring the lasers onto a membrane would provide versatility for other photonic platforms, e.g. as re-usable sensors for biophotonic applications. The concept arose naturally from the development of the release procedure discussed in Chapter 3, where initially the membrane was to be dissolved to release the disks. In the process, multiple avenues have been developed to controllably fix the disks onto a membrane. This would have numerous advantages, including the creation of nearby perturbation structures to influence and understand near field effects of the whispering gallery mode, and creating a periodic array of a known diameter of disks detached from substrate for more accurate experimental data to confirm the models in Chapter 2, a more reliable method of sensing the changes in refractive index by using multiple disks as a 2d sensor similar to other biophotonics platforms, see e.g. ERISM [174], neuron nanoneedle [3]), but also as a general transferable photonic sensing platform.

5.7.1 Nanolaser Membrane Fabrication

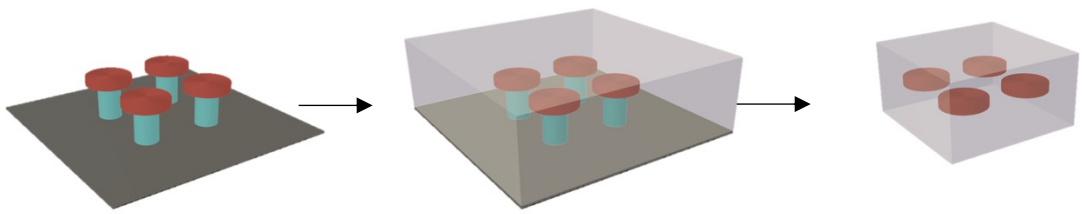

Figure 0.1 Further fabrication process to detach nanodisks getting released from membrane. The final stage was attempted both by epitaxial removal using under-etching of the substrate, and by physical removal.

By preparing the disks on pillars as described in Chapter 3, initial development simply used SU8, PMMA resists to recoat and produce polymer disks that could be epitaxially removed to form polymer encapsulated 'multiplets' of several disks, illustrated in Figure 0.1. The size of these final multiplets could be adjusted from 10 μm caps, to 5 mm sized membranes using standard photolithography techniques.

This membrane lift-off process first then explored with using SiO_2 analogues of the wafer material. This involved using a concentrated 48% HF etch. A re-coating of SU8 was used to explore the potentially advantageous property of HF mask diffusion a known effect that polymer masks do not effectively mask HF etches. Due to changes in the polymer

membrane sizes, e.g. from swelling, the disks were not well adhered and would regularly be released from the membrane. For larger macroscopic structures, the SU8/PMMA resists had additional drawbacks, they were quite fragile, and had low level fluorescence. As an alternative the elastomer polydimethylsiloxane (PDMS) was investigated, as the elastomer is flexible, strong, was not optically active in the sense that it was not fluorescent and did not seem to impede the laser wavelength, and it is easier to manipulate. Post-processing of this structure after successful disk transfer was challenging, as reducing the thickness after PDMS has crosslinked requires an RIE etch process.

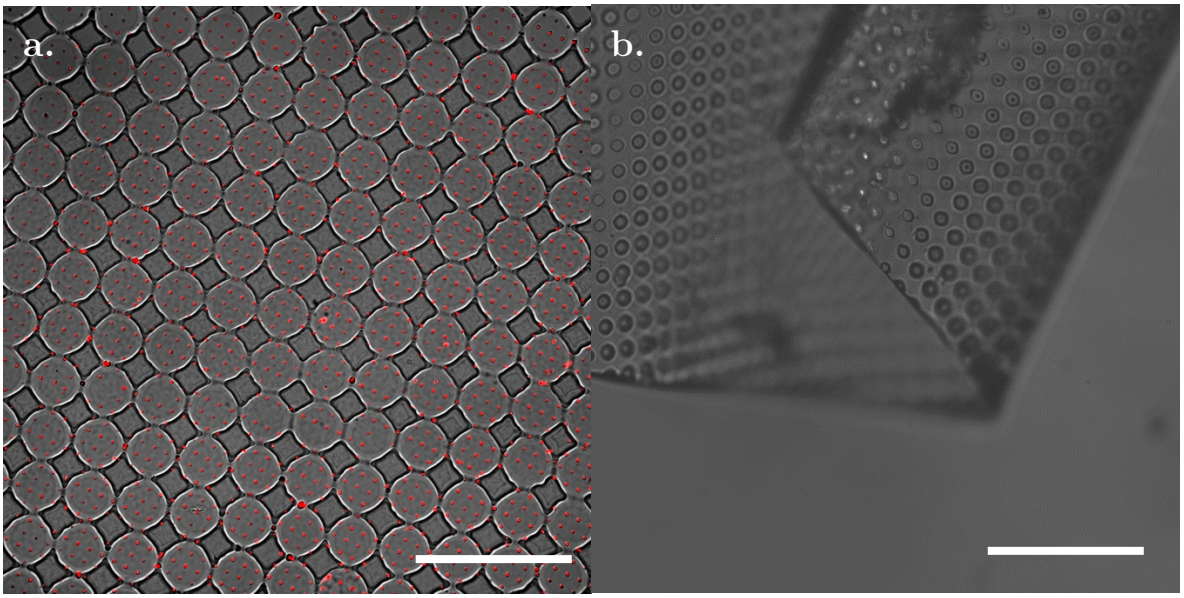

Figure 0.2. a) Nanodisk (red) embedded into SU8 connected platelets (grey) after GaAs substrate release etch. b) PDMS detachments using a disk-on-pillar structure, crosslinking the PDMS around the wafer and manually separating the disks from wafer. Scale bar 50μm.

In the first approach polymer SU8 was spin coated on a prepared disk on pillar structure, to provide purchase around the disks once transfer was successful. SU8 caps were initially prepared as detached, encapsulated multiplet structure but attempts to extend this to a membrane of macroscopic size were not successful. This appeared to be a consequence of the desirable property of SU8 as a strong adhesive agent: it adhered very well to the surface of the wafer such that fractures occur within the SU8 coating when manually delaminated rather than releasing at the substrate / SU8 interface. Following this, subsequent trials used the SU8 added pores to the membrane (Figure 0.2 a), an epitaxial release etch lift-off process. To release this interconnected grid membrane from the substrate, the membrane was exposed to citric acid, briefly described in Chapter 3, selective for the GaAs substrate until the disks were released. This etch process was

endothermic, so required continuous heating, however the etch rate (~500 nm/min) was likely limited by diffusion processes and required up to 20 minutes for the SU8 caps to be sufficiently underetched to release the disks. Once there was significant underetching, the structure was manually delaminated using water soluble tape. Despite the large number of fluorescent objects in the grid structure (Figure 6.2 a) there was only sporadic lasing disks (~10 of several hundred tested). It was concluded that the exposure to the citric acid for such long time periods damaged the disks. It was apparent that the disks were now no longer regular circles under higher magnifications, and although the fluorescence was still bright, this did not seem to correlate with lasing. The resulting membrane structure was easy to manipulate, but due to the interconnecting grid and cap morphology, made imaging through the membrane was prohibitively challenging. Due to the low yield and imaging issues, alternative processes were investigated.

The elastomer PDMS was investigated for its desirable flexibility and strength. Detachments of disks using HF onto PDMS were initially accomplished with some success, but potentially introduced etch products as contaminants. Instead, the elastomer was crosslinked on disk-on-pillar sample like the SU8 sample and was similarly manually delaminated, removing the disks from wafer without further under etching. This resulted in very thin, optically clear and manipulatable membranes of disks (Figure 0.2 b). This process was favoured for future experiments but presented issues in post-processing.

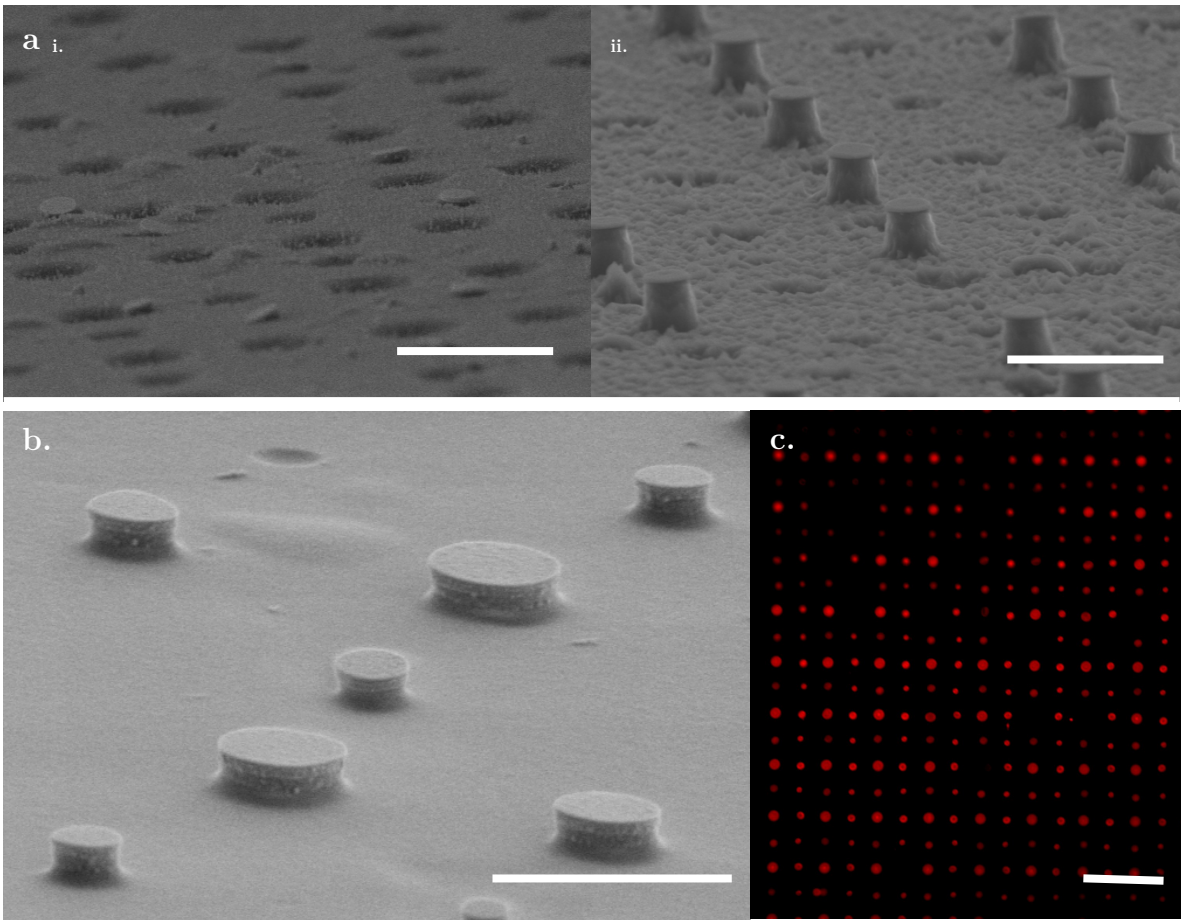

Figure 0.3. a) PDMS etch using low power (not sufficient to etch through etch stop layers) and high power (results in damage to disks). Scale bar 5μm. b) Disks on PDMS with optimised RIE and PDMS removal protocol. Capable of holding a range of different disk sizes. c) disk fluorescence of PDMS embedded disks in grid formation.

Once crosslinked, PDMS is very challenging to remove, with only few suitable solvents and acids that are able to evenly remove the material. For this, an RIE process based on a gas blend of 25 O2:100 SF_6 at 20W for 2 minutes was selected. SF_6 was able to etch through the silica containing layers, and O_2 to remove the CF_3 etch stop layers that would form. Figure 0.3 a indicates some early attempts, showing an insufficiently etched sample, with the pits the disks leave when within the PDMS (i), and an overetched sample, with disks on pillars of PDMS (ii), though exposure to the RIE has resulted in damage to the disk. Optimising for power and flow rate, the disks could be prepared just on the surface of the PDMS (Figure 6.3 b), but still well attached to be transferred from sample to sample. Refinements to this process resulted in very high yields of >95% with very few disks on the wafer remaining, with no discernible loss in lasing capability (fluorescence and profiles in Figure 6.3 c). The process also was able to remove disks that were freestanding on the substrate rather than on pillar, some of which are visible in Figure 0.3 a.i.

5.8 ENZ Platform

Artificial media with extreme optical properties, such epsilon-near-zero (ENZ) metamaterials, provide an attractive investigation target. These metamaterials are actively researched and have a multitude of different potential applications for optical technologies, such as subwavelength imaging or advanced photonic circuits. ENZ can be realised by operating materials close to the plasma frequency e.g, for transparent conductive oxides in the near infra-red [177]. Alternatively, it can be achieved by creating a composite material, produced by stacking metallic material of negative permittivity, and dielectrics of positive permittivity, such that the effective permittivity is sums to zero at a particular resonant wavelength. By adjusting the subwavelength thickness of each layer this resonance can be tuned. [178], [179].

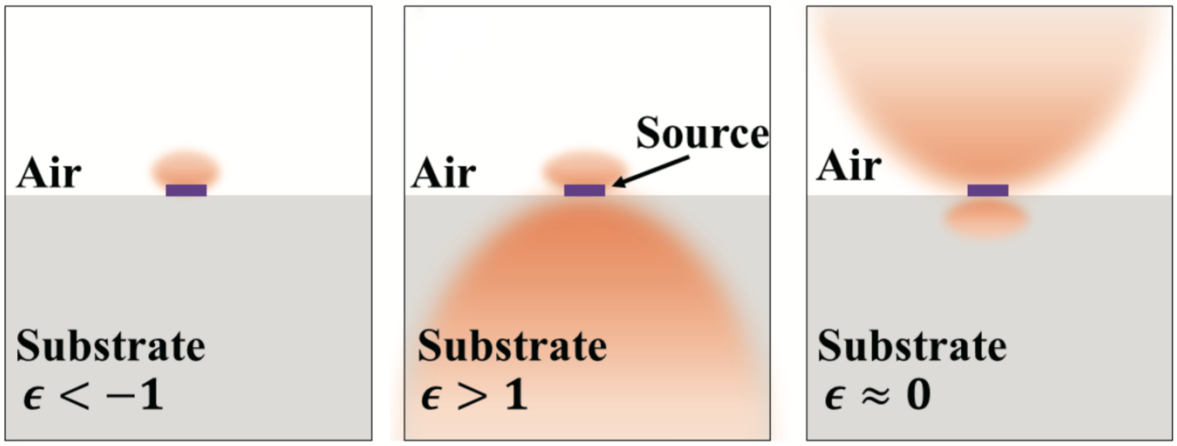

Figure 0.4 A schematic illustration comparing the behaviour of a light emitting source on substrates of varying permittivity, where metallic substrates have ε < -1, dielectrics ε>1. The material of interest to this subsection uses a combination of these materials to have a combined $\varepsilon \approx 0$ and are therefore named epsilon near zero materials. The light emitted by the source is represented in orange. Reproduced from [180].

In this work we wish to investigate the interaction of the ENZ condition and the behaviour of the light outcoupling from the nanolaser. As discussed, the refractive index contrast defines the mode profile of the laser and the evanescent component of the resonant mode. The ENZ surface, with its novel property, could enhance the output intensity of the disk by forcing the emitted light into the more optically dense medium, in this case, air [181]. This is conceptually illustrated in Figure 0.4. For dielectric and metallic substrates, light is either scattered into more the more optically dense substrates or decays rapidly due to high conductivity respectively [182]. For the nanolasers

discussed the majority of the outcoupled energy being directed in the shortest possible optical path, defined by the effective refractive index n_{eff}. However, the ENZ condition results in a sub-unitary refractive index for resonant wavelengths and can therefore exhibit much longer effective optical path lengths than any naturally occurring material, resulting in significant emission enhancement [25].

5.8.1 ENZ Substrates

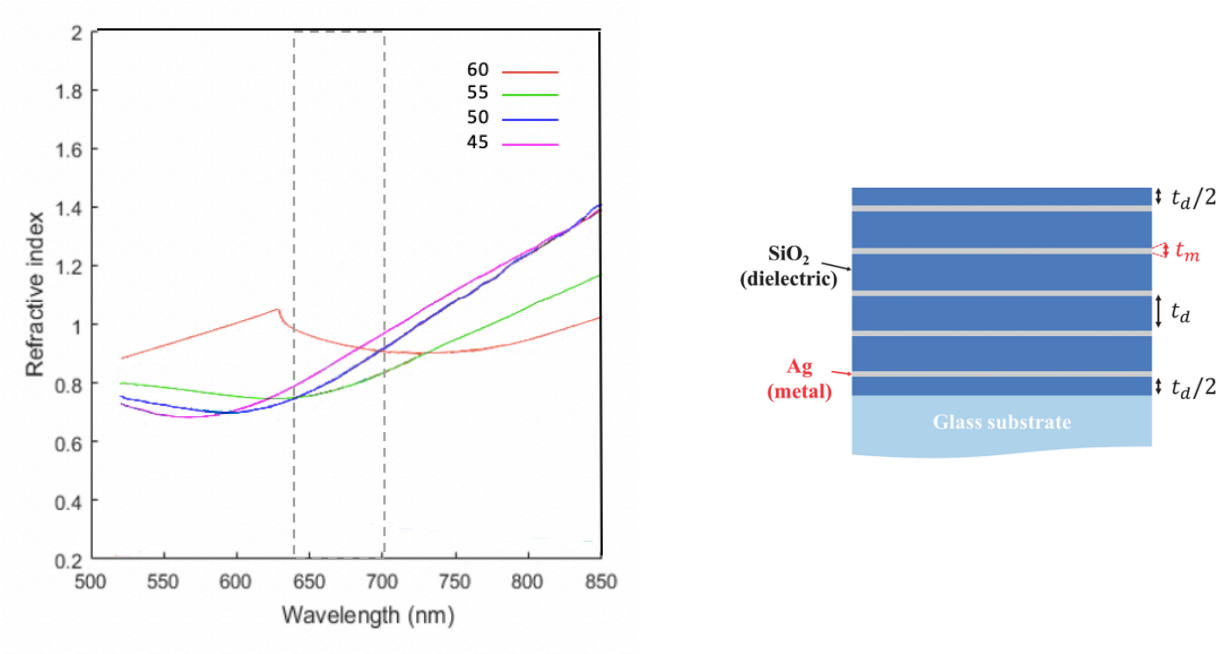

Figure 0.5 Investigated ENZ samples and their absolute refractive index (determined by modelled real and imaginary permittivity), with dotted lines to indicate the gain region the disks emit in for reference. The sample numbers indicate the thickness (nm) of the SiO_2 dielectric component of the bilayer (t_d).

The ENZ metamaterials tested here were produced by Xin Li [180] by e-beam evaporation (Figure 6.5). They consist of a 5-bilayer structure of 6nm silver (Ag) and SiO_2. The resonance condition was tuned by adjusting the thickness of the SiO_2 dielectric layers to 45, 50, 55, 60nm, which corresponds to the ENZ condition at 583 nm, 602 nm, 610 nm and 730 nm, resulting in a minimum refractive index at 570 nm, 621 nm, 645 nm and 742 nm. The thickness of the SiO_2 layers is used to refer to the individual samples.

5.8.2 WGM Experiments

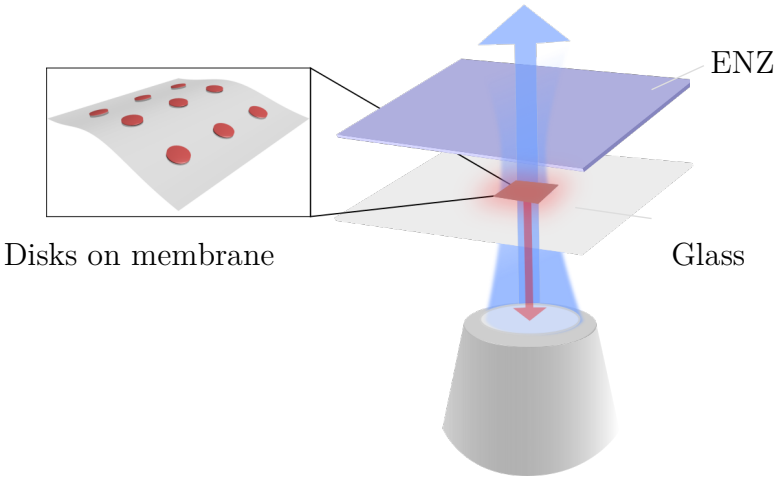

Figure 0.6, schematic of the tests for ENZ. The glass membrane support served two purposes, easy imaging and lasing of the nanolasers (red, left inset) through optically clear medium and allowing for the use of oil immersion objectives. The top layer (purple) represents the ENZ testing surface and could be easily exchanged.

To fully investigate the optical enhancement effects of the ENZ, it must be within the evanescent field of the whispering gallery mode. This required some effort to reduce the separation between the disk membrane and ENZ substrate as much as possible. To achieve this the membrane surface, its glass coverslip scaffold and ENZ test surface were cleaned as effectively as possible, and brought into contact using DI water to try and hold the two surfaces together with capillary action whilst keeping good optical uniformity in the cavity and facilitating the exchange of the ENZ substrate once the experiment was completed (Figure 6.6).

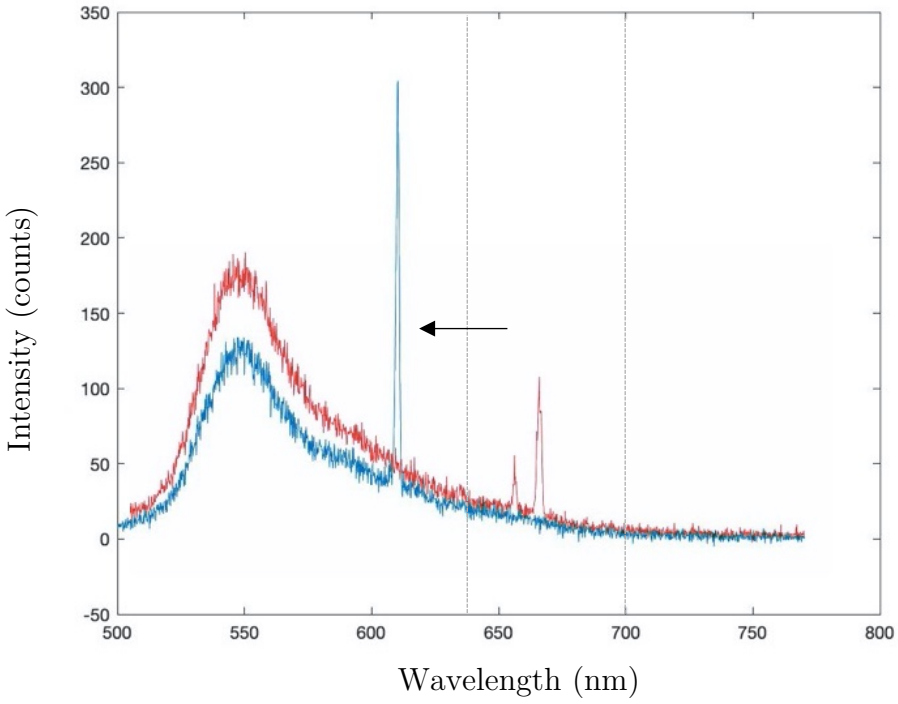

Figure 0.7 Representative example of 2 disks in SU8 membrane platelet on glass emitting wavelengths (red) in expected gain region (orange). Same area excited on ENZ (blue) showing a sharp, more intense peak in an area that does not usually have sufficient gain to support a lasing mode. Initial configuration resulted in a loss in pump power (SU8 fluorescence peak drop in intensity) as the excitation was through the ENZ.

Initial responses utilising the few SU8 disks on the grid membrane (Figure 6.1 a) showed a surprising shift in wavelength of the few remaining disks to 600-630 nm for which the origin is currently unknown and a subject of ongoing investigation (Figure 6.7). The expected response was the potential increase in intensity through optical enhancement. To test this membrane, the configuration in Figure 6.6 was inverted - the membrane to be placed onto a test substrate, which resulted in a decrease in pump fluence due to optical absorption of the ENZ. This causes the decrease in florescence output in Figure 6.7, but the more intense lasing peak could indicate ENZ enhancement. However, as discussed earlier, the disks were largely compromised by the transfer process.

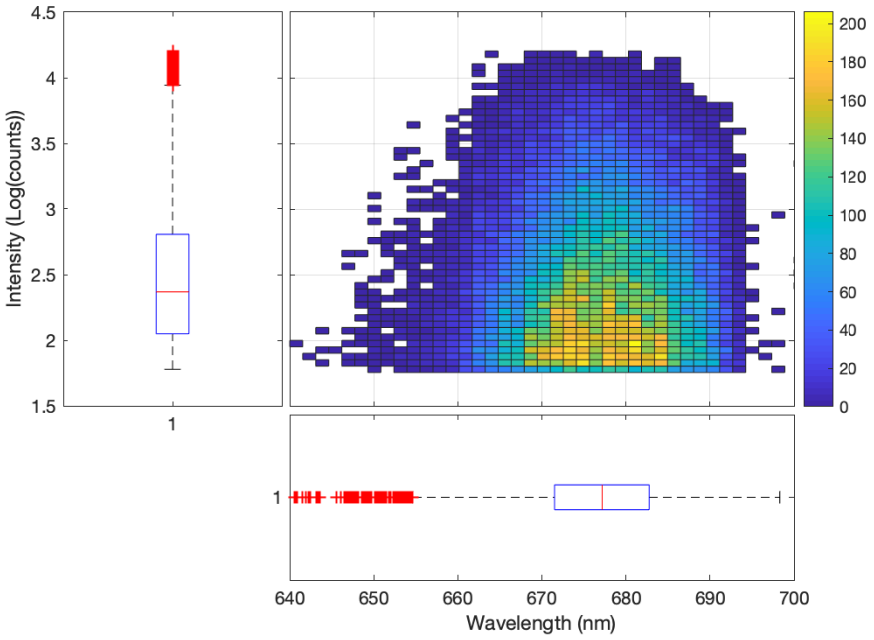

Figure 0.8 Peaks from at least 5000 disks on PDMS over repeated scans, with number of occurrences as a heatmap for a histogram of peak intensity log(counts) and the wavelength (nm). The box plots are interpretations statistical data from each axis. Red crosses are outliers.

In the PDMS configuration of membrane in Figure 6.3 b, disks were very densely packed, it was difficult to precisely locate the same disk. Marking the PDMS after fabrication was avoided due to potential bubbling which would affect the separation distance between nearby disks and the ENZ, which was a higher priority. Therefore, we used a statistical approach where the same membrane region was scanned several times, using distinctive edge patterns. The process was successful, and further samples were put into development with marked waypoints so that smaller collections of disks could be used and uniquely identified from images. The area measured approximately 2500 μm and 100 μm, where the automated stage would raster scan with the same pump fluence (100 $\mu J/mm^2$) and exposure time (0.1s). The region analysed contained a good spread of emission wavelengths for investigation (Figure 6.8), where the intensity of the peaks could be statistically compared to a control scan. Shifts like those detected in Figure 6.7 were not reproducible in this configuration. The differences in the two samples were the SU8 material and the lack of glass scaffold. The material may have had some interaction with the disks, but it is more likely that the PDMS membrane and glass scaffold structure provided insufficient proximity to the ENZ test surface.

To investigate the optical enhancement effect of the ENZ and the disk, PDMS 1:10 was spin coated onto a #**0** (85 - 115 µm) thick glass slide, with an estimated thickness of <5µm. A prepared disk on pillar configuration was inset into the PDMS and then was crosslinked. Once this prepared sample was investigated under SEM (Figure 6.2 b) the sample was exposed to the ENZ, as well as two controls, a glass coverslip of similar thickness, and a silver mirror, to control for both dielectric and reflective effects of the sample.

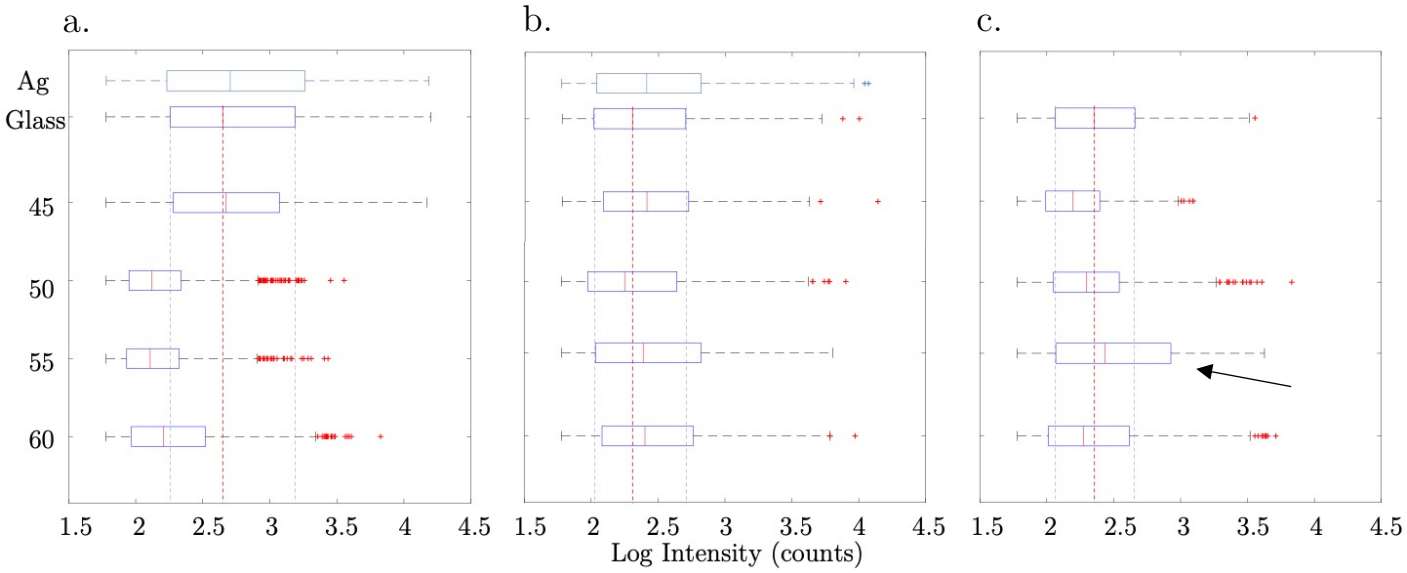

Figure 0.9. Change in peak intensity distribution of 5000 disks in setup. a) Initial testing of disks freshly prepared as in Figure 6.2b were exposed to glass, then the ENZ, then finally the metallic silver (grey) secondary control to ensure any shifts were not due to disk photodegradation. Annotated area extends the results of the glass control for reference. b) Experiment repeated after further PDMS reduction, which should have reduced the separation to the ENZ surface. c) Further removal of PDMS appears to have degraded disk intensity significantly. Red crosses are outliers. Arrow indicates possible ENZ enhancement over control.

The results of this experiment are depicted in Figure 6.9 a. The silver mirror and glass box plots show a spread of intensity as a box plot and are used as controls, where the box plots are extracted from the distribution of peaks for each test substrate as shown in Figure 6.8. There is no significant difference between the controls, however most ENZ samples show a marked decrease in laser excitation. The silver mirror control tests were performed after all other ENZ test to remove the possibility that the decrease in intensity were due to photodamage to the disks during the scanning process, so the effect must be some sort of suppression of the mode. It's this suppressive effect that might explain the shift in wavelength in Figure 6.7, instead permitting another mode in a less favourable part of the gain to lase. However, there was no wavelength shift detected (all

wavelengths for all test substrates were not statistically different). In order to try to reduce the separation distance, the glass cover slip that held the membrane was exposed to a high intensity RIE such as that used on Figure 6.2 b to remove any PDMS that may have been obstructing the decrease in separation. The disk area was protected by a silicon hard mask to prevent exposure to the RIE process. The result, described in Figure 6.9 b shows that with the potentially decreased separation all the intensities distributions do not show any significant change from each other, though it shows a relative increase of the ENZ substrate laser intensities over the previous scan, the emission of the controls in particular is significantly lowered after the RIE treatment. Further reduction of the membrane was attempted (Figure 6.9 c) which compounds the decrease, despite the hard mask substantial reduction in the control nanolaser sample is apparent. Figure 6.9 c, should now represent the sample of closest separation have been roughly in contact, separated by the water only, (which, despite holding the samples closer than otherwise possible, is likely still a separation greater than 300 nm which is the extent of evanescent field of the nanolaser). This sample does not have a silver control due to degradation of the metal after repeated experiments. Nonetheless, if compared to the latest control scan, sample 55 – which has a refractive index minimum of 645 nm or just within the gain region of the nanolasers, appears to show possibly significant optical enhancement. The degradation of disk performance over days was mirrored by a degradation of ENZ multilayer. This did not appear to be a DI water effect, as a PDMS dummy and ENZ were stored in water for several days with no similar effect. The PDMS with disks appeared to be slightly acidic with litmus test, which could be a result of reaction products of the RIE post-processing of the PDMS. The hypothesis is that hydrolysis of C-F_3 etch stop layer could result in aqueous fluorine / flouroform [183] which could potentially disrupt both the SiO_2 and disk structure. With refinements to the disk fabrication process tests are planned to control the separation with a pre-grown SiO_2 layer and free floating detached disks, which could then be transferred and released onto another surface, though this removes the potential for position information, this could be accomplished with a relatively small subset of disks and multiplexing the peaks using statistical numbers as before. This would both remove the potential damage to the disks induced by the RIE and its potential reaction products.

5.9 Random Network Structure

The described processes used to detach the disks could be applied to the partially or completely underetched random network structures, discussed in Chapter 3. Particularly

the PDMS lift-off showed great promise, as it did not rely on additional etch steps that could damage the delicate structure, and could remove free standing structures attached to the wafer after complete underetching.

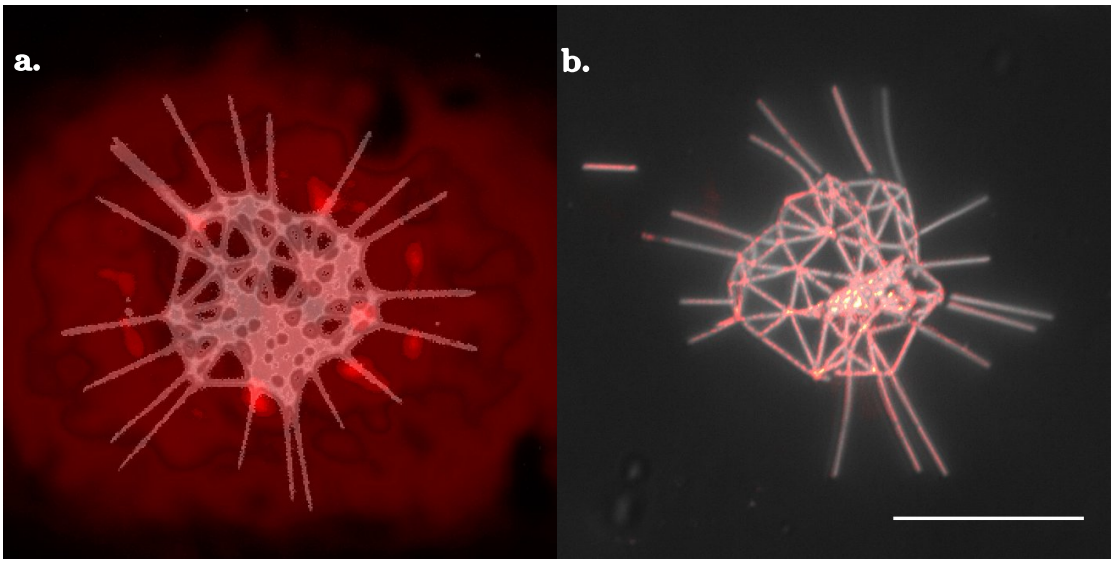

Figure 0.10 a) brightfield network on wafer with partial under etching (white) with fluorescence pattern under laser excitation (red), adapted from data courtesy of: Complex Nanophotonic Groups ICL b) brightfield Network detached onto PDMS (white) and laser fluorescence (red) scale for both 50μm.

The results of a partially under etched random network can be compared to a PDMS embedded structure (Figure 6.10). Most of the structure has been successfully detached, and exhibits fluorescence is clearly more localised to the nodes, a significant improvement of the relatively homogenous fluorescence profile of the wafer attached structure. However, the PDMS appears to have been sufficiently flexible that the structure has undergone some damage, which is likely due to the flexibility of the PDMS. To reduce the flexibility, the ratio of crosslinking agent could be increased to make a stiffer elastomer, which may preserve the random network structure more effectively.

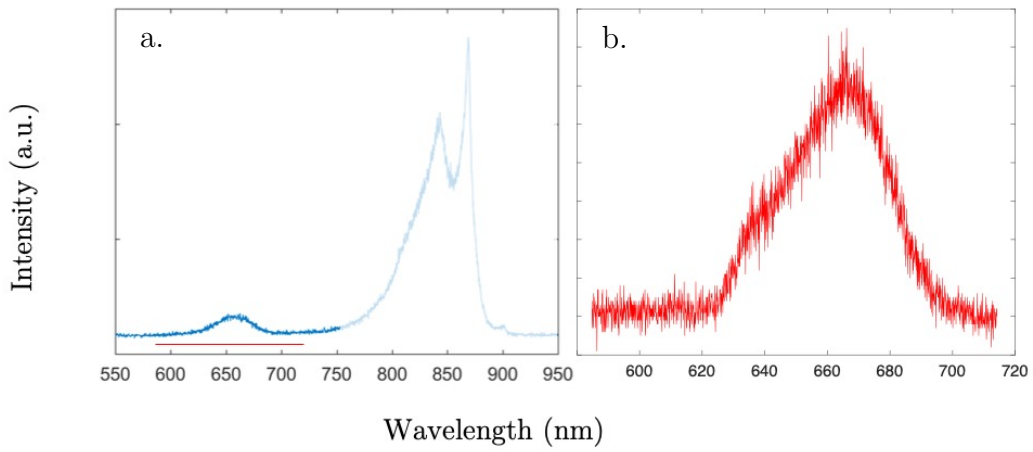

Figure 0.11 Spectrum collected under excitation for Figure 6.10. a) Shows fluorescence of network on wafer. The peak at 850 nm is due to fluorescence from the GaAs wafer substrate. Red line highlights the region analysed for the detached random networks. Adapted from data courtesy of: Complex Nanophotonic Groups b) Shows the output of laser excited fluorescence of the detached random network on PDMS.

However, the localisation of the fluorescence does not seem substantially shifted in this case, both fluorescent peaks (Figure 6.11) are co-localised with the gain discussed in Chapter 3, and attempts to increase pump power did not produce lasing in the random network, and appear to just show bulk fluorescence properties. This is not immediately surprising, as the network requires optimisation to the fabrication process to make the structure thinner, which in turn might allow for easier lift-off. The process is relatively simple and the optical clarity of the PDMS allows for good resolution, pump fluence and longevity of the sample.

5.10 Contributions

Stefano Verme (Undergraduate student I co-supervised) assisted in early development of the membrane detachment concept
Xin Li (PhD student, Professor Di Falco's Lab) prepared the ENZ materials for analysis
Soraya Ciaxero (Post-doc, Professor Gathers lab) and collaborators Complex Nanophotonic Groups Imperial Collage London (ICL) designed the network structures, with early investigations done by ICL.
I was responsible for refining and developing the PDMS lift-off process to investigate the nanodisks and random network structures, as well as designing and optimising the setup to investigate the ENZ and acquiring and analysing the lasing data from the experiments.

Conclusion

This thesis has introduced the basic concepts, discussed the material properties and presented the theoretical basis for efficient, nano-scale visible laser emitters. It has demonstrated the controllable fabrication of high quality, sub-μm disk structures using a two-step wet etch, introducing the advantages of a dry etch process for random networks and encapsulation for long term stability. The characterisation of the whispering gallery mode nanolasers confirmed experimentally the theoretical predictions. The application the nanodisks as intracellular devices and as a transferrable photonic platform, indicated the versatility and effectiveness of these nanolasers. This section will summarise the main findings of the thesis and discuss the future direction of the project.

6.1 The Work

The motivation of this work was to fabricate a sub-μm, visible laser device with as low thresholds as possible. For this, a MQW, InGaP/AlInGaP nanodisk laser was fabricated with smooth, steep side walls. To ensure its stability in solution over planned experimental timescales a passivation process was developed. For longer, future experiments, encapsulation was explored. This method was also used to isolate the disks from the refractive index of their environments. The resulting structures demonstrated a highly efficient laser performance, with narrow linewidths indicating high Q factors, effective use of the gain medium, with very low thresholds.
In a biophotonic environment, the lasers were demonstrated to be stable over long periods of time, which was a useful feature for barcoding. They could be applied and detected in optically scattering material and confined environments, without hindering the behaviour of the cell or the performance of the disk. The thesis also discussed the use of the nanolasers as a sensor for refractive index changes within the cell.
Additionally, this thesis presented the preliminary results of ongoing work, aimed at transferring the disks to a flexible membrane, and using the properties of the whispering gallery mode to investigate the enhancement properties of ENZ media. Finally, work to utilise the wafer material to construct a random network to investigate the properties of random scattering lasers was explored, and the partial transfer of a test structure onto a membrane was demonstrated.

6.2 Outlook

Now that the fabrication and characterisation of the disks has almost reached a mature stage with high yields, high performance and good reproducibility, the focus on the project falls on future applications. The applications illustrated in this project provide an excellent proof of concept reproductions of previous experiments, however, the nanolasers could provide novel insights into the platforms they are applied to.

6.2.1 Further Biophotonic Application

Current ongoing work focuses on the sensing capability of the disks. Preliminary experiments on cardiomyocyte and neurons is likely to produce results in the coming months.
The nanolasers small size has been demonstrated to be internalised by some of the smallest cell types and in environments with restricted geometries of the membrane. The natural step forward is to label and track cells around an in-vivo sample, to determine the nature of tumour metastases and immune system activation. This necessitates that the nanolasers be targeted toward a specific cell type. Current developments in using micromanipulators to inject the disks where required are being developed, as well as making bio-functionalised coatings such that the disks can selectively tag and sense pre-determined conditions.
Finally, combining this cell specific, unambiguous tracking even through highly complicated, in-vivo environments, could be combined with cell sorting procedures, allowing for single cell genomics applications, a potentially transformative advancement for bioanalysis.

6.2.2 Random Network Lasers

Optimisation to the fabrication process to produce the random network lasers is nearing maturity. Once realised, the production and investigation of pre-determined and reproducible 'random' structures could be used to understand the processes and output of a random scattering laser. The delicate structure presents a challenge for fabrication, but the application of a flowable oxide HSQ resist, ICP chemical-assisted dry etching techniques should provide the selectivity and surface properties necessary, where then the procedure for transferring the networks can be applied.

6.2.3 Transferable Photonic Platform

Though detaching the disks onto a membrane provided potentially encouraging results, decreasing the separation distance between the substrate and the nanodisk to within the evanescent field of the WGM will likely rely on injected disks on a pre-determined silica coating of desired thickness. The disks could then be removed and released using the lift off techniques developed. The PDMS membrane, combined with the optimisation of the random network structure fabrication, could be used to produce highly specific laser

sizes to better characterise the disks mode behaviour and sensing capability. Finally, the development of a large 2D array of lasers that are capable of sensing changes to the environment has considerable application as a general refractive index sensor.

6.3 Impact

All considered, the nanolaser devices have been shown to be a highly versatile, novel structure. The bio-optimised nanostructure that can act as a highly characterisable barcode or refractive index sensor, but also for applications both as a general platform to investigate photonic structures such as ENZ metamaterials and random lasers. The promise that using these highly capable devices to investigate biological phenomena could yield transformative understanding of single cell behaviour and genetic correlations is a powerful motivator for further study. Optimisations for the material for far-red / near IR emission, functionalisation of the surface to target specific cells or sense particular molecules is a matter of ongoing research, whilst integration with cell sorting is being developed.

Compared to the state of the art, these laser devices exhibit highly attractive properties, with some of the lowest thresholds and smallest sizes for a visible laser emitter. The resilience of the nanolasers to solvents, transfer and sustained operation make them a versatile photonic tool.

The primary goal of this thesis aimed to produce and demonstrate a nanoscale whispering gallery mode laser tag and sensor. This goal has been achieved in full, but it only briefly explores their full potential for future research applications into photonics and biology.

Bibliography

[1] M. S. Zubairy, "A Very Brief History of Light," in *Optics in Our Time*, M. D. Al-Amri, M. El-Gomati, and M. S. Zubairy, Eds. Cham: Springer International Publishing, 2016, pp. 3–24.

[2] A. J. Gross and T. R. W. Herrmann, "History of lasers," *World J. Urol.*, vol. 25, no. 3, pp. 217–220, Jun. 2007.

[3] A. Baranov and E. Tournié, *Semiconductor lasers: Fundamentals and applications*. 2013.

[4] R. M. Ma and R. F. Oulton, "Applications of nanolasers," *Nature Nanotechnology*. 2019.

[5] D. S. Wiersma, "The physics and applications of random lasers," *Nat. Phys.*, vol. 4, no. 5, pp. 359–367, 2008.

[6] C.-Z. Ning, "Semiconductor nanolasers and the size-energy-efficiency challenge: a review," *Adv. Photonics*, vol. 1, no. 01, p. 1, 2019.

[7] T. H. Maiman, "Stimulated optical radiation in Ruby," *Nature*, 1960.

[8] H. Hora, S. Eliezer, G. H. Miley, J. Wang, Y. Xu, and N. Nissim, "Extreme laser pulses for non-thermal fusion ignition of hydrogen-boron for clean and low-cost energy," *Laser Part. Beams*, 2018.

[9] L. He, Ş. K. Özdemir, and L. Yang, "Whispering gallery microcavity lasers," *Laser Photonics Rev.*, vol. 7, no. 1, pp. 60–82, 2013.

[10] E. Kim, M. D. Baaske, and F. Vollmer, "Towards next-generation label-free biosensors: recent advances in whispering gallery mode sensors," *Lab Chip*, 2017.

[11] M. C. Gather and S. H. Yun, "Single-cell biological lasers," *Nat. Photonics*, 2011.

[12] S. Nizamoglu *et al.*, "A Simple Approach to Biological Single-Cell Lasers Via Intracellular Dyes," *Adv. Opt. Mater.*, vol. 3, no. 9, 2015.

[13] M. Schubert *et al.*, "Lasing within Live Cells Containing Intracellular Optical Microresonators for Barcode-Type Cell Tagging and Tracking," *Nano Lett.*, vol. 15, no. 8, pp. 5647–5652, 2015.

[14] D. J. Bergman and M. I. Stockman, "Surface Plasmon Amplification by Stimulated Emission of Radiation: Quantum Generation of Coherent Surface Plasmons in Nanosystems," *Phys. Rev. Lett.*, 2003.

[15] E. I. Galanzha *et al.*, "Spaser as a biological probe," *Nat. Commun.*, vol. 8, 2017.

[16] G. C. Righini and S. Soria, "Biosensing by WGM microspherical resonators," *Sensors (Switzerland)*, vol. 16, no. 6. 2016.

[17] C. Zeng, A. Gonzalez-Alvarez, E. Orenstein, J. A. Field, F. Shadman, and R. Sierra-Alvarez, "Ecotoxicity assessment of ionic As(III), As(V), In(III) and Ga(III) species potentially released from novel III-V semiconductor materials,"

Ecotoxicol. Environ. Saf., 2017.

[18] M. T. Hill and M. C. Gather, "Advances in small lasers," *Nat. Photonics*, vol. 8, no. 12, 2014.

[19] R. Horstmeyer, H. Ruan, and C. Yang, "Guidestar-assisted wavefront-shaping methods for focusing light into biological tissue," *Nat. Photonics*, 2015.

[20] A. Y. Kobitski *et al.*, "An ensemble-averaged, cell density-based digital model of zebrafish embryo development derived from light-sheet microscopy data with single-cell resolution," *Sci. Rep.*, 2015.

[21] M. Gaio, D. Saxena, J. Bertolotti, D. Pisignano, A. Camposeo, and R. Sapienza, "A nanophotonic laser on a graph," *Nat. Commun.*, 2019.

[22] S. Rotter, "Network lasers," *Nature Photonics*. 2019.

[23] Q. Lu, X. Chen, L. Fu, S. Xie, and X. Wu, "On-chip real-time chemical sensors based on water-immersion-objective pumped whispering-gallery-mode microdisk laser," *Nanomaterials*, vol. 9, no. 3, 2019.

[24] D. Dai, J. Bauters, and J. E. Bowers, "Passive technologies for future large-scale photonic integrated circuits on silicon: Polarization handling, light non-reciprocity and loss reduction," *Light: Science and Applications*. 2012.

[25] L. Caspani *et al.*, "Enhanced Nonlinear Refractive Index in ϵ -Near-Zero Materials," *Phys. Rev. Lett.*, 2016.

[26] I. D. W. Samuel, E. B. Namdas, and G. A. Turnbull, "How to recognize lasing," *Nat. Photonics*, vol. 3, no. 10, pp. 546–549, 2009.

[27] M. Karl *et al.*, "Optofluidic distributed feedback lasers with evanescent pumping: Reduced threshold and angular dispersion analysis," *Appl. Phys. Lett.*, 2016.

[28] R. P. Feynman, R. B. Leighton, and M. L. Sands, "The Origin of the Refractive index," *Feynman Lect. Phys. Vol. 1*, 1963.

[29] C. Bayo, M. Ángel, M. Ángel, and C. Bayo, "Miguel Angel Caro Bayo," 2013.

[30] M. Fox and R. Ispasoiu, "Quantum Wells, Superlattices, and Band-Gap Engineering," in *Springer Handbook of Electronic and Photonic Materials*, 2017.

[31] P. Blood, *Principles of semiconductor lasers*. Woodhead Publishing Limited, 2013.

[32] D. A. B. Miller, "Optical Physics of Quantum Wells," *Quantum Dyn. Simple Syst. Oppo, G. -L., Barnett, S. M., Riis, E., Wilkinson, M., Eds.; Inst. Phys. London*, pp. 239–266, 1996.

[33] M.-H. Zhuge *et al.*, "Wavelength-Tunable Micro/Nanolasers," *Adv. Opt. Mater.*, vol. 1900275, p. 1900275, 2019.

[34] C. Y. Liu, S. F. Yoon, W. J. Fan, J. W. R. Teo, and S. Yuan, "Low threshold current density and high characteristic temperature narrow-stripe native oxide-confined 1.3-μm InGaAsN triple quantum well lasers," *Opt. Express*, vol. 13, no. 22, p. 9045, 2005.

[35] A. J. Zilkie *et al.*, "Carrier dynamics of quantum-dot, quantum-dash, and

quantum-well semiconductor optical amplifiers operating at 1.55 μm," *IEEE J. Quantum Electron.*, 2007.

[36] F. Kano, T. Yamanaka, N. Yamamoto, H. Mawatari, Y. Tohmori, and Y. Yoshikuni, "Linewidth Enhancement Factor in InGaAsP/InP Modulation-Doped Strained Multiple-Quantum-Well Lasers," *IEEE J. Quantum Electron.*, 1994.

[37] Z. Zhang, L. Yang, V. Liu, T. Hong, K. Vahala, and A. Scherer, "Visible submicron microdisk lasers," *Appl. Phys. Lett.*, vol. 90, no. 11, pp. 2005–2008, 2007.

[38] F. Hadjaj, A. Belghachi, and A. Helmaoui, "Optical gain and confinement in Gaas/Algaas structure quantum well lasers," *Int. J. Nanoelectron. Mater.*, vol. 11, no. 1, pp. 61–70, 2018.

[39] R. Phelan *et al.*, "InGaP/AlGaInP quantum well discrete mode laser diode emitting at 689 nm," *IEEE Photonics Technol. Lett.*, 2018.

[40] M. Zafar *et al.*, "Theoretical study of structural, electronic, optical and elastic properties of Al x Ga 1−x P," *Optik (Stuttg).*, vol. 182, no. February, pp. 1176–1185, 2019.

[41] E. Ochoa-Martínez *et al.*, "Refractive indexes and extinction coefficients of n- and p-type doped GaInP, AlInP and AlGaInP for multijunction solar cells," *Sol. Energy Mater. Sol. Cells*, vol. 174, pp. 388–396, Jan. 2018.

[42] M. V. Lebedev, N. A. Kalyuzhnyy, S. A. Mintairov, W. Calvet, B. Kaiser, and W. Jaegermann, "Comparison of wet chemical treatment and Ar-ion sputtering for GaInP 2 (100) surface preparation," *Mater. Sci. Semicond. Process.*, vol. 51, pp. 81–88, Aug. 2016.

[43] G. Margaritondo, *Chapter 14 - The Role of Photoemission Spectroscopies in Heterojunction Research*, Second Edi. Elsevier B.V., 2013.

[44] M. Karl, "Living Lasers : Lasing from Biological and Biocompatible Soft Matter," no. April, 2018.

[45] M. Humar and S. Hyun Yun, "Intracellular microlasers," *Nat. Photonics*, vol. 9, no. July, 2015.

[46] H. Quan and Z. Guo, "Analytical Solution of Whispering-Gallery Modes," *ASME 2007 InterPACK Conf. Vol. 1*, pp. 489–497, 2007.

[47] Y. Zheng *et al.*, "Sensing and lasing applications of whispering gallery mode microresonators," *Opto-Electronic Adv.*, vol. 1, no. 9, pp. 18001501–18001510, 2018.

[48] H. Cao and J. Wiersig, "Dielectric microcavities: Model systems for wave chaos and non-Hermitian physics," *Rev. Mod. Phys.*, vol. 87, no. 1, pp. 61–111, 2015.

[49] G. Lin *et al.*, "Dependence of quality factor on surface roughness in crystalline whispering-gallery mode resonators," *Opt. Lett.*, vol. 43, no. 3, p. 495, 2018.

[50] M. Ornigotti and A. Aiello, "Analytical approximations of whispering gallery modes in anisotropic ellipsoidal resonators," *Phys. Res. Int.*, vol. 2014, no. 1, pp. 1–17, 2014.

[51] M. Schubert *et al.*, "Lasing in Live Mitotic and Non-Phagocytic Cells by Efficient Delivery of Microresonators," *Sci. Rep.*, vol. 7, 2017.

[52] A. B. Matsko and V. S. Ilchenko, "Optical resonators with whispering-gallery modes - Part I: Basics," *IEEE J. Sel. Top. Quantum Electron.*, 2006.

[53] M. Oxborrow, "How to simulate the whispering-gallery-modes of dielectric microresonators in FEMLAB/COMSOL - art. no. 64520J," *Laser Reson. Beam Control IX*, vol. 6452, no. 0, pp. J4520–J4520, 2007.

[54] T. Baba, M. Fujita, A. Sakai, M. Kihara, and R. Watanabe, "Lasing characteristics of GaInAsP-InP strained quantum-well microdisk injection lasers with diameter of 2-10 μm," *IEEE Photonics Technol. Lett.*, vol. 9, no. 7, pp. 878–880, 1997.

[55] A. H. Fikouras *et al.*, "Non-obstructive intracellular nanolasers," *Nat. Commun.*, vol. 9, no. 1, p. 4817, 2018.

[56] V. Duong Ta, R. Chen, L. Ma, Y. Jun Ying, and H. Dong Sun, "Whispering gallery mode microlasers and refractive index sensing based on single polymer fiber," *Laser Photon. Rev.*, vol. 7, no. 1, 2013.

[57] Y. Z. Huang, Z. Pan, and R. H. Wu, "Analysis of the optical confinement factor in semiconductor lasers," *J. Appl. Phys.*, vol. 79, no. 8, pp. 3827–3830, 1996.

[58] A. Zagajewski, "Modelling the Properties of," 2018.

[59] A. B. Matsko, A. A. Savchenkov, D. Strekalov, V. S. Ilchenko, and L. Maleki, "Review of Applications of Whispering-Gallery Mode Resonators in Photonics and Nonlinear Optics," *IPN Prog. Rep.*, vol. 42, no. 162, pp. 1–51, 2005.

[60] T. Reynolds *et al.*, "Optimization of whispering gallery resonator design for biosensing applications," *Opt. Express*, vol. 23, no. 13, 2015.

[61] N. Kryzhanovskaya *et al.*, "Enhanced light outcoupling in microdisk lasers via Si spherical nanoantennas," *Cit. J. Appl. Phys.*, vol. 124, p. 163102, 2018.

[62] G. C. Righini *et al.*, "Whispering Gallery Mode microresonators: Fundamentals and applications," *Riv. del Nuovo Cim.*, vol. 34, no. 7, pp. 435–488, 2011.

[63] A. A. Vyshnevyy and D. Y. Fedyanin, "Lasing threshold of thresholdless and non-thresholdless metal-semiconductor nanolasers," *Opt. Express*, vol. 26, no. 25, p. 33473, 2018.

[64] Y. C. Hsu *et al.*, "Room temperature ultraviolet GaN metal-coated nanorod laser," *Appl. Phys. Lett.*, vol. 103, no. 19, pp. 1–5, 2013.

[65] R. M. Lammert *et al.*, "InGaAsP-InP ridge-waveguide DBR lasers with first-order surface gratings fabricated using CAIBE," *IEEE Photonics Technol. Lett.*, vol. 9, no. 11, pp. 1445–1447, 1997.

[66] A. I. Nosich, E. I. Smotrova, S. V. Boriskina, T. M. Benson, and P. Sewell, "Trends in microdisk laser research and linear optical modelling," *Opt. Quantum Electron.*, vol. 39, no. 15, pp. 1253–1272, 2007.

[67] S. L. McCall, A. F. J. Levi, R. E. Slusher, S. J. Pearton, and R. A. Logan, "Whispering-gallery mode microdisk lasers," *Appl. Phys. Lett.*, vol. 60, no. 3, pp.

289–291, 1992.

[68] Q. Song, H. Cao, S. T. Ho, and G. S. Solomon, "Near-IR subwavelength microdisk lasers," *Appl. Phys. Lett.*, vol. 94, no. 6, 2009.

[69] O. Salehzadeh, M. Djavid, N. H. Tran, I. Shih, and Z. Mi, "Optically Pumped Two-Dimensional MoS<inf>2</inf> Lasers Operating at Room-Temperature," *Nano Lett.*, vol. 15, no. 8, pp. 5302–5306, 2015.

[70] Y. Xu *et al.*, "Optical analysis of AlGaInP laser diodes with real refractive index guided self-aligned structure," in *Materials, Active Devices, and Optical Amplifiers*, 2004, vol. 5280, p. 29.

[71] B. Romeira and A. Fiore, "Purcell Effect in the Stimulated and Spontaneous Emission Rates of Nanoscale Semiconductor Lasers," *IEEE J. Quantum Electron.*, vol. 54, no. 2, 2018.

[72] K. Srinivasan, M. Borselli, O. Painter, A. Stintz, and S. Krishna, "Cavity Q, mode volume, and lasing threshold in small diameter AlGaAs microdisks with embedded quantum dots," *Opt. Express*, vol. 14, no. 3, p. 1094, 2006.

[73] T. Baba and D. Sano, "Low-Threshold Lasing and Purcell Effect in Microdisk Lasers at Room Temperature," *IEEE J. Sel. Top. Quantum Electron.*, vol. 9, no. 5, pp. 1340–1346, 2003.

[74] M. R. Foreman, J. D. Swaim, and F. Vollmer, "Whispering gallery mode sensors," *Adv. Opt. Photonics*, vol. 7, no. 2, p. 168, 2015.

[75] V. D. Ta, Y. Wang, and H. Sun, "Microlasers Enabled by Soft-Matter Technology," *Adv. Opt. Mater.*, vol. 1900057, pp. 1–30, 2019.

[76] J. Su, "Label-Free biological and chemical sensing using whispering gallery mode optical resonators: Past, present, and future," *Sensors (Switzerland)*, vol. 17, no. 3, pp. 1–18, 2017.

[77] A. Boleininger, T. Lake, S. Hami, and C. Vallance, "Whispering gallery modes in standard optical fibres for fibre profiling measurements and sensing of unlabelled chemical species," *Sensors*, 2010.

[78] H. Detz, "Thermal expansion of III-V materials in atomistic models using empirical Tersoff potentials," *Electron. Lett.*, vol. 51, no. 18, pp. 1455–1457, 2015.

[79] Y. Q. Kang, A. François, N. Riesen, and T. M. Monro, "Mode-splitting for refractive index sensing in fluorescent whispering gallery mode microspheres with broken symmetry," *Sensors (Switzerland)*, vol. 18, no. 9, pp. 1–9, 2018.

[80] A. L. Efros, J. B. Delehanty, A. L. Huston, I. L. Medintz, M. Barbic, and T. D. Harris, "Evaluating the potential of using quantum dots for monitoring electrical signals in neurons," *Nat. Nanotechnol.*, vol. 13, no. 4, pp. 278–288, 2018.

[81] P. B. Kruskal, Z. Jiang, T. Gao, and C. M. Lieber, "Beyond the patch clamp: Nanotechnologies for intracellular recording," *Neuron*. 2015.

[82] M. Dipalo *et al.*, "Intracellular and Extracellular Recording of Spontaneous Action Potentials in Mammalian Neurons and Cardiac Cells with 3D Plasmonic

Nanoelectrodes," *Nano Lett.*, 2017.

[83] G. Tsekenis, V. Vanikioti, K. Kordatos, and I. Zergioti, "Apta- and Immuno-Sensors Performance Optimization: A Comparative Study of Surface Functionalization Techniques," *Proceedings*, vol. 2, no. 13, p. 847, 2018.

[84] J. H. Choi *et al.*, "Selective Pump Focusing on Individual Laser Modes in Microcavities," *ACS Photonics*, vol. 5, no. 7, pp. 2791–2798, 2018.

[85] V. Kalashnikov, D. Krimer, I. Poloyko, and V. Mikhailov, "Ultrashort pulse generation in cw solid-state lasers with semiconductor saturable absorber in the presence of the absorption linewidth enhancement," 1999.

[86] P. Agrawal and C. M. Bowden, "Concept of Linewidth Enhancement Factor in Semiconductor Lasers: Its Usefulness and Limitations," 1993.

[87] B. R. Bennett, R. A. Soref, and J. A. Del Alamo, "Carrier-Induced Change in Refractive Index of InP, GaAs, and InGaAsP," *IEEE J. Quantum Electron.*, vol. 26, no. 1, pp. 113–122, 1990.

[88] Y. Xu *et al.*, "Optical analysis of AlGaInP laser diodes with real refractive index guided self-aligned structure," *Mater. Act. Devices, Opt. Amplifiers*, vol. 5280, no. May 2004, p. 29, 2004.

[89] S. Chen *et al.*, "Spectral dynamics of picosecond gain-switched pulses from nitride-based vertical-cavity surface-emitting lasers," *Sci. Rep.*, vol. 4, pp. 27–29, 2014.

[90] A. Mischok, "Controlling Light in Organic Microcavities," 2015.

[91] M. P. van Exter, G. Nienhuis, and J. P. Woerdman, "Two simple expressions for the spontaneous emission factor β," *Phys. Rev. A - At. Mol. Opt. Phys.*, vol. 54, no. 4, pp. 3553–3558, 1996.

[92] X. Liu *et al.*, "Continuous wave operation of GaAsBi microdisk lasers at room temperature with large wavelengths ranging from 127 to 141 μm," *Photonics Res.*, vol. 7, no. 5, p. 508, 2019.

[93] A. N. Kamalieva, N. A. Toropov, and T. A. Vartanyan, "Spasers monolayer based on silver nanoparticles," vol. 1067224, no. May 2018, p. 76, 2018.

[94] H. Zhu *et al.*, "Lead halide perovskite nanowire lasers with low lasing thresholds and high quality factors.," *Nat. Mater.*, vol. 14, no. 6, 2015.

[95] K. Wang, S. Wang, S. Xiao, and Q. Song, "Recent Advances in Perovskite Micro- and Nanolasers," *Advanced Optical Materials*, vol. 6, no. 18. Wiley-VCH Verlag, 18-Sep-2018.

[96] A. S. Berestennikov, P. M. Voroshilov, S. V. Makarov, and Y. S. Kivshar, "Active meta-optics and nanophotonics with halide perovskites," *Appl. Phys. Rev.*, vol. 6, no. 3, p. 031307, Sep. 2019.

[97] M. S. Song, H. Baek, and G.-C. Yi, "Intracellular GaN microrod laser," p. STu4H.7, 2019.

[98] B. Damilano *et al.*, "Top-down fabrication of GaN nano-laser arrays by displacement Talbot lithography and selective area sublimation," *Appl. Phys.*

Express, 2019.

[99] Q. Gu and Y. Fainman, "Semiconductor nanolasers," *Semicond. Nanolasers*, vol. 788, no. 4, pp. 1–332, 2017.

[100] C. A.R, "Guide to references on {III-V} semiconductor chemical etching," *Mater. Sci. Eng. R Reports*, vol. 31, no. 1–6, pp. 1–438, 2001.

[101] K. Petter, T. Kipp, C. H. Heyn, D. Heitmann, and C. Schüller, "Fabrication of large periodic arrays of AlGaAs microdisks by laser-interference lithography and selective etching," *Appl. Phys. Lett.*, vol. 81, no. 4, pp. 592–594, 2002.

[102] S. Yang, Y. Wang, and H. D. Sun, "Advances and Prospects for Whispering Gallery Mode Microcavities," *Adv. Opt. Mater.*, vol. 3, no. 9, 2015.

[103] "Modern GaAs processing methods," *III-Vs Rev.*, 1991.

[104] B. Cakmak, "Fabrication and characterization of dry and wet etched InGaAs/InGaAsP/InP long wavelength semiconductor lasers.," *Opt. Express*, vol. 10, no. 13, pp. 530–5, 2002.

[105] X. Li *et al.*, "Fabrication of ridge waveguide of 808 nm GaAs-based laser diodes by wet chemical etching," *J. Semicond.*, vol. 36, no. 7, p. 074009, 2015.

[106] I. Aharonovich *et al.*, "Low threshold, room-temperature microdisk lasers in the blue spectral range," *Appl. Phys. Lett.*, vol. 103, no. 2, 2013.

[107] V. Passi, A. Lecestre, C. Krzeminski, G. Larrieu, E. Dubois, and J. P. Raskin, "A single layer hydrogen silsesquioxane (HSQ) based lift-off process for germanium and platinum," *Microelectron. Eng.*, vol. 87, no. 10, pp. 1872–1878, 2010.

[108] A. Rastelli *et al.*, "Fabrication and characterization of microdisk resonators with In(Ga)As/GaAs quantum dots," *Phys. Status Solidi Curr. Top. Solid State Phys.*, vol. 3, no. 11, pp. 3641–3645, 2006.

[109] R. Debnath *et al.*, "Top-down fabrication of large-area GaN micro- and nanopillars," *J. Vac. Sci. Technol. B, Nanotechnol. Microelectron. Mater. Process. Meas. Phenom.*, vol. 32, no. 2, p. 021204, 2014.

[110] J.-H. Kim, "Selective etching of AlGaAs/GaAs structures using the solutions of citric acid/H[sub 2]O[sub 2] and de-ionized H[sub 2]O/buffered oxide etch," *J. Vac. Sci. Technol. B Microelectron. Nanom. Struct.*, vol. 16, no. 2, p. 558, 1998.

[111] S. Etching, Hb. Solutions, and S. E. Microscope, "Study of Silicon Etching in HBr Solutions using," *J. Chem. Soc.*, 1995.

[112] Z. Tomashik, S. Danylenko, V. Tomashik, and M. Kravetski, "Chemical dissolution of indium arsenide in the Br_2-HBr solutions," pp. 73–75, 1999.

[113] K. Shinoda, A. Taike, H. Sato, and H. Uchiyama, "Optimizing HBr-Br2-H2O etchants to form low defect regrowth interfaces for highly reliable InGaAsP/InP buried-heterostructure lasers," *J. Electrochem. Soc.*, vol. 150, no. 2, pp. 117–121, 2003.

[114] D. H. van Dorp *et al.*, "Nanoscale etching of III-V semiconductors in acidic hydrogen peroxide solution: GaAs and InP, a striking contrast in surface

chemistry," *Appl. Surf. Sci.*, vol. 465, pp. 596–606, 2019.

[115] M. M. A. J. Voncken *et al.*, "Etching AlAs with HF for Epitaxial Lift-Off Applications," *J. Electrochem. Soc.*, vol. 151, no. 5, p. G347, 2004.

[116] S. J. Pearton and F. Ren, "Wet chemical etching of compound semiconductors," *Proc. Electrochem. Soc.*, pp. 147–159, 2005.

[117] B. Gayral *et al.*, "High-Q wet-etched GaAs microdisks containing InAs quantum boxes," *Appl. Phys. Lett.*, vol. 75, no. 13, pp. 1908–1910, 1999.

[118] S. Adachi, Y. Noguchi, and H. Kawaguchi, "Chemical Etching of InGaAsP/InP DH Wafer," *J. Electrochem. Soc.*, vol. 129, no. 5, pp. 1053–1062, 1982.

[119] J. J. Kelly and H. G. G. Philipsen, "Anisotropy in the wet-etching of semiconductors," *Curr. Opin. Solid State Mater. Sci.*, 2005.

[120] P. H. L. Notten and A. A. J. M. Damen, "The electrochemistry of InP in Br2/HBr solutions and its relevance to etching behaviour," *Appl. Surf. Sci.*, vol. 28, no. 4, pp. 331–344, 1987.

[121] C. Strelow *et al.*, "Hybrid systems of AlInP microdisks and colloidal CdSe nanocrystals showing whispering-gallery modes at room temperature," *Appl. Phys. Lett.*, vol. 105, no. 9, p. 091107, Sep. 2014.

[122] T. Kallstenius, U. Smith, and B. Stoltz, "Studies of Internal Structure in InGaAsP/InP-Based Lasers Using Atomic Force Microscopy in Combination with Selective Etching," *J. Electrochem. Soc.*, 1999.

[123] J. R. Flemish, "Selective Wet Etching of GaInP, GaAs, and InP in Solutions of HCl, CH[sub 3]COOH, and H[sub 2]O[sub 2]," *J. Electrochem. Soc.*, vol. 140, no. 3, p. 844, 1993.

[124] P. Tomkiewicz, A. Winkler, M. Krzywiecki, T. Chasse, and J. Szuber, "Analysis of mechanism of carbon removal from GaAs(1 0 0) surface by atomic hydrogen," *Appl. Surf. Sci.*, vol. 254, no. 24, pp. 8035–8040, 2008.

[125] N. J. Kadhim, S. H. Laurie, and D. Mukherjee, "Chemical etching of group III-V semiconductors," *J. Chem. Educ.*, vol. 75, no. 7, pp. 840–843, 1998.

[126] M. Bauhuber, A. Mikrievskij, and A. Lechner, "Isotropic wet chemical etching of deep channels with optical surface quality in silicon with HNA based etching solutions," *Mater. Sci. Semicond. Process.*, 2013.

[127] A. T. J. Van Niftrik *et al.*, "HF species and dissolved oxygen on the epitaxial lift-off process of GaAs Using AlAsP release layers," *J. Electrochem. Soc.*, vol. 155, no. 1, pp. 1–6, 2008.

[128] M. Estruga, F. Meng, L. Li, L. Chen, X. Li, and S. Jin, "Large-scale solution synthesis of α-AlF<inf>3</inf> · 3H <inf>2</inf>O nanorods under low supersaturation conditions and their conversion to porous β-AlF<inf>3 nanorods," *J. Mater. Chem.*, vol. 22, no. 39, pp. 20991–20997, 2012.

[129] R. Elnathan *et al.*, "Maximizing transfection efficiency of vertically aligned silicon nanowire arrays," *Adv. Funct. Mater.*, 2015.

[130] J. Price, J. Barnett, S. Raghavan, M. Keswani, and R. Govindarajan, "A study

of the interaction of gallium arsenide with wet chemical formulations using thermodynamic calculations and spectroscopic ellipsometry," *Microelectron. Eng.*, vol. 87, no. 9, pp. 1661–1664, 2010.

[131] M. G. Scullion, A. Di Falco, and T. F. Krauss, "Slotted photonic crystal cavities with integrated microfluidics for biosensing applications," *Biosens. Bioelectron.*, vol. 27, no. 1, pp. 101–105, Sep. 2011.

[132] F. L. Lie, W. Rachmady, and A. J. Muscat, "In0.53Ga0.47As(1 0 0) native oxide removal by liquid and gas phase HF/H2O chemistries," *Microelectron. Eng.*, vol. 87, no. 9, pp. 1656–1660, 2010.

[133] N. V. Kryzhanovskaya *et al.*, "Room Temperature Lasing in 1-μm Microdisk Quantum Dot Lasers," *IEEE J. Sel. Top. Quantum Electron.*, vol. 21, no. 6, pp. 709–713, 2015.

[134] M. Humar, "Liquid-crystal-droplet optical microcavities," *Liq. Cryst.*, vol. 43, no. 13–15, pp. 1937–1950, 2016.

[135] H. Hamada, "Characterization of gallium indium phosphide and progress of aluminum gallium indium phosphide system quantum-well laser diode," *Materials (Basel).*, vol. 10, no. 8, pp. 1–18, 2017.

[136] P. Kumar, S. Kanakaraju, and D. L. Devoe, "Sacrificial etching of AlxGa1-xAs for III-V MEMS surface micromachining," *Appl. Phys. A Mater. Sci. Process.*, vol. 88, no. 4, pp. 711–714, 2007.

[137] K. S. Hsu *et al.*, "Compact microdisk cavity laser with type-II GaSb/GaAs quantum dots," *Appl. Phys. Lett.*, vol. 98, no. 5, 2011.

[138] C. Chen *et al.*, "Effects of edge inclination angles on whispering-gallery modes in printable wedge microdisk lasers," *Opt. Express*, vol. 26, no. 1, p. 233, 2018.

[139] G. S. Solomon *et al.*, "Optically pumped InAs quantum dot microdisk lasers," *Appl. Phys. Lett.*, vol. 76, no. 24, p. 3519, 2000.

[140] X. F. Jiang *et al.*, "Highly unidirectional emission and ultralow-threshold lasing from on-chip ultrahigh-Q microcavities," *Adv. Mater.*, vol. 24, no. 35, pp. 260–264, 2012.

[141] C. Weisbuch and J. Nagle, "The physics of the quantum well laser," *Phys. Scr.*, vol. 1987, no. T19A, pp. 209–214, 1987.

[142] M. Fujita, R. Ushigome, and T. Baba, "Large spontaneous emission factor of 0.1 in a microdisk injection laser," *IEEE Photonics Technol. Lett.*, 2001.

[143] P. S. Kuo, J. Bravo-Abad, and G. S. Solomon, "Second-harmonic generation using 4-quasi-phasematching in a GaAs whispering-gallery-mode microcavity.," *Nat. Commun.*, vol. 5, p. 3109, 2014.

[144] E. D. Haberer *et al.*, "Free-standing, optically pumped, GaN/InGaN microdisk lasers fabricated by photoelectrochemical etching," *Appl. Phys. Lett.*, vol. 85, no. 22, pp. 5179–5181, 2004.

[145] R. E. Slusher, A. F. J. Levi, U. Mohideen, S. L. McCall, S. J. Pearton, and R. A. Logan, "Threshold characteristics of semiconductor microdisk lasers," *Appl.*

Phys. Lett., vol. 63, no. 10, pp. 1310–1312, 1993.

[146] M. R. Foreman and F. Vollmer, "Theory of resonance shifts of whispering gallery modes by arbitrary plasmonic nanoparticles," *New J. Phys.*, vol. 15, 2013.

[147] N. Martino *et al.*, "Wavelength-encoded laser particles for massively multiplexed cell tagging," *Nat. Photonics*, 2019.

[148] Y. Choi, H. Jeon, and S. Kim, "A fully biocompatible single-mode distributed feedback laser," *Lab Chip*, vol. 15, no. 3, pp. 642–645, 2015.

[149] Y. Chen and X. Fan, "Biological Lasers for Biomedical Applications," *Adv. Opt. Mater.*, vol. 1900377, p. 1900377, 2019.

[150] X. Lopez-Yglesias, J. M. Gamba, and R. C. Flagan, "The physics of extreme sensitivity in whispering gallery mode optical biosensors," *J. Appl. Phys.*, vol. 111, no. 8, 2012.

[151] and F. V. Matthew R. Foreman, Jon D. Swaim, "Whispering gallery mode sensors Matthew," *Adv. Opt. Photonics*, vol. 6, pp. 293–339, 2014.

[152] R. N. Ratnaike, "Acute and chronic arsenic toxicity," *Postgraduate Medical Journal*. 2003.

[153] U. Bog *et al.*, "Large-Scale Parallel Surface Functionalization of Goblet-type Whispering Gallery Mode Microcavity Arrays for Biosensing Applications," *Small*, 2014.

[154] M. margaret Seale-goldsmith and J. F. Leary, "Nanobiosystems," *Wiley Interdisciplinary Reviews: Nanomedicine and Nanobiotechnology*. 2009.

[155] V. A. Sinani *et al.*, "Collagen coating promotes biocompatibility of semiconductor nanoparticles in stratified LBL films," *Nano Lett.*, 2003.

[156] J. Icha, M. Weber, J. C. Waters, and C. Norden, "Phototoxicity in live fluorescence microscopy, and how to avoid it," *BioEssays*. 2017.

[157] V. Magidson and A. Khodjakov, "Circumventing photodamage in live-cell microscopy," in *Methods in Cell Biology*, 2013.

[158] E. Blasco, M. B. Sims, A. S. Goldmann, B. S. Sumerlin, and C. Barner-Kowollik, "50th Anniversary Perspective: Polymer Functionalization," *Macromolecules*. 2017.

[159] J. Conde, J. T. Dias, V. Grazú, M. Moros, P. V. Baptista, and J. M. de la Fuente, "Revisiting 30 years of biofunctionalization and surface chemistry of inorganic nanoparticles for nanomedicine," *Frontiers in Chemistry*. 2014.

[160] A. Schroedter, H. Weller, R. Eritja, W. E. Ford, and J. M. Wessels, "Biofunctionalization of Silica-Coated CdTe and Gold Nanocrystals," *Nano Lett.*, 2002.

[161] J. Liu, J. Wen, Z. Zhang, H. Liu, and Y. Sun, "Voyage inside the cell : Microsystems and nanoengineering for intracellular measurement and manipulation," *Microsystems Nanoeng.*, vol. 1, no. August, pp. 1–15, 2015.

[162] S. Kobayashi *et al.*, "Artificial induction of autophagy around polystyrene beads

in nonphagocytic cells," *Autophagy*, vol. 6, no. 1, pp. 36–45, 2010.

[163] S. P. Poulos, M. V. Dodson, and G. J. Hausman, "Cell line models for differentiation: Preadipocytes and adipocytes," *Experimental Biology and Medicine*. 2010.

[164] R. Noy and J. W. Pollard, "Tumor-Associated Macrophages: From Mechanisms to Therapy," *Immunity*, vol. 41, no. 1. 2014.

[165] J. Condeelis and J. W. Pollard, "Macrophages: Obligate partners for tumor cell migration, invasion, and metastasis," *Cell*, vol. 124, no. 2. pp. 263–266, 2006.

[166] M. Schubert *et al.*, "Microlaser-based contractility sensing in single cardiomyocytes and whole hearts," 2019.

[167] A. N. Miliotou and L. C. Papadopoulou, "CAR T-cell Therapy: A New Era in Cancer Immunotherapy," *Curr. Pharm. Biotechnol.*, 2018.

[168] J. T. Robinson, M. Jorgolli, A. K. Shalek, M.-H. Yoon, R. S. Gertner, and H. Park, "Vertical nanowire electrode arrays as a scalable platform for intracellular interfacing to neuronal circuits," *Nat. Nanotechnol.*, vol. 7, no. 3, pp. 180–184, Jan. 2012.

[169] M. J. Stoddart, "Cell Viability Assays: Introduction," in *Mammalian Cell Viability: Methods and Protocols*, M. J. Stoddart, Ed. Totowa, NJ: Humana Press, 2011, pp. 1–6.

[170] A. C. Rowat *et al.*, "Nuclear envelope composition determines the ability of neutrophil-type cells to passage through micron-scale constrictions," *J. Biol. Chem.*, 2013.

[171] C. M. Denais *et al.*, "Nuclear envelope rupture and repair during cancer cell migration," *Science (80-.).*, 2016.

[172] K. Baumann, "Cell migration: Nuclear envelope ruptures as cells squeeze through tight spaces," *Nature Reviews Cancer*. 2016.

[173] N. Kramer *et al.*, "In vitro cell migration and invasion assays," *Mutation Research - Reviews in Mutation Research*. 2013.

[174] N. M. Kronenberg *et al.*, "Long-term imaging of cellular forces with high precision by elastic resonator interference stress microscopy," *Nat. Cell Biol.*, 2017.

[175] C. Chiappini *et al.*, "Mapping Local Cytosolic Enzymatic Activity in Human Esophageal Mucosa with Porous Silicon Nanoneedles," *Adv. Mater.*, 2015.

[176] Y.-C. Chen *et al.*, "Laser Recording of Subcellular Neuron Activities," *bioRxiv*, no. March, p. 584938, 2019.

[177] Y. Wang, A. Capretti, and L. Dal Negro, "Wide tuning of the optical and structural properties of alternative plasmonic materials," *Opt. Mater. Express*, 2015.

[178] C. Argyropoulos, P. Y. Chen, G. D'Aguanno, N. Engheta, and A. Alù, "Boosting optical nonlinearities in ε-near-zero plasmonic channels," *Phys. Rev. B - Condens. Matter Mater. Phys.*, 2012.

[179] X. Li, C. Rizza, S. A. Schulz, A. Ciattoni, and A. Di Falco, "Conformable optical coatings with epsilon near zero response," *APL Photonics*, 2019.

[180] X. Li, "Epsilon-Near-Zero Metamaterials for Optoelectronic Applications at the," 2019.

[181] J. Kim *et al.*, "Role of epsilon-near-zero substrates in the optical response of plasmonic antennas," *Optica*, 2016.

[182] R. Maas, J. Parsons, N. Engheta, and A. Polman, "Experimental realization of an epsilon-near-zero metamaterial at visible wavelengths," *Nat. Photonics*, 2013.

[183] H. C. Clark, "Chemistry of the Trifluoromethyl Group," *Can. J. Chem.*, vol. 40, no. 3, pp. 1–6, 1962.